

THEORETICAL STUDIES AND RATIONAL DESIGN OF
SYMMETRICAL AND UNSYMMETRICAL SQUARINE
DYES: AN APPLICATION FOR DYE-SENSITIZED SOLAR
CELL

AMEERUL HAZEEQ HASHIM

FACULTY OF SCIENCE
UNIVERSITI MALAYA
KUALA LUMPUR

2020

**THEORETICAL STUDIES AND RATIONAL DESIGN
OF SYMMETRICAL AND UNSYMMETRICAL
SQUARINE DYES: AN APPLICATION FOR DYE-
SENSITIZED SOLAR CELL**

AMEERUL HAZEEQ HASHIM

**DESSERTATION SUBMITTED IN FULFILMENT OF
THE REQUIREMENTS FOR THE DEGREE OF MASTER
OF SCIENCE**

**DEPARTMENT OF CHEMISTRY
FACULTY OF SCIENCE
UNIVERSITI MALAYA
KUALA LUMPUR**

2020

UNIVERSITI MALAYA
ORIGINAL LITERARY WORK DECLARATION

Name of Candidate: **AMEERUL HAZEEQ BIN HASHIM**

Registration/Matric No: **SGR150045**

Name of Degree: **MASTER OF SCIENCE**

Title of Dissertation: **THEORETICAL STUDIES AND RATIONAL DESIGN
OF SYMMETRICAL AND UNSYMMETRICAL SQUARINE DYE:
AN APPLICATION FOR DYE-SENSITIZED SOLAR CELL**

Field of Study:

COMPUTATIONAL CHEMISTRY

I do solemnly and sincerely declare that:

- (1) I am the sole author/writer of this Work;
- (2) This Work is original;
- (3) Any use of any work in which copyright exists was done by way of fair dealing and for permitted purposes and any excerpt or extract from, or reference to or reproduction of any copyright work has been disclosed expressly and sufficiently and the title of the Work and its authorship have been acknowledged in this Work;
- (4) I do not have any actual knowledge nor do I ought reasonably to know that the making of this work constitutes an infringement of any copyright work;
- (5) I hereby assign all and every rights in the copyright to this Work to the University of Malaya ("UM"), who henceforth shall be owner of the copyright in this Work and that any reproduction or use in any form or by any means whatsoever is prohibited without the written consent of UM having been first had and obtained;
- (6) I am fully aware that if in the course of making this work I have infringed any copyright whether intentionally or otherwise, I may be subject to legal action or any other action as may be determined by UM.

Candidate's Signature

Date:

Subscribed and solemnly declared before,

Witness's Signature

Date:

Name:

Designation:

**THEORETICAL STUDIES AND RATIONAL DESIGN OF SYMMETRICAL
AND UNSYMMETRICAL SQUARINE DYES: AN APPLICATION FOR DYE-
SENSITIZED SOLAR CELL**

ABSTRACT

Dye- sensitized solar cell (DSSC) has been explored in depth due to its effectiveness and low-cost conversion of photovoltaic energy. Squaraine has unique properties because it has the capacity to increase light-harvesting energy as well as its low-cost conversion of photo-energy. Dyes that perform well, namely the symmetrical indolenine-based squaraine dye (SQM1a, VG1, and VG10) and the unsymmetrical indolenine-based squaraine dye (SQM1b, SQ01, MSQ, and VG13) were computationally studied and modified. Six density functionals were used to verify the accuracy of the simulation ranging from generalized gradient approximation (pure-GGA) density functional to the large Hartree-Fock exchange functional. Three methods were used to benchmark oxidation potential for all seven dyes namely, the vertical ground state oxidation potential (GSOP_v), adiabatic ground state oxidation potential (GSOP_a) and Koopman's Theorem. Calculation for oxidation potential via GSOP_v using M062X has provided better correlation to experimental oxidation potential energy level with mean absolute error of 0.0081 eV. Following the success in benchmarking experimental oxidation potential energy level, GSOP_v was employed using M062X hybrid meta-GGA functional as part of the advanced theoretical methods to modify squaraine dye structure via Dewar's rule. SQM1a was modified by addition of either electron donating (ED) or electron-withdrawing (EW) substituent along the π -conjugated bridge. Methoxy (-OCH₃) and nitrile (-CN) were chosen as the ED unit and EW unit respectively. As a consequence, the highest occupied molecular orbital (HOMO) and the lowest unoccupied molecular orbital (LUMO) energy levels were altered for band gap optimization.

Keywords: Vertical ground state oxidation potential (GSOP_v), adiabatic ground state oxidation potential (GSOP_a), Dye- Sensitized solar cell (DSSC).

University of Malaya

**KAJIAN TEORI DAN REKA BENTUK RASIONAL BAGI PEWARNA
SQUARIN SIMETRI DAN TIDAK SIMETRI: APLIKASI BAGI PEMEKAAAN
PEWARNA SEL SURIA**

ABSTRAK

Sel suria terpeka pewarna (DSSC) telah diterokai dengan mendalam kerana keberkesanan dan penjimatan kos untuk penuaian cahaya melalui tenaga fotovolttek. Squarin mempunyai ciri-ciri unik kerana dapat meningkatkan serta menjimatkan kos penukaran tenaga penuaian cahaya. Pemekaan pewarna squarin berasaskan indolenin simetri (SQM1a, VG1, VG10) dan pemekaan pewarna squarin berasaskan indolenin tidak simetri (SQM1b, SQ01, MSQ, VG13) akan dikira dan diubahsuai secara teori. Enam fungsi ketumpatan telah digunakan untuk mengesahkan ketepatan simulasi bermula daripada fungsi ketumpatan kecerunan umum (GGA-tulen) kepada fungsi ketumpatan yang mempunyai pertukaran fungsi Hartree-Fock yang besar. Tiga kaedah digunakan untuk menentukan potensi pengoksidaan bagi tujuh pemekaan pewarna iaitu potensi pengoksidaan keadaan tegak ($GSOP_v$), potensi pengoksidaan keadaan adiabatik ($GSOP_a$) dan Teorem Koopman. Pengiraan untuk potensi pengoksidaan menggunakan $GSOP_v$ melalui M062X telah memberikan nilai yang dekat dengan tahap potensi tenaga pengoksidaan eksperimen dengan min purata ralat mutlak 0.0081 eV. Berikutan kejayaan dalam penandaarasan tahap tenaga potensi pengoksidaan eksperimen, $GSOP_v$ digunakan bersama fungsi hibrid meta-GGA M062X sebagai salah satu kaedah teori untuk mengubah suai struktur pewarna squarin berdasarkan peraturan Dewar. SQM1a telah diubahsuai dengan penambahan penyumbang elektron (ED) atau pengurangan elektron (EW) di sepanjang jambatan π -konjugat. Metoksi (-OCH₃) dan nitril (-CN) dipilih sebagai unit ED dan unit EW. Oleh yang demikian, tahap tenaga orbital molekul terisi yang tertinggi (HOMO) dan tahap tenaga orbital molekul tidak terisi yang terendah (LUMO) telah diubah untuk pengoptimum jurang jalur.

Kata Kunci: Potensi Pengoksidaan Keadaan Tegak (GSOPv), Potensi Pengoksidaan Keadaan Adiabatik (GSOPa), Sel Suria Terpeka Pewarna (DSSC).

University of Malaya

ACKNOWLEDGEMENTS

I would like to thank Institut Pengurusan & Pemantauan Penyelidikan Universiti Malaya (IPPP) and Fundamental Research Grant Scheme (FRGS) for their financial supports. Not to forget, all Department of Chemistry staffs that have directly or indirectly contributed in this research project. A special word of thanks to the technicians and Data-intensive Computing Centre (DICC) staff, who went the extra kilometres in managing Universiti Malaya Cluster.

A big thanks to all the members from computational lab and inorganic lab over the last couple of years – I must definitely give them compliments for what they have done for me and for the wedding gift. In relation to the work contained in this thesis, The most special gratitude goes to my supervisors Professor Dr. Shariffudin Md Zain for giving me the confidence to do computational chemistry – and for your help with the experimental work. Thank you to Associate Professor Dr. Vannajan Sanghiran Lee for the motivation to finish this thesis. I thank them for their delightful guidance throughout the journey. I'd especially like to thank and Professor Dr. Hapipah Mohd Ali.

To my family, my father Hashim Hasan and mother Halimah Ibrahim. Without their continuous support, it is impossible for me to finish this work. To my beloved wife, Nurul Nadiah Zakaria for her everlasting support. Thanks for being positive, when I was negative. My siblings, Ameerul Hakeem and Ameerul Haneef, they have given me support and advice concernedly during the study period.

TABLE OF CONTENTS

ABSTRACT	iii
ABSTRAK	v
ACKNOWLEDGEMENTS	vii
TABLE OF CONTENTS	viii
LIST OF FIGURES	viii
LIST OF TABLES	xiii
LIST OF SYMBOLS AND ABBREVIATIONS	xiv
CHAPTER 1: INTRODUCTION	1
1.1 Background.....	1
CHAPTER 2: LITERATURE REVIEW	10
2.1 Computational Chemistry Development	10
2.2 Dye- Sensitized Solar Cell (DSSCs)	12
2.2.1 Device structure.....	13
2.2.2 Operating mechanism.....	14
2.2.3 Features of Dye Sensitizers	17
2.2.4 Photovoltaic Cell Parameters	19
2.3 Squarine Dye	26
2.4 Structure modification based on Dewar's Rule	32
2.5 Computational prediction for dye.....	34
2.6 Hartree-Fock Theory	36
2.7 Density Functional Theory	41
2.8 Research Aims and Objectives.....	43

CHAPTER 3: RESEARCH METHODOLOGY	44
3.1 Introduction	44
3.2 Ground State Calculation.....	45
3.3 Ground state oxidation potential.....	48
3.4 Excited State Calculation.....	51
3.5 Dewar's Rule	55
CHAPTER 4: RESULT AND DISCUSSION.....	60
4.1 Ground state determination	60
4.1.1 Conformation Study	60
4.2 Ground State Oxidation Potential (GSOP).....	62
4.2.1 GSOP Obtained from Energy Difference.....	62
4.3 Excited State Calculation.....	96
4.4 Ultraviolet-Visible Spectrophotometer (UV-Vis)	107
4.5 Structural Design by Dewar's Rule	112
4.6 Ground State Dye Evaluation Based on Dewar's Rule	117
4.7 Excited State Dye Evaluation	118
CHAPTER 5: CONCLUSION.....	125
REFERENCES.....	127
LIST OF PUBLICATIONS AND PAPERS PRESENTED	139

LIST OF FIGURES

Figure 1.1	: a) A scheme of D- π -A dye configuration. b) Some example of chemical groups employed for different moieties of the metal-free organic dye sensitizers.....	8
Figure 1.2	: The Cyanoacrylic Acid Acceptor/ Anchoring Group.....	9
Figure 2.1	: Mechanism of a DSSC system converting light to electricity.....	16
Figure 2.2	: Current, Voltage and Power Relationship in Photovoltaic Cell.....	20
Figure 2.3	: Photon Wavelengths and Radiant Photon Flux Density Relationship.....	23
Figure 2.4	: Absorption and emission spectra of N,N-dimethylaniline derivative squaraine dye immersed in CH ₃ Cl solution (reprinted from ref. 94 with permission. © (1997) American Chemical Society).....	27
Figure 2.5	: Symmetrical Squaraine Dyes.....	29
Figure 2.6	: Unsymmetrical Squaraine Dyes.....	31
Figure 2.7	: Potential Energy Surface Diagram.....	33
Figure 2.8	: Gaussian Algorithm for Self-Consistent Field (SCF)	39
Figure 3.1	: Representation of the Potential Energy Curves Used in Determining GSOP _v and GSOP _a	49
Figure 3.2	: Gap Energies in Molecular Ground State and Excited State.....	54
Figure 3.3	: Optimized 3D Structure of SQM1a Dye Sensitizer (Red: Oxygen; Blue: Nitrogen; Grey: Carbon). Hydrogen Atoms Are Not Displayed To Aid Visualization	56
Figure 3.4	: Schematic Diagram for SQM1a with Starred and Unstarred Labelled Position. Take Note That Starred Position is Put Asterisk and Unstarred Position is Left Empty, Alternating Starred Position.....	58
Figure 3.5	: Research Process Flow Chart.....	59

Figure 4.1	: GSOP _v versus the calculated GSOP _v using various density functionals in DCM employing the C-PCM framework.....	62
Figure 4.2	: GSOP _a versus the calculated GSOP _a using various density functionals in DCM employing the C-PCM framework.....	65
Figure 4.3	: HOMO _{exp} versus the calculated HOMO _{cal} based on Koopman's Theorem using various density functionals in DCM employing the C-PCM framework.....	67
Figure 4.4	: Absolute errors for the calculated Squarine Dyes via GSOP _v using different functionals based on the C-PCM framework... ..	70
Figure 4.5	: Absolute errors for the calculated Squarine Dyes via GSOP _a using different functionals based on the C-PCM framework.....	71
Figure 4.6	: Absolute errors for the calculated Squarine Dyes via HOMO _{cal} using different functionals based on the C-PCM framework.....	71
Figure 4.7	: Absolute errors of the calculated HOMO _{cal} , GSOP _v , and GSOP _a of SQM1 _a using different functionals in Chloroform based on the C-PCM framework.....	75
Figure 4.8	: Absolute errors of the calculated HOMO _{cal} , GSOP _v , and GSOP _a of SQM1 _b using different functionals in Chloroform based on the C-PCM framework.....	79
Figure 4.9	: Absolute errors for the calculated HOMO _{cal} , GSOP _v , and GSOP _a of MSQ using different functionals in Chloroform based on the C-PCM framework.....	82
Figure 4.10	: Absolute errors for the calculated HOMO _{cal} , GSOP _v , and GSOP _a of VG1 using different functionals in Chloroform based on the C-PCM framework.....	85
Figure 4.11	: Absolute errors for the calculated HOMO _{cal} , GSOP _v , and GSOP _a of SQ01 using different functionals in Chloroform based on the C-PCM framework.....	87

Figure 4.12	: Absolute errors for the calculated HOMO _{cal} , GSOP _v , and GSOP _a of VG10 using different functionals in Chloroform based on the C-PCM framework.....	91
Figure 4.13	: Absolute errors for the calculated HOMO _{cal} , GSOP _v , and GSOP _a of VG13 using different functionals in Chloroform based on the C-PCM framework.....	93
Figure 4.14	: SQM1a energies comparison of the HOMOs (ϵ_{HOMO}), the LUMOs (ϵ_{LUMO}), the HOMO–LUMO energy gap ($\Delta\epsilon_{\text{es}}$), in CHCl ₃ solution calculated with different density functional at excited state.....	97
Figure 4.15	: SQM1a energies comparison of the HOMOs (ϵ_{HOMO}), the LUMOs (ϵ_{LUMO}), the HOMO–LUMO energy gap ($\Delta\epsilon_{\text{es}}$), in CHCl ₃ solution calculated with different density functional at excited state	98
Figure 4.16	Bloch’s Theorem Representation Diagram Defining Lattice Constant, α	100
Figure 4.17	Band Structure Diagram	102
Figure 4.18	Experimental and Simulated UV-VIS Graph for SQM1a Using Different Density Functionals.....	108
Figure 4.19	Molecular Orbital Editor Displayed in Gaussview.....	111
Figure 4.20	HOMO–LUMO energy gap ($\Delta\epsilon_{\text{es}}$) Energies Comparison for SQM1a and New Dyes by TD-DFT.....	122
Figure 4.21	Experimental and Simulated UV-VIS Graph for SQM1a and New Dyes Respectively. Single Point Excitation Using TD-DFT at PBE0/6-31+G (d) in Chloroform.....	124

LIST OF TABLES

Table 2.1	: The Dependency of Harvested Light and Current Density Expressed in Terms of Wavelength.....	24
Table 4.1	: Bond Distances (Å) and Angles (°) for Compound SQM1a, Calculated at DFT Level Using Various Functional/ 6-31G(d).....	61
Table 4.2	: Calculated GSOP _v , GSOP _a , HOMO _{cal} for Compound SQM1a Using Various Density Functional.....	73
Table 4.3	: Calculated GSOP _v and GSOP _a for Compound SQM1b Using Various Density Functional.....	78
Table 4.4	: Calculated GSOP _v , GSOP _a and HOMO _{cal} for Compound MSQ Using Various Density Functional.....	81
Table 4.5	: Calculated GSOP _v and GSOP _a for Compound VG1 Using Various Density Functional.....	84
Table 4.6	: Calculated GSOP _v and GSOP _a for Compound SQ01 Using Various Density Functional.....	86
Table 4.7	: Calculated HOMO _{cal} , GSOP _v and GSOP _a for Compound VG10 Using Various Density Functional.....	89
Table 4.8	: Calculated GSOP _v and GSOP _a for Compound VG13 Using Various Density Functional.....	92
Table 4.9	: Band Gap From HOMO-LUMO, $\Delta\epsilon_{\text{fundamental}}$ and GSOP _v -LUMO, $\Delta\epsilon_{\text{ES}}$ Calculation.....	105
Table 4.10	: Calculated Excited State Energy (nm), Oscillator Strength and Transition Configuration of SQM1a by TD-DFT Employing Different Density Functional.....	109
Table 4.11	: Optimized Three-Dimensional Structure for SQM1a and New Dyes. Carbon is represented by grey Ball, Oxygen by red Ball and Nitrogen.....	112

Table 4.12	:	Selected π -Bridge Length (L_{π}), Bond Length, Bond Angle, Dihedral Angle and Dipole Moments for SQM1a and New Dyes.....	116
Table 4.13	:	Frontier Molecular Orbital for SQM1a and New Dyes Obtained via Single Point Calculation Employing PBE0/6-31+G(d) at Excited State.....	119
Table 4.14	:	Calculated Excited State Energy (nm), Oscillator Strength and Transition Configuration of SQM1a and New Dyes by TD-DFT via Single.....	123

University of Malaysia

LIST OF SYMBOLS AND ABBREVIATIONS

$M_{(g)}^-$: Anionic Molecule in Gas Phase
χ_{μ}	: Atomic Function
$E^+(M^+)$: Cationic Energy of the Cationic Molecule
\hat{J}	: Coulomb Energy
IV	: Current-Voltage
S^*	: Dye at Excited State
S	: Dye at Ground State
ρ_0	: Electron Density
L_n	: Electron Diffusion Length
E_g	: Electronic Band Gap
$e_{(g)}^-$: Electron in Gas Phase
E_{SD}	: Energy of Slater Determinant
\hat{K}	: Exchange Energy
V_{ext}	: External Potential Energy
\hat{F}	: Fock Operator
g_p	: Gaussian Function
$d_{\mu,p}$: Gaussian Primitive Function
L_p	: Hole Diffusion Length
I/I_3^-	: Iodide / Triiodide
e_{pt}^-	: Injected Electron from Platinum Counter Electrode
\hat{T}	: Kinetic Energy
HOMO _{cal}	: Koopman's Theorem Ionization Energy
ω B97XD	: Long Range Becke Corrected 1997 Dispersion Density Functional

$-\text{OCH}_3$: Methoxy Substituent
$E^+(\text{M})$: Neutral Molecule Cationic Energy
$E(\text{M})$: Neutral Molecule Ground State Energy
$\text{M}_{(\text{g})}$: Neutral Molecule in Gas Phase
$-\text{CN}$: Nitriles Substituent
\hat{V}_{NE}	: Nuclear-Electron Attraction Energy
V_{oc}	: Open Circuit Photovoltage
Φ_i	: Operator
ϵ_i	: Orbital Energies Eigenvalue
ζ	: Orbital Exponent
S^+	: Oxidized Dye at Conduction Band
Φ	: Photon Flux
n_{photon}	: Photon Number
P	: Power Density
S_1	: Singlet Excited State
S_0	: Singlet Ground State
I_{sc}	: Short Circuit Current
J_{sc}	: Short-Circuit Current Density
η	: Solar Conversion Efficiency
ω	: Spin Coordinate
U^0	: Standard Internal Energy
A	: Surface Area
t	: Time
GSOP_v	: Vertical Ground State Oxidation Potential

Ψ	: Wavefunction
λ	: Wavelength
AE	: Adiabatic Electron Affinity
GSOP _a	: Adiabatic Ground State Oxidation Potential
AI	: Adiabatic Ionization Potential
B3LYP	: Becke-3-Parameter Lee-Yang-Parr Density Functional
CdTe	: Cadmium Telluride
CH ₃ Cl	: Chloromethane
CASSCF	: Complete Active Space Self-Consistent Field
CB	: Conduction Band
CIS	: Configuration Interaction Singles
CIGS	: Copper Indium Gallium Selenide
C-PCM	: Conductor-like Polarizable Continuum Model
D- π -A	: Donor Group- π Bridge Linkage-Acceptor Group Configuration
DSSC	: Dye- Sensitized Solar Cell
DFT	: Density Functional Theory
ED	: Electron Donating Group
ESOP	: Excited State Oxidation Potential
EW	: Electron Withdrawing Group
ETM	: Electron Transporting Material
FF	: Fill Factor
FTO	: Fluorine-Doped Tin Oxide
GGA	: Generalized Gradient Approximation
GHG	: Greenhouse gas

GSOP	: Ground State Oxidation Potential
GSOP	: Ground State Oxidation Potential
HOMO	: Highest Occupied Molecular Orbital
HTM	: Hole Transporting Material
HF	: Hartree-Fock
ICT	: Intermolecular Charge Transfer
ITO	: Indium Tin Oxide
IR	: Infra-Red
KS	: Kohn-Sham
LUMO	: Lowest Unoccupied Molecular Orbital
MAEs	: Mean Absolute Error
MLCT	: Metal-Ligand Charge Transfer
MPW1k	: Meta-Hybrid Generalized Gradient Density Functional
M062x	: Minnesota 06 Global Hybrid Functional
MO	: Molecular Orbital
NIR	: Near Infra-Red
NBMO	: Non-Bonding Molecular Orbital
PBE0	: Perdew-Burke Ernzerhof Density Functional
PCM	: Polarizable Continuum Model
PEC	: Photoelectrochemical
PMO	: Perturbation Molecular Orbital
PW	: Plane-Wave
PW91	: Perdew-Wang 1991 Density Functional
PV	: Photovoltaic
PES	: Potential Energy Surface

SCF	: Self-Consistent Field
SD	: Slater determinant
SMO	: Semiconducting Metal Oxide
SQM	: Squarine
MSQ	: Squarylium Dye
SMD	: Solvation Model Based on Desntiy
SA-	: State Averaging Complete Active Space Self-
CASSCF	Consistent Field
SQM1a	: Symmetrical Dicyanovinylene Squarine Dye
SQM1b	: UnSymmetrical Dicyanovinylene Squarine Dye
SQ01	: Unsymmetrical Trimethyl-indolenine Squarine
SnO ₂	: Tin Dioxide
TCO	: Transparent Conducting Oxide
TiO ₂	: Titanium Dioxide
TD-DFT	: Time Dependent Density Functional Theory
TPB	: Tetraphenylbenzidine
TICT	: Twisted Intramolecular Charge Transfer State
UV-Vis	: Ultraviolet-Visible
VG1	: Symmetrical Trimethyl-indolenine Squarine
VG10	: Symmetrical Bis-Benzoinolenine Squarine
VG13	: Unsymmetrical Bis-Benzoinolenine Squarine
VASP	: Vienna Ab Initio Simulation Package
VB	: Valence Band
XC	: Exchange Energy Functional
ZPE	: Zero-Point Vibrational Energies

CHAPTER 1: INTRODUCTION

1.1 Background

Malaysia's total greenhouse gas (GHG) emissions represent about 0.6% of global emissions in 2011. Carbon fossil fuel combustion industry continue to dominate in the country ending GHG at 279,098.38 kt of CO₂ equivalent in 2012. Throughout the century, the heavily subsidized incumbent fossil fuel has dominated the energy industry, resulting in a serious of environmental impact. Fossil fuels combustion emits number of air pollutants such as nitrogen oxides (NO_x = NO₂ + NO), sulfur oxides (SO₃ + SO₂), fly ash containing trace elements (heavy metals), and volatile carcinogenic organic compounds (Chmielewski, 1999). The burning of fossil fuel does not only pollute the air but acts directly on water and soil. Dry and wet deposition of inorganic pollutants give rise to acidification of environment to land and aquatic life. Apart from natural environmental issues, fossil fuel energy also poses a threat in terms of macroeconomic environment. As of June 2014, oil prices fall from an annual average price of US\$99 in 2014 to US\$43 in 2016. The implication is seen worst in oil-intensive country such as Venezuela with inflation rise up to 481.52% through the year and 1,642% in 2017. The macroeconomic climate triggers world leaders to navigate the challenges onto a more sustainable and longer term of dynamic energy supply.

In line with increasing impetus towards a sustainable energy system, renewable energies have become a top agenda and priority for leaders around the globe. In 2015, China represented 36% of global investment in renewable energy, catalyzing the development of solar photovoltaic (PV) and wind power generation. Generation of electricity by wind is known as wind power energy while electrical production from solar radiation is known as solar PV. Wind energy has more disadvantages compared to its counterpart, solar PV. Disadvantages of wind energy include the fact that it relies entirely on the availability of wind, large acres of land and expensive cost of installation. The

efficiency and availability of wind passes on daily basis is highly specific on location. Coastal region will have more energy generated than other areas, suggesting that not all countries will have the maximize usage on wind energy system. On the contrary, solar PV does not depend on climate or location. Solar energy will still be generated on cloudy or rainy weather. The requirement to install a solar PV generator is much more flexible in terms of cost and space than wind energy.

The first idea of solar cell was discovered by Charles Fritts in 1884 (Guarnieri, 2015). Fritts' solar cell had a very poor efficiency, comprise a layer of selenium covered with gold film. Edmond Becquerel, a French physicist, continued the legacy and was the first person to demonstrated photovoltaic effect using electrochemical cell back in 1939 (A. E. Becquerel, 1839). An electric current was observed when 2 metal sheets (electrodes) were illuminated and dipped into an electrolyte solution. However, these observations were later explained in 1905 by Albert Einstein. Einstein introduced the concept of "light quanta", which means that light energy is carried by an indivisible packet known as photon (Einstein, 1905). This revolutionary discovery was the stepping stone for light technology.

Solar cell energy has now successfully competing with polluting fossil fuel plant as the primary source of energy supply. 227 GW of clean renewable solar power have been installed across the global market at the end of 2015, creating thousands of jobs and paving the way towards a cleaner energy future. PV cells or also known as solar cells, is an electric device which can be powered and generate electricity from the illumination of the sun. The first generation PV cell which is commercially available are based on wafers comprising crystalline silicon (Green, 2001). Monocrystalline silicon is expensive to grow but promised a high light to energy conversion. Mostly, first generation PV cells are installed in residential area to power house appliances. Second generation PV cell, known as the thin film PV cells arise as to counter the expensive cost of manufacturing process.

Thin film PV cells are cheaper to produce, provided that they comprise of inexpensive elements. Second generation PV cells are mostly made up of amorphous and polycrystalline silicon which require less material to manufacture. Thin film copper indium gallium selenide (CIGS) PV cells and modules have achieved 19.5% efficiencies while the cadmium telluride (CdTe) PV cells are 16.5% efficient (Noufi et al., 2006). However, first generation PV cell shows a higher efficiency than the second generation with 25% efficiency (Green et al., 2014). Also, their outspread production is constrained by the limited availability of tellurium, indium and selenium. One other disadvantage for second generation PV cells is the high toxicity of the metal used, cadmium. This pose a serious threat to any emerging technology because the key to a successful development is stability and sustainability (Cann et al., 2016). The focus of attention has again shifted in developing a more efficient, cost effective and environmentally friendly PV cells. At last, dye sensitized solar cells (DSSCs) comprise all value of emerging technology, representing as the third generation PV cells.

Dye-Sensitized Solar Cell (DSSC) is a well-known device for electrical supply and lighting application in households. By converting sunlight into electricity, this device is considered using a freely available and renewable resource. Along with this neat energy resource, DSSC has attracted so much attention from researchers due to its highly efficiency and low-cost fabrication. One major difference between DSSC and conventional PV cells is the working principle. For a conventional PV cells, both the charge separation and light absorption is done by the semiconducting material. On the contrary, DSSC separate these two principles. The semiconductor which act as the electrode is responsible for charge separation and electron transportation. A sensitizer or dye is responsible for light absorption hence, the name DSSC.

In 2010, thousands of articles have been published discussing on dye sensitized solar cells. Topics of discussion attribute to increase in efficiency and understanding the internal mechanism of a DSSCs, making it the hottest field of science research in this century (Peter, 2011). The downside to this rapid development is mainly due to the expensive and time consuming to design, synthesize, device fabrication, and testing of the new materials (Mishra et al., 2009).

Without any clear understanding and information on new dyes, synthetic chemist would find it hard to develop dye sensitizer with desirable properties (Zhang et al., 2012). Chemical intuition alone is insufficient to determine the structure and property relationship of a new dye sensitizer. Quantum mechanical calculation using high performance computer enables researcher to understand the internal mechanism and physical behavior of desired dye at electronic level. Hence, DSSC development is propelled by the utilization of computational chemistry.

Computational chemistry is a powerful branch of chemistry prior to synthesis which provide reliable tool to mimic the material properties, design, analyze and develop new materials. Such calculations come with a price of a supercomputing facilities. In reality, DSSC comprise sophisticated dimension system, interatomic interaction and electronic mechanism.

Thus, it is hurdle to simulate the entire working cell as a holistic theoretical approach. Different phases (interface, gas, and solution), ground state and excited state need to be taken into account when investigating DSSC working principle. Balance between theoretical methods and computing capabilities have also pose another problem. A very precise theoretical method requires long hour, expensive computational power and vice versa.

Nevertheless, in long terms, computational chemistry is a promising approach to provide many solution in everyday research problem, making it a demanding and promising field (Mariachiara & Filippo, 2012). It is proven that theoretical approach is efficient in understanding the internal mechanism and developing DSSC materials. Recent review on the first principle quantum chemical calculation reported successive approach to model and probe DSSCs theoretically (Pastore & De Angelis, 2014). A notable review on the state-of-art computational design for isolated DSSC system is done by Labat and group (Labat et al., 2012). Labat et al. have successfully reproduce and predict spectroscopic property of dye sensitizer using density functional theory (DFT).

Research done by the computational state-of-art can be categorized in two main areas. Firstly, the computational investigation of isolated DSSC component (e.g. redox couple system, dye sensitizer, and the nanocluster system). Second category is the simulation between two or more DSSC components. The current thesis will focus on the development of computer aided rational design and internal mechanism investigation of isolated DSSC component, the dye sensitizer.

Countless research has been performed for isolated DSSC component. DFT and time dependent DFT (TD-DFT) are employed to investigate dye sensitizer at ground and excited level, respectively. Molecular geometry, binding modes, aggregation, polarizability and frontier molecular orbital are obtained from DFT calculation while estimated lowest unoccupied molecular orbital (LUMO) and Ultraviolet-visible (UV-Vis) absorption spectra are obtained from TD-DFT (Pastore & De Angelis, 2014). Computer-aided rational design starts off with modeling and calculation of dye sensitizer property.

This is done to correlate between theoretical and experimental databases such as cyclic voltammetry and UV-Vis spectroscopy. Numerous computational approaches will be employed to probe experimental data. DFT and TD-DFT models comprise of different

density functional and basis sets, each combination is different and calculated based on the calculation agreement available from experimental databases. For each reference dye selected, results obtained from DFT and TD-DFT are compared with experiment parameters. Model that best describe experimental parameters will be used for further in-silico DSSC development, corresponding to the new computer-aided rational design dye.

Rational design of dye structure by systematic chemical modification is done based on the chosen computation method. New dyes are developed with better conversion efficiency, reducing synthesis time and cost. The discovery of new dye by the computer-aided rational design has spark several group for further development and motivated the current thesis (Fan et al., 2012; Feng et al., 2013; Zhou et al., 2012; Mohammadi & Wang, 2014; Sánchez et al., 2012; Yang et al., 2012; Zhang et al., 2012).

Computer-aided rational design is generally understood as achieving a desired property of an object by predicting their behavior by means of theoretical methodology (Parnas & Clements, 1985). Conjugated organic molecule adapt a D- π -A configuration, shown in Fig. 1.1, where each organic sensitizer is divided into 3 moieties. The donor group of the sensitizer is denoted as 'D'. The 'D' group responsible for the source of electron in the organic molecule.

The linker that connects both end of the group is known as the conjugated bridge, denoted as ' π '. The ' π ' group act as a pathway for electron to be distributed from 'D' group to 'A' group. The 'A' group is the acceptor moiety, the chemical group that is sensitized onto the nanocluster semiconductor. Upon excitation, electron is distributed from 'D' group, to the π -linker group before it is channeled to 'A' group. The electron is said to have travelled throughout one isolated DSSC component, the dye sensitizer before being diffused into the next DSSC component, the nanocluster semiconductor (Fischer et al.,

2010; Li et al., 2013; Mao & Song, 2016; Marszalek et al., 2013; Ooyama et al., 2014; Chang et al., 2010; Yang et al., 2014).

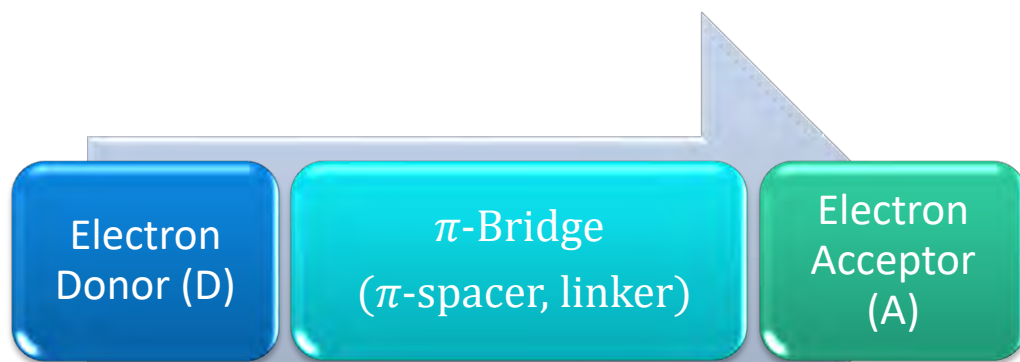
Computer-aided rational design of organic dye sensitizer based on D- π -A structure provide an effective approach towards desirable properties. Independent modification can be done onto individual dye sensitizer and moieties.

Chemical structure at π -bridge linkage is modified. Hence, tuning the highest occupied molecular orbital (HOMO) and the lowest unoccupied molecular orbital (LUMO) energy levels of an organic dye sensitizer (Hagberg et al., 2007). In this thesis, this strategy is employed on a coupled of well-performing dyes as part of the computer-aided rational design.

Throughout this thesis, the already well-performing dyes will be referred as “the reference” or “the parent” dyes. They are selected based on their symmetrical structure, flexibility in structural modification and their overall performance. Once a suitable computational methodology has been identified, the reference dyes are modified into desirable new dyes.

The main objective of this research is to develop a new dye with a smaller band gap thus, shifting the absorption spectra into the red region. There are several approaches that can be adopted to decrease the band gap of an organic dye sensitizer: (1) Modification on the π -bridge linkage structure, (2) introduction of electron-donating (ED) and electron withdrawing along the conjugated molecule, (3) optimize the π -bridge linkage length (Peters & Freeman, 1994).

A.



B.

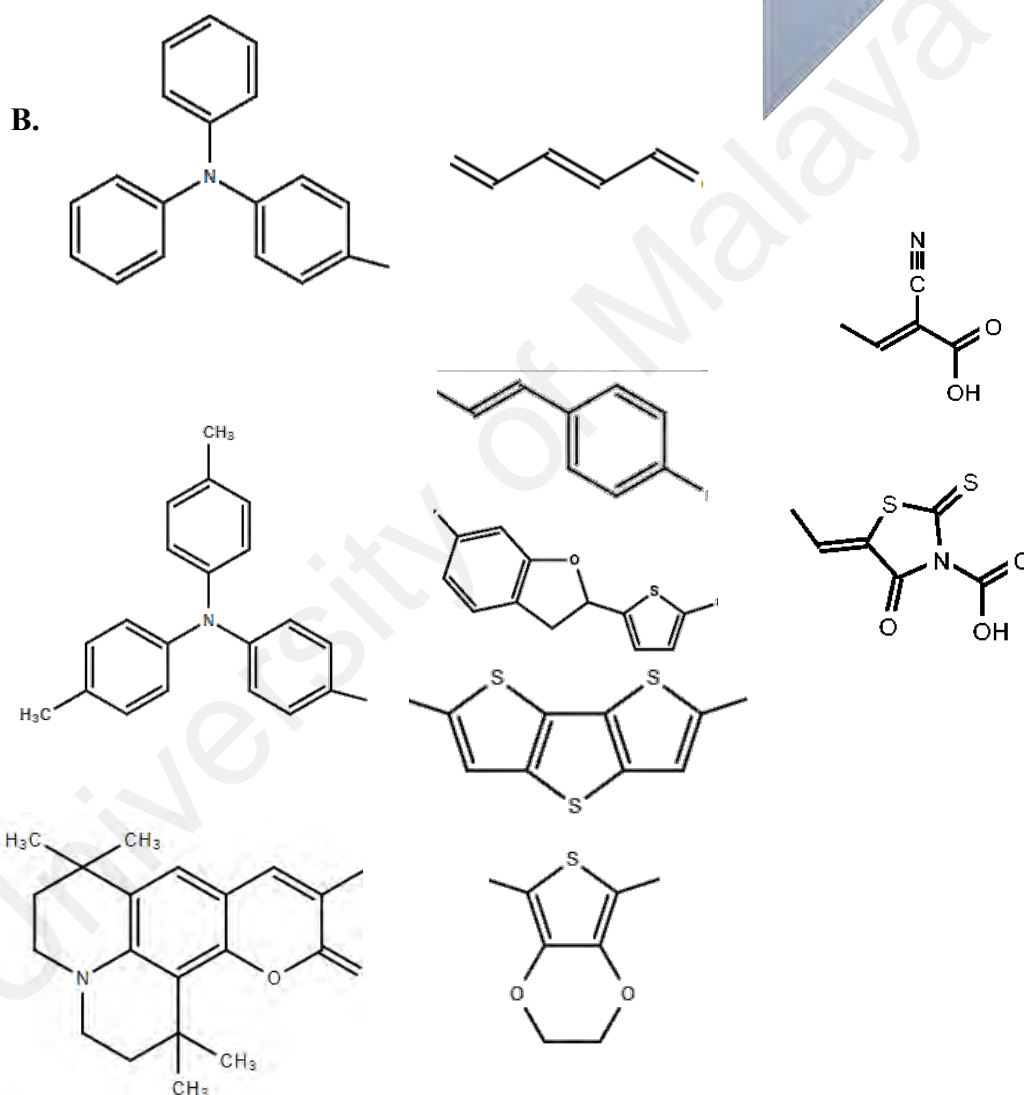


Figure 1.1: a) A scheme of D- π -A dye configuration. b) Some example of chemical groups employed for different moieties of the metal-free organic dye sensitizers.

Acceptor moiety act as anchoring unit that attach the dye sensitizer onto the surface of nanocluster semiconductor. Number of literatures have been reported with various acceptor moieties and conversion efficiency. Most of the reference dyes obtained in this thesis are designed with carboxylic group as the acceptor moieties. One significant approach in designing dye sensitizer is to include cyanoacrylic acid as part of the acceptor group. Cyanoacrylic acid act as electron withdrawing unit through the cyano-part thus, affecting the energy level of a dye sensitizer.

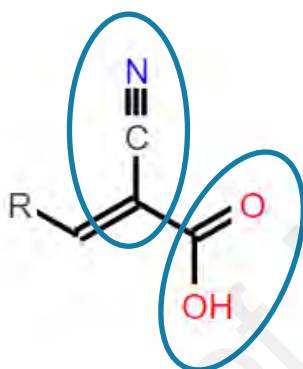


Figure 1.2: The Cyanoacrylic Acid Acceptor/ Anchoring Group.

Modification on the π -bridge linkage structure involve the extension of the conjugating bridge. However, extending the conjugating bridge beyond a certain length could restrict DSSC efficiency due to instability towards heat and light (Peters & Freeman, 1994).

This thesis employed second approach (i.e. employing electron withdrawing and donating group) to optimize band gap towards the desired feature. New substituent introduced onto reference dye will adjust the band gap of a dye sensitizer subsequently, enhance DSSC efficiency. In order to correlate in silico DSSC development and hand-in-hand experiment, the simulation method to elucidate DSSC mechanism and predictive capabilities must be strong. Hence, this thesis is inspired by the ultimate goal in silico DSSC development.

CHAPTER 2: LITERATURE REVIEW

2.1 Computational Chemistry Development

Computational chemistry has advanced in the 20th century and flourished as an emerging scientific field dealing with many complex chemical problems. Chemical problems can be solved by exploiting computational science techniques via software programs and developing codes. The fundamental principle upon which computational chemistry is built combines fundamental law of physics and mathematical expression. These two features are applied to solve chemical problems hence, the name computational chemistry. The behavior of particles on an electronic scale can be simulated, enhancing any desired property to the fullest potential. This thesis takes advantage of this interdisciplinary field on which molecular modelling are simulated by computer codes and algorithms.

Chemistry is the scientific field involving compounds comprised of atoms: explained in terms of structure, properties, composition and behavior. The molecular geometry of a compound is built as a set of three-dimensional coordinates along the Cartesian plane. The type of atoms and geometrical coordinates define the chemical structure of a molecule (Katrutzky et al., 2010; Levi, 2006). Hence, the property of a molecule is derived based on the function of their molecular geometry (Schoch, 2004; Luan et al., 2013;). One can imagine a positively charged molecule surrounded by negatively charged electrons stay intact by Coulombic forces of attraction thus, prediction of the chemical environment is made possible. The dual particle property of an electron shows both particle and wave-like characteristics. Therefore, quantum mechanics is employed to describe the light elementary particle in terms of mathematical description. The behavior of nuclei and electrons are not described by classical physics. The reason is that Newton's equation of motion (i.e. $F=ma$) fail to describe mathematical formulation for dual wave-particle property.

In the early 20th century, quantum mechanics were first postulated by mathematical expression, describing experimental observations and phenomena. Wavefunction, the fundamental postulate in quantum mechanics, is introduced to describe the state of a quantum system (Seybold et al. 1987; Sherrill, 2001). Wave function is denoted as ψ , Ψ the 23rd Cyrillic letter adopted from Greek. The wave function has no physical interpretation rather, it is a complex number which act as a function of position and time for particle (i.e. Ψ (position, time)). The complex square value of wave function gives a real number (i.e. absolute square value or $|\Psi|^2$). Based on Max Born, the complex square wave function is interpreted as the probability of finding a particle at a given position and time (Born, 1955). By all means, wave function can be determined experimentally even though it is not an experimentally measurable entity. It contains all the system information about a measurable data and observable properties. Quantum mechanics postulates that averaging a wave function acted by operator gives the physical properties of an experimental measurement (Bastard, 1990; Smith, 1991).

In 1925, an Austrian physicist named Erwin Schrödinger formulated a formula to obtain wave functions, the Schrödinger's equation (Schrödinger, 1926). Schrödinger's equation is classified into two, the time-independent equation and time-dependent equation. One need to solve the Schrödinger's equation in order to obtain wave functions. The time-dependent is analogous to the equation of motion (Newton's second law). The equation outlines the dynamic system behavior which change over time. Therefore, one finds it challenging and complicated to solve time-dependent Schrödinger's equation. Most of chemistry problems has standing wave which do not evolve with time. For a stationary state, the wave function is a function of position only. Thus, time-independent Schrödinger's equation is employed to find such state in most theoretical chemistry problem.

2.2 Dye- Sensitized Solar Cell (DSSCs)

Inspired by nature, DSSC mimic the photosynthesis mechanism in plants. The stacking of semiconducting material (e.g titanium dioxide, tin dioxide) resembles the thylakoid membrane which can be found in green leaves (Grätzel, 2011). The similar plant mechanism of charge separation and electron generation differentiate DSSC from other PV cells.

The word solar originated from Latin, sol which means sun. A solar cell can be defined as an electronic device that produce electricity upon sunlight illumination. Sunlight that strikes the surface of solar cell panel produces voltage and current, thus generating electricity. For this process to occur, a light absorbing material is needed. The material should absorb light and excite an electron to a higher state, thus, injecting the higher energy electron into the external circuit. The electron then frittered from the other end of the external circuit before returning to the absorbing material.

The basic idea of DSSC is the dye sensitization of a nanostructured semiconductor metal oxide (SMOs). The electronic band gap (E_g) of semiconducting material is about 3.0- 3.4 eV at 300K (Ahn et al., 2016), which is greater than that of commercial PV cells with 1.1 eV. Hence, SMOs alone are unable to absorb most of the solar emission due to the wide E_g . On the bright side, wide band gap SMOs hold several advantages which include inexpensive manufacturing cost, abundant raw materials and stable. SMOs are made sensitive to visible light by the sensitization of a dye.

Application of DSSCs concept to photo electrochemistry (PEC) process can be traced back to the US patent issued in 1978, reported by Chen et.al. (Chen et al., 1978). However, the conversion efficiency was very low and did not stimulate worldwide research interest. The real breakthrough of DSSC in the PEC application was in 1991 published from the work of O'Regan and Grätzel (O'Regan & Gratzel, 1991). The photo to light conversion

efficiency was enough to compete against other PV cells and other renewable energy technologies. Conversion efficiency of 10% was achieved by M. Grätzel group two years later (Nazeeruddin et al., 1993).

There has been a rapid development and dramatic increase in research interest to enhance DSSC efficiency. The greatest challenge in DSSC is to design a low E_g and thermally stable dye sensitizer. Therefore, computational method provides the best way to tackle the problem. The structural design of dye sensitizers can be made by computational prediction before going into the wet laboratory for their synthesis. By doing this, time, energy and cost are reduced much drastically.

2.2.1 Device structure

Dye sensitized solar cell comprise 5 key components which include the conducting glass substrate, the light absorber, the electron transporting material (ETM), the hole transporting material (HTM) and the counter electrode. The conventional light absorber is a monolayer of organic or inorganic dye sensitizer, responsible for charge injection upon excitation by sunlight. The ETM is a mesoporous structured of a wide band gap semiconducting material.

The HTM is a liquid electrolyte containing redox couple. In the old days, the semiconducting material were made either from silicon, cadmium sulfide or gallium arsenide. However, this kind of electrodes have undergone photo corrosion when exposed to sun light resulting in poor stability of the photo electrochemical cell. The use of titanium dioxide (TiO_2) or tin dioxide (SnO_2) nanocluster as the wide band gap semiconductor material has resulted in high chemical stability of the cell. These materials are abundant and cheap, reducing the total manufacturing cost of DSSCs.

The main component of DSSC is known as redox shuttle which consist of 3 components, a wide band gap semiconductor as the charge transfer layer, a dye sensitizer as the light absorption layer and a redox couple as the regeneration layer. The working electrode of DSSC is made up of a mesoporous SMO nanoparticle (usually a TiO_2 or SnO_2) deposited onto a conducting glass.

The conducting glass is a transparent conducting substrate coated with layer of transparent conducting oxide (TCO). TCO are generally made up of fluorine-doped tin oxide (FTO), indium tin oxide (ITO) and doped zinc oxide. The surface of the working electrode is attached with a monolayer of dye sensitizer via anchoring group of the dye, which will be discussed later in the thesis. The counter electrode of a DSSC system is also deposited onto a TCO. The counter electrode consists of an inert, catalytic and thin layer of platinum. The electrolyte system must have optimum redox potential and high interaction with the dye sensitizer. Electrolyte containing a redox couple, usually iodide/triiodide (I^-/I_3^-) ions are used to regenerate the oxidized dye.

2.2.2 Operating mechanism

Photovoltaic energy conversion follows the same mechanism as the p-n junction used in semiconductor material. The light-generated current in a PV cell involve two main processes. The first process involves the absorption of incident light comprise of photons particle. For a successive electron-hole pair generation, the energy of the incident photon should be greater than the band gap of the absorbing material in the PV cell. The holes generated in the p-type material and electron generated in the n-type material are in metastable state (excited state) and exist for a certain amount of time equivalent to the minority carrier lifetime before recombination occur. If carrier recombines faster, then no power or current can be generated.

Majority carrier is defined as the carrier with abundant charge, responsible for the transport of current in semiconducting material. In the p-type and n-type semiconductor, the carriers are hole and electron. Minority charge carrier has less charge carriers. For the p-type and n-type semiconductor, the minority charge carrier is the electron and hole respectively. Minority carriers cannot cross a semiconductor-metal boundary. In order to prevent recombination from occurring, minority carrier must be collected by the junction for a successive current flow.

Second process involves the collection of these carriers by spatially separating the electron and the hole by the action of the electric field in the p-n junction. Light-generated minority carrier is swept across the junction by the electric field at the p-n junction and has now become majority carrier. If the PV cell base and the emitter are connected, the light-generated carrier will flow through the external circuit. Figure 2.1 dictates the movement of electron-hole pair at short circuit. Redox shuttle dictates the overall operation mechanism. DSSC operates in the presence of sunlight as the energy resource. Absorption layer, dye sensitizer absorbed light which is attached onto the wide band gap semiconductor through anchoring group. Incoming photons with sufficient energy to be absorbed allow the dye sensitizer to be excited from the ground state to the excited state.



where TiO_2 is the wide band gap semiconductor, S and S^* , represents dye sensitizer at ground and excited state respectively. Since TiO_2 is by far the most employed SMO, it will be used to represent the semiconductor throughout the discussion.

Upon excitation, the excited photo sensitizer is oxidized by injecting an electron into the conduction band of the TiO_2 , and oxidation reaction takes place.



Where by, S^+ is the oxidized dye sensitizer, and e_{cb}^- , stands for an injected electron in the conduction band of TiO_2 .

Injected electrons in the TiO_2 conduction band are transported between the mesoporous nanocluster via diffusion. Eventually the injected electron is collected at the front side of transparent conducting oxide TCO through external load and wiring.

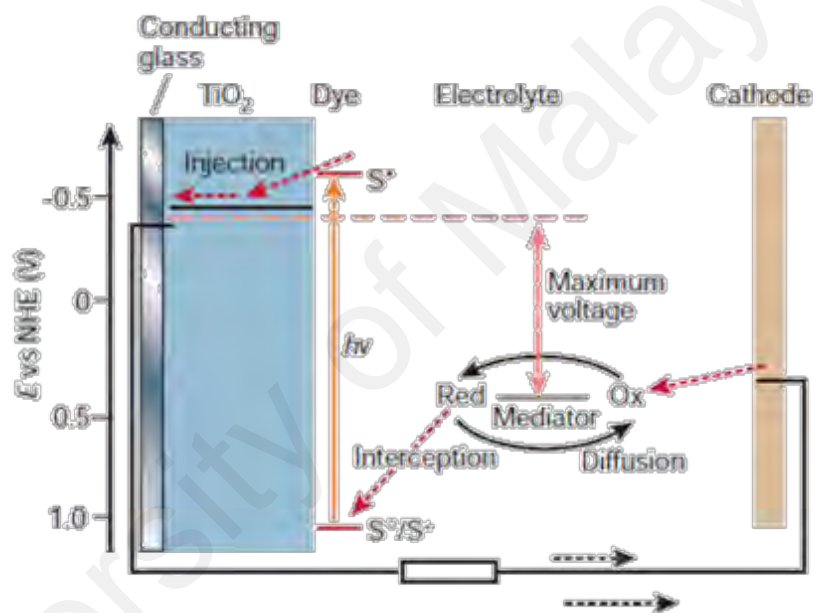
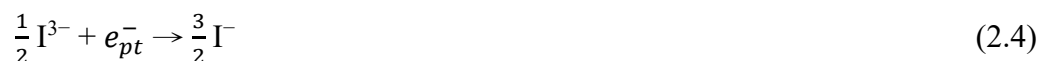


Figure 2.1: Mechanism of a DSSC system converting light to electricity (reproduced from (Gratzel, 2001) with permission of Nature Publishing Group).

The redox shuttle, usually the iodide/triiodide (I^-/I_3^-) come into play in the dye regeneration. Redox shuttle dissolved in organic solvent, donate an electron to the oxidized dye for dye regeneration.



The oxidized triiodide shuttle, I_3^- , is diffused and reduced to I^- and at the counter electrode to restart the DSSC mechanism and completes the circuit.



where, e_{pt}^{-} , refer to the electron coming in from a Pt-coated counter electrode. There are many alternatives to replace iodide/triiodide (I/I_3^{-}) as the redox mediator.

The alternative includes transition metal based complex redox system e.g. cobalt (II/III) (Kashif et al., 2013; Mathew et al., 2014; Xiang et al., 2013), copper (I/II) (Bai et al., 2011), ferrocene, and nickel (III/IV) (Li et al., 2010; Spokoyny et al., 2010)) and organic redox system e.g. nitroxide radicals (Kato et al., 2012; Lee et al., 2012), sulphur (Li et al., 2010; Tian et al., 2010), and various halogens (Ning et al., 2009; Rani et al., 2011; Teng et al., 2009)). However, recent reports have shown almost all DSSC showed high efficiency when coupled with iodide/triiodide electrolyte (Boschloo & Hagfeldt, 2009; Hardin et al., 2012; Nusbaumer et al., 2001; Qin et al., 2012).

The ability of the iodide/triiodide electrolyte to prevent loss of generated electrons by the slow interception of injected electrons at the TiO_2 and its highly efficient in dye regeneration has made it a prevalent redox shuttle in DSSCs. The only drawbacks of having iodide/triiodide as the redox shuttle are corrosiveness, inefficient dye regeneration for far-red-dye sensitizer and the impedance of open-circuit photovoltage, which limit the full potential of highly efficient dye and the cell (Boschloo & Hagfeldt, 2009; Thomas et al., 2008; Wang et al., 2010; Xiang et al., 2013; Yella et al., 2011).

2.2.3 Features of Dye Sensitizers

As for the light absorber, there are many classes of dye sensitizers. These dyes are sensitized onto the ETM semiconductor and injects electron upon excitation by sunlight. Dye sensitizer can be classified into metal-based complexes (inorganic) and metal-free (organic) dyes. The N719 with 11.2% efficiency (Nazeeruddin et al., 2005), black dye with 10.4% efficiency (Nazeeruddin et al., 2001), and N3 with 10% efficiency (Nazeeruddin et

al., 1993) exhibit superior performances over other dyes and are perhaps, the most outstanding class of the metal-based sensitizers.

The ultimate property that make these dyes perform efficiently are attributed to their stability, longer exciton lifetime and the ability to absorb broad range of light through metal-ligand charge transfer (MLCT) (Chung, & Kim, 2013). The demand for metal will skyrocket resulting in dramatic rise in price within the next decade. Metal free organic dye sensitizer appear to be the alternative as it holds several advantages over the metal-based complexes dye based on the following list:

- Inexpensive preparation and manufacture cost (Heredia et al., 2010; Yang et al., 2006; Pastore et al., 2010),
- Flexible molecular design and tunable optical properties (Pastore, et al., 2010),
- Free from rare metals such as ruthenium because organic dyes are biodegradable and do not cause environmental issues (Kim et al., 2013),
- Higher molar absorption or extinction coefficient, a degree of how strong a chemical species absorb light at a specified wavelength. Unlike metal-based dyes, a high molar extinction coefficient organic dye allow the use of thinner layer of ETM semiconductor without disrupting the light harvesting efficiency (Heredia et al., 2010; Li et al., 2006; Pastore et al., 2010),
- Wide application such as the suitability for multi-colour solar cells that serve as power producing building (Heredia et al., 2010).

Due to various attractive properties of organic dye sensitizer, these dyes are investigated and developed intensively. Organic dye sensitizer contains different functional group in their structure such as fluorine, carbazole, coumarin, indoline, merocyanine and triphenylamine.

Despite these features, organic dyes are less stable and less efficient compared to their counterpart, inorganic dye. The efficiency recorded for metal free DSSC range around 5%, far inferior from inorganic dye with 14.3% efficiency (Lee et al., 2017)

The low efficiency of organic dye is hampered by several factors: (a) photochemical degradation that relates to instability of dye; (b) narrow absorption of light in the visible wavelength region; (c) self-quenching due to dye aggregation; and (d) shorter exciton lifetimes. One of the research objectives is to improve the efficiency of organic dye sensitizer.

Organic dye efficiency is increased by improving the absorption profile, enabling it to absorb sunlight better at near infrared region. This thesis will address relevant steps in developing a high efficiency organic dye sensitizer. There are various processes, characteristics, and material that can potentially produce an ideal sensitizer.

An ideal sensitizer is a dye sensitizer that satisfy the requirements for a full photovoltaic energy conversion. Ideally, it should absorb light in the whole visible and the near infrared region (NIR). The threshold wavelength should be around 920 nm (Agrawal et al., 2012; Grätzel, 2003; Hagfeldt et al., 2010). There has been no dye that can absorb light in the whole visible and NIR range.

2.2.4 Photovoltaic Cell Parameters

Current and voltage combination output of a PV cell is indicated by the current-voltage (*IV*) curve. In the absence of light, a PV cell has the same electrical characteristic as a large diode. Current, expressed in symbol I , is on the vertical y -axis and voltage in symbol V , is on the horizontal x -axis. Upon sunlight illumination, the *IV* curve shifts downward as *PV* cell begins to generate power. Light affect the shifting of the *IV* curve down. The greater

the amount of light, the greater the amount of shift. Maximum current is achieved when there is zero resistance in the circuit.

This maximum current is a short circuit between the positive and negative terminal and is abbreviated to I_{sc} . When the device is short circuit, the voltage is zero. Maximum voltage is achieved when there is a break in the circuit, an infinitely high resistance and when there is no current flow. This is called the open circuit voltage, V_{oc} .

In other word, the I_{sc} point is on the y -axis when the voltage is zero while the V_{oc} point is on the x -axis, when the current is zero. The power available for a PV device is indicated along the I - V curve, a product between current and voltage expressed in watts. A maximum power point is achieved at the knee of the curve, a maximum product of current-voltage. Figure 2.2 illustrate the relationship between current, voltage and power of a PV cell.

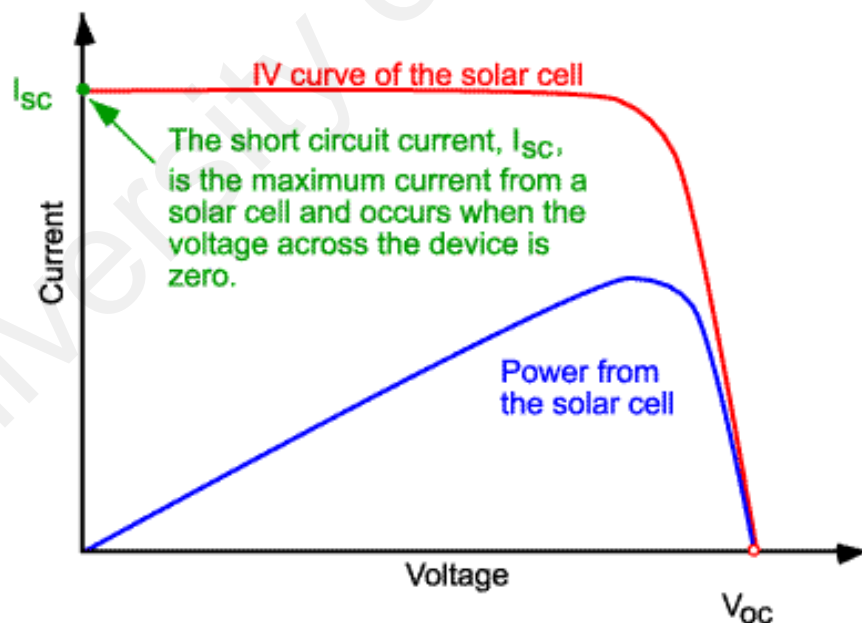


Figure 2.2: Current, Voltage and Power relationship in photovoltaic cell.

The collection and production of light-generated carrier results in short-circuit current. Hence, the largest current drawn from a device is the short-circuit current. The short-circuit current is dictated by several factors (Sawyer, 1986):

- The surface area of a PV cell. It is common to denote short-circuit current density (J_{sc} in mA/cm²) in PV cell rather than short-circuit current, I_{sc} ;
- The number of incident photons since I_{sc} is proportional to light density;
- The incident light spectrum. The spectrum for a PV cell is standardized to AM1.5
- The optical properties of the surface of a PV cell such as reflection and refraction; and
- The minority carrier lifetime and surface passivation which affects the collection probability of the PV cell.

Surface passivation and diffusion length are the critical parameter when comparing PV cells of the same material. For a perfect passivated surface, the short circuit current density can be approximated as:

$$J_{sc} = qG (L_n + L_p) \quad (2.5)$$

where G denotes generation rate, L_n and L_p are the diffusion lengths for electron and hole respectively.

The assumption for this equation does not fit the true condition encountered in *PV* cells nevertheless, shows the strong dependence between generation rate, diffusion length and short-circuit current density, J_{sc} . The light absorption of dye sensitizer into near infra-red region can increase the short-circuit current density, J_{sc} . To better understand this

mechanism, photon flux needs to be taken into consideration. Photon flux is defined as the number of photons per unit time per unit surface area:

$$\Phi = \frac{n_{\text{photon}}}{t \times A} \quad (2.6)$$

Where Φ denotes photon flux, n_{photon} is the number of photons, t , is time expressed in unit seconds and A is surface area expressed in unit m^2 . The photon flux can measure the electrical current produced from a *PV* cell by determining the number of electrons generated. Multiplying photon flux with the energy of a photon gives the power density. Power density can be obtained from the following equations:

$$P \left(\frac{W}{m^2} \right) = \Phi \times \frac{hc}{\lambda} \quad \text{using SI units.} \quad (2.7)$$

$$P \left(\frac{W}{m^2} \right) = \Phi \times q \frac{1.24}{\lambda (\mu m)} \quad \text{for wavelength in } \mu m. \quad (2.8)$$

$$P \left(\frac{W}{m^2} \right) = \Phi \times qE \text{ (eV)} \quad \text{for energy in eV.} \quad (2.9)$$

Since the radiant power density is calculated by the product of energy of incident photons and the number of photons expressed in photon flux, more photons are needed for a photon in the red-light region. In other word, for the same amount radiant power density in both red and blue light, more red photons are needed since each one has less energy. Figure 2.3 illustrates the relationship of photon wavelengths against photon flux density on earth surface. The figure is reproduced based on reference (Kim et al., 2013).

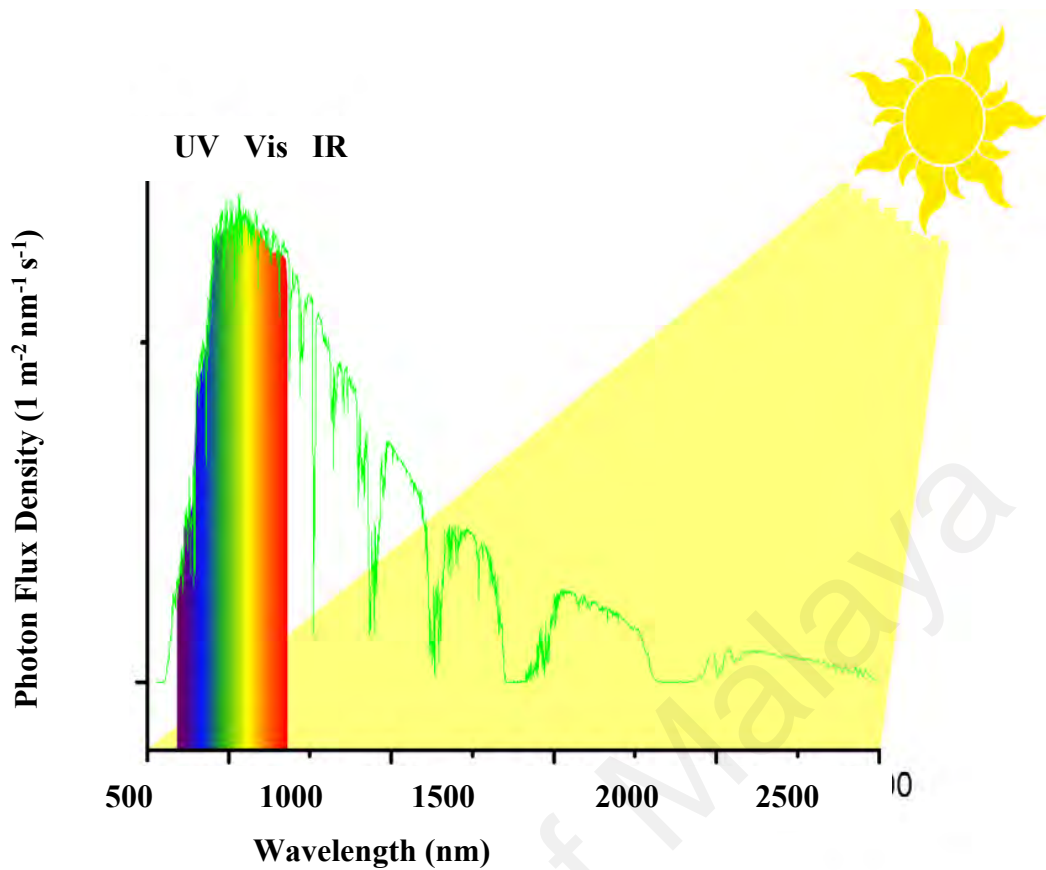


Figure 2.3: Photon wavelengths and radiant photon flux density relationship.

From the figure above, there is an uneven distribution of harvesting degrees. The highest photon flux density is obtained in the 600-800 nm region. The dependency of current density and degree of harvested light expressed in wavelength is summarized in Table 2.1, data are reproduced from reference (Kim et al., 2013).

From Table 2.1, it can be understood that for a dye sensitizer to absorb all radiation from a 280-550 nm wavelength region, a maximum current density of 5.1 mA cm² will be generated. However, if the dye sensitizer absorbs a smaller part of the long wavelength region, then it is sufficient to covers a higher photon flux density region and able to generate more current density (Kim et al., 2013).

Table 2.1: The Dependency of Harvested Light and Current Density Expressed in Terms of Wavelength.

Wavelength (nm)	Maximum Percentage of Harvested Light (from 280 nm)	Current Density (mAcm ⁻²)
500	8.0	5.1
600	17.3	11.1
700	27.6	17.6
800	37.3	23.8
900	46.7	29.8

For instance, if the dye covers the 700-800 nm, calculated as 23.8 mA cm⁻²-17.6 mA cm⁻², it can generate 6.2 mA cm⁻² of current density. Hence, the optical band gap of a dye should be adjusted to fall onto the optimum absorption range that provide the maximum photon flux region in the solar spectrum.

This clearly shows the relationship between dye sensitizer band gap, degree of absorption range of dye and expected current output (Dessi et al., 2014).

Since extending the absorption range in the long wavelength region increases current output, the short-circuit current density, J_{sc} is also affected thus, increasing the overall solar conversion efficiency, η according to the following equation:

$$\eta = \frac{J_{sc} \times V_{oc} \times FF}{P_{in}} \quad (2.10)$$

where V_{oc} is the open-circuit voltage parameter, FF is the fill factor and P_{in} is the total incident solar power of the cell (Thomas et al., 2008).

Another aspect that affect the performance of DSSC is the physical stability of the dye sensitizer. The dye should grasp firmly onto the glass substrate of semiconductor oxide (SMO) surface (Hagfeldt et al., 2010; Thomas et al., 2008).

Arrangement of dye is crucial in avoiding aggregation. Aggregation occur when the dye sensitizer is flat and stack on top of one another. This leads to self-quenching, a phenomena where by electron is being injected between sensitizers instead of towards SMO (Connick et al., 1999).

Stability of organic dye has been questioned for many years. This is because organic dyes are less stable towards heat and light compared to inorganic dyes. For an ideal organic dye to operate, it should have 110 turnover cycles of operation. This equals to 20 years of operation under natural light (Luque & Hegedus, 2011).

The lowest unoccupied molecular orbital (LUMO) is often regard as the excited-state energy of the dye sensitizer. In order to generate photocurrent density, the LUMO must be higher in energy than the *n-type* semiconductor oxide conduction band edge.

Both LUMO and the underlying semiconductor oxide must be strongly coupled and energetically matched for a high quantum injection efficiency (A. Becquerel, 1839; Luque & Hegedus, 2011; Williams, 1960). The highest occupied molecular orbital (HOMO) energy manifested as the ground-state energy of the dye sensitizer must lie below the hole conductor (redox shuttle) energy.

This is to allow the oxidized dye to be regenerated via electron donation from the holes conductor (Ehrlich & Ehrlich, 2008; Einstein, 1905; Luque & Hegedus, 2011; Schiermeier et al., 2008; Greenspan, 2005).

2.3 Squarine Dye

For the past decades, the center stage of research for both technological and fundamental viewpoint has focused on squarine chemistry. The reference squarine dyes are a class of successful organic sensitizer in DSSCs. They are famous for their high molar absorption coefficient and conjugated zwitterionic-like structure. This feature separates squarine dye from other near infra-red dyes. The resonance stabilized structure of squarine is made up of donor-acceptor-donor (D-A-D) structure, containing two electron-donating groups and a central four membered ring which act as the electron deficient group. Number of theoretical investigations have been performed on squarine dye and suggested that the singlet S_0 - S_1 electronic excitation represents charge transfer transition.

This is because there is a significant intermolecular charge transfer (ICT) involved in both ground and excited singlet states. The p-electron extension from donor moiety combined with the ICT transition feature gives the high molar extinction coefficient in the near infra-red and visible-light region spectrum (Ramamurthy, 1997).

The formation of squarine dyes were first reported by Triebs and Jacob upon reaction of squaric acid and pyrrole in 1965 (Triebs & Jacob, 1965). Since then, numerous literatures have highlighted the potential application and essential synthesis pathway of squarine dyes (Sprenger & Ziegenbein, 1967). In general, squarine dyes can be prepared by introducing squaric acid with heterocyclic compounds such as phenols, benzotiazoles, imidiazoles, *N,N*-dialkylannilines and pyrroles. The typical absorption and emission spectra of squarine dye usually falls in the 500-650 nm region. Figure 2.4 illustrates the absorption and emission spectra of *N,N*-dimethylaniline derivative squarine dye in CH_3Cl solution.

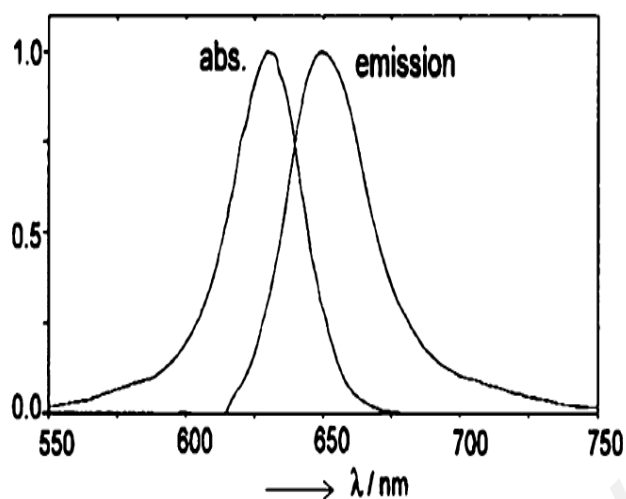


Figure 2.4: Absorption and emission spectra of N,N-dimethylaniline derivative squaraine dye immersed in CH₃Cl solution (reprinted from reference with permission from American Chemical Society©, 1997).

Squaraine dyes are dominant in solar cell applications due to their remarkably high molar absorption coefficients in the near-infrared and visible light region. Despite the high molar absorption coefficient, squaraine displayed a low conversion efficiency. This is mainly due to the stacking dye arrangement and aggregation that consequently resulted in self-quenching of the organic sensitizer (Kanaparthi et al., 2012).

Self-quenching is identified as back electron transfer onto neighboring compound of a same species. In this case, the electron transfer occurred between dye sensitizers instead of injecting electron into the semiconducting metal oxide (SMO). Low thermal stability stress and photo-stability pose another disadvantage of using squaraine as dye sensitizer.

Symmetrical squaraine dye has been investigated in the field of solar cell application by Kaman in 1993 (Kaman et al., 1993). They observed a very low conversion efficiency (0.05 - 0.7 %) due to the very low singlet fluorescence quantum yields and high number of dye aggregation which leads to self-quenching (Das et al., 1994).

Squaraine dye is further developed and displayed a better conversion efficiency of 2.17%, a research done by Zhou et.al (Zhou et al., 2011). The overall conversion efficiency improved dramatically due to the enhanced adsorption of dye sensitizer onto SMO films. Despite the low efficiency displayed by most squaraine dye, molecular engineering is able to enhance photosensitizer performance and stability under standard illumination condition.

There are many possibilities to design squaraine dye as photosensitizer due to number of heterocyclic systems which give variable donor strength and π -bridge conjugation length. Tunable optical properties can be adjusted to match their application in photonic devices.

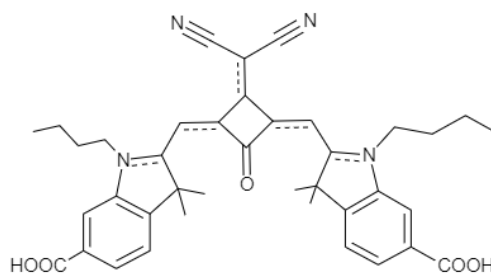
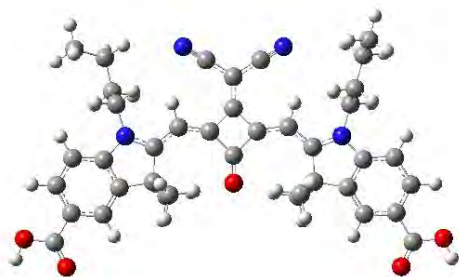
Taking advantage on technology, processor and computer advancement, computational chemistry enables squaraine photosensitizer to be developed in-situ, testing their potential application in DSSC. The common idea of this research is to focus on photosensitizer unique conjugation pattern and observe charge transfer band directionality in the excited states.

Four unsymmetrical squaraine dyes are taken from literature as part of the structure-relationship investigation. They are SQ01, SQM1b, MSQ and VG13. Three reference dyes are chosen for their symmetrical structure, they are VG1, SQM1a, and VG10. (Park et al., 2012).

This structure-property relationship is further developed in 2014 and 2 new dyes have been reported, VG13 and VG10 (Park et al., 2014). X-ray crystallography of SQM1a from the work of Maeda et al. (2013) is taken to compare the conformational parameter between experimental and theoretical photosensitizers (Maeda et al., 2013).

They elucidate conformational effect of photosensitizer by comparing symmetrical SQM1a dye with unsymmetrical dyes, SQM1b and MSQ (Maeda et al., 2013). X-ray crystallography can be used to map theoretical dye onto the potential energy surface by varying density functional or Hartree-Fock (HF) exchange parameter. Symmetrical and unsymmetrical squarine dyes are illustrated in Figure 2.5 and Figure 2.6 respectively.

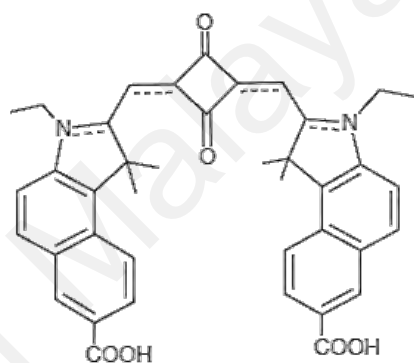
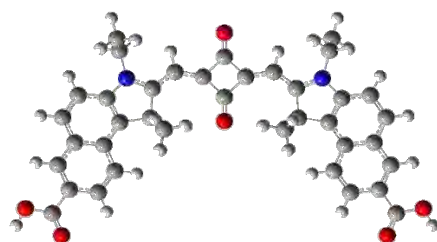
University of Malaya



HOMO = - 5.44 eV

LUMO = -3.71

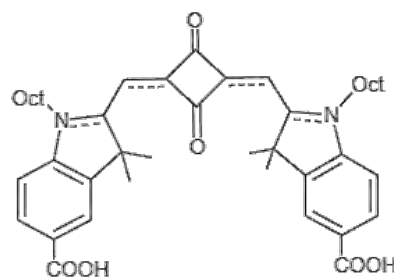
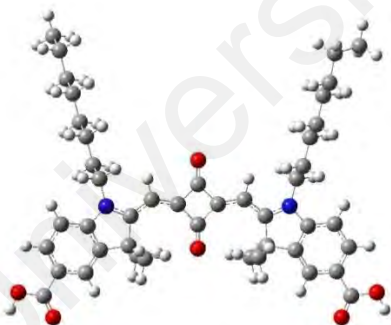
SQM1a



HOMO = -4.56 eV

LUMO = - 3.00 eV

VG10



HOMO = - 4.66 eV

LUMO = -3.07 eV

VG1



Oxygen



Nitrogen



Carbon



Hydrogen

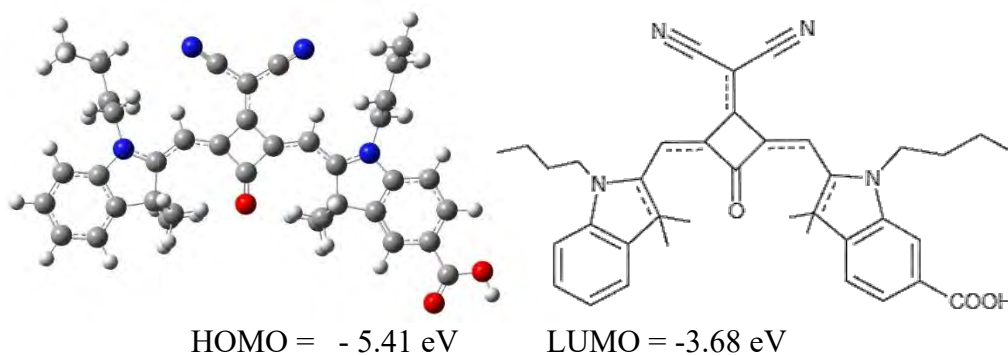
O – Oxygen

N – Nitrogen

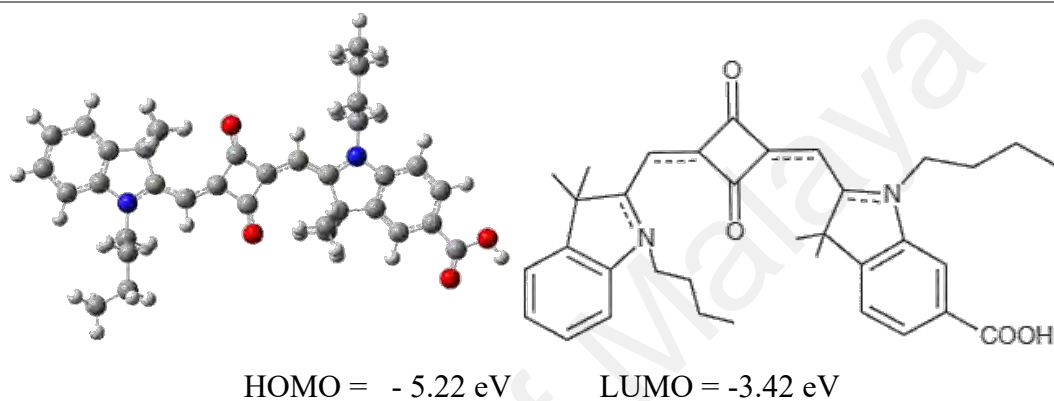
COOH- Carboxylic acid

Oct- Octyl

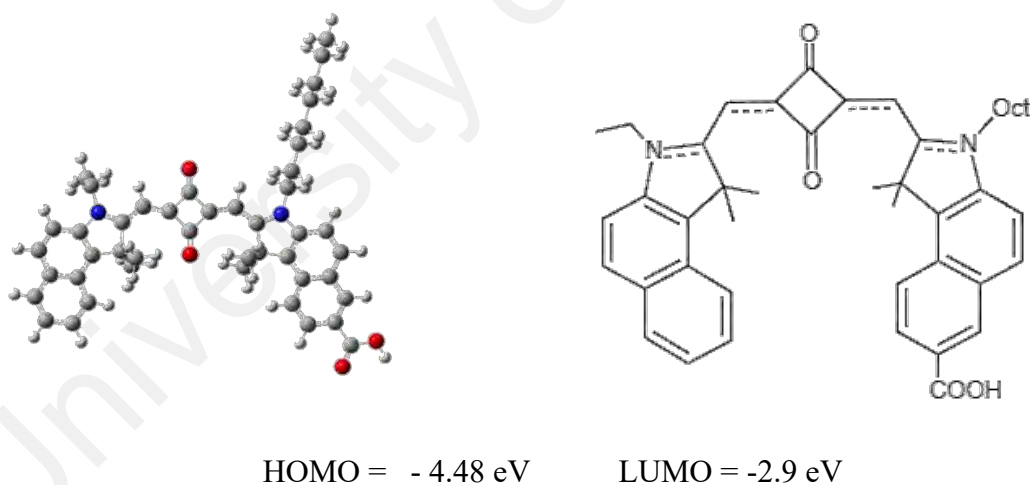
Figure 2.5: Symmetrical Squaraine Dyes.



SQM1b



MSQ



VG13

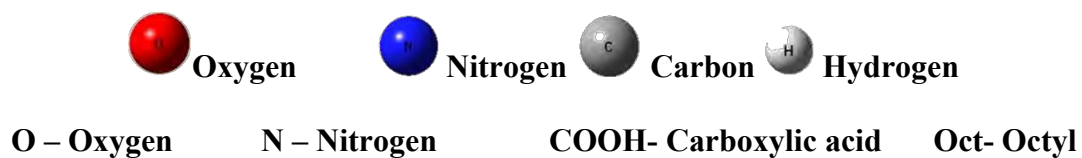
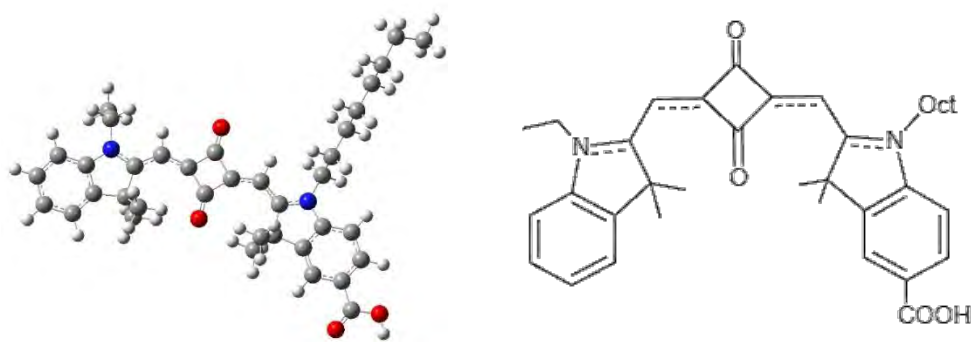


Figure 2.6, continued.



HOMO = - 4.61 eV

LUMO = -3.32 eV

SQ01



Figure 2.6: Unsymmetrical Squaraine Dyes.

2.4 Structure modification based on Dewar's Rule

7 push-pull photosensitizers are chosen as backbone reference dye for the development of new dyes through π -bridge modifications. Engineering of new dyes will follow Dewar's rule guidelines (Dewar, 1952). Perturbation molecular orbital (PMO) is employed by Dewar in 1952 for semi-quantitative/qualitative analysis of organic chemistry.

Based on Dewar's rules, electronegativity is experienced in alternate position of a D- π -A chromophore with π -conjugated spacer along the charge transfer direction. There is a systematic pattern on the triangular relationship between molecular energy levels, substituent group species and their position on the π -conjugated spacer.

Numbers of electron-withdrawing (EW) and electron-donating (ED) are introduced along the π -conjugated spacer. New dyes are developed by the substitution of EW and ED substituent takes on an alternating position along the π -conjugated indolenine bridge.

DFT and TD-DFT are employed to evaluate the frontier molecular energy levels, shifting of electronic absorption spectra and molecular geometry of new dyes. This will affect the highest occupied molecular orbital (HOMO) and lowest unoccupied molecular orbital (LUMO) energy levels thus, reducing the band gap, which is the most desirable property of efficient dyes.

Based on Dewar's rules, the alternate position of a chromophore compound with π -conjugated bridge is indexed as "starred" and "unstarred". According to PMO, an increased in HOMO energy is exhibited when *ED* group is substituted onto starred position of a chromophore (Hung et al., 2010).

On the contrary, *EW* group substitution onto unstarred position along the π -conjugated bridge decreases LUMO energy level. Reduction of HOMO-LUMO energy gap can be achieved when both of *ED* and *EW* groups are substituted onto starred and unstarred position. Hence, a bathochromic shift is observed.

Bathochromic shift is desirable in DSSC. A smaller energy is needed to excite an electron. Also, small band gap corresponds to an increased in photocurrent density, J_{sc} which ultimately increase the overall dye efficiency. Therefore, a new dye can be constructed based on the substituent inserted along the π -conjugated bridge.

New dye with *ED* substituent on starred position will move HOMO energy upward, closer to LUMO as compared to original dye. Alternatively, new dye can also be constructed with *EW* substituent on unstarred position, which bring down LUMO energy level. Based on this theory, new dye can be rationally designed with reduced band gap.

Therefore, this study is designed to construct new dye structure theoretically based on Dewar's rule as a guideline. Desired property is obtained through substitution of electron donating or electron withdrawing group at possible position along π -conjugated bridge of the original squaraine dye.

2.5 Computational prediction for dye

Since DSSC involve excitation of electrons, deep calculation on electron and nuclei are compulsory in modelling dye sensitizer. The dual-wave particle behaviour of an electron that shows particle and wave characteristic are described by quantum mechanics. Classical Newtonian equation of motion approach is invalid in simulating DSSC device because it has failed to delineate nuclei and electron behaviour.

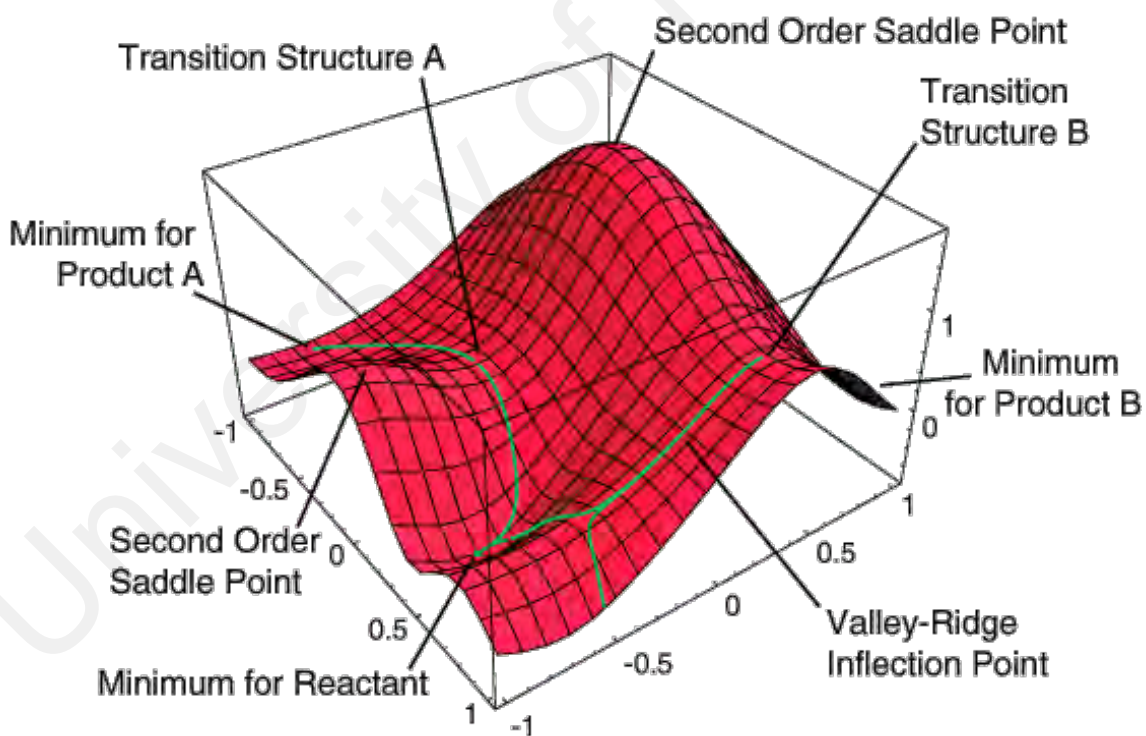


Figure 2.7: Potential Energy Surface Diagram.

Potential energy surfaces (PES) associates an energy with each geometry of a molecule. Equilibrium molecular structures corresponds to the positions of the minima in the valleys on a PES. In other word, it has achieved a stable geometry at the ground

state, optimized geometry. Based on figure 2.7, optimized geometry is achieved when the investigated compound has reached minimum energy level at 'Minimum for Product A'. Once at optimized geometry, bond length and angle displayed experience minimum external forces, giving an approximate true bond length and angle. Not only optimized geometry outline bond length and angle, type of functional group, chemical reactivity and many more properties can be extracted out.

The shape of the valley around a minimum determines the vibrational spectrum. Hence, theoretical Infra-Red (IR) spectrum can be simulated by analyzing the shape of the valley. IR reading obtained from calculation describe the type of functional group in a molecule. This chapter does not elaborate on the theoretical derivation and foundation of computational chemistry. Instead, general important molecular properties and calculation procedure to obtain them are highlighted.

All calculation in this study are obtained using Gaussian 09 software (Gaussian 09, 2009). As mentioned earlier, simulating DSSC system must be done in electronic level. Hence, for a multi electron system, Hartree-Fock approach is one method of solving Schrodinger equation by breaking down complex system to a set of one electron system (Slater, 1951). A severe approximation is to consider each electron is influenced by other electrons and nuclei fields, ignoring the influence from opposite electron spin that might affect its motion (Hartree, 1928).

By applying to the successive hydrogen atom theory, a function centered on each nucleus can be constructed. The function is denoted as wavefunction, Ψ represented by the Greek symbol, 'psi'. Parameters in Hartree-Fock calculation that describe the type and orbital exponents are known as basis set. For atomic functions, denoted as χ_{μ} , they are defined by using linear combination of gaussian functions. In order to construct an atomic function, number of primitives also known as gaussian functions, $g_p(\zeta, r)$ are

required. Typically, 6 gaussian functions are required in the core region and 1 in the valence region of an atomic function. Therefore,

$$\chi_{\mu} = \sum_p d_{\mu,p} g_p(\zeta, r) \text{ Where } g_p(\zeta, r) = c x^n y^m z^l e^{-\zeta r^2} \quad (2.11)$$

Where $d_{\mu,p}$ is defined as the gaussian primitive g_p fixed constant for a given atomic orbital χ_{μ} . The orbital exponent, ζ , responsible for the compression or diffusion of each gaussian function. The function is normalized by coefficient c in a way that the component over all space, or the integral of its square is 1: $\int g^2 = 1$. While the exponents on x, y and z define the shape of an atomic function namely the s, p, d , and f orbital. Each element is separated with different basis function.

2.6 Hartree-Fock Theory

In 1928, Hartree and Fock, performed a trial wavefunction based on the variational theorem (Hartree & Fock, 1928). The energy derived using Lagrange multipliers method, a method of finding the set of orthonormal spin orbital. As a result, Fock equation is known, derived from an eigenvector of a single determinant wavefunction that best describe the possible molecular spin:

$$\hat{F}\Phi_i = \epsilon_i \Phi_i \quad (2.12)$$

Where the Fock operator, \hat{F} , is an effective one-electron Hamiltonian for an orbital. The eigenvalue, ϵ_i are referred to as orbital energies. In this formulation, each orbital sees the average distribution of all other electrons. Using atomic units, the Fock equation can be further elaborate as follows:

$$\hat{F}\Phi_i = \hat{T}\Phi_i + \hat{V}_{NE} + \hat{J}\Phi_i - \hat{K}\Phi_i = \epsilon_i \Phi_i \quad (2.13)$$

Where by, $\hat{T}\Phi_i$ is the kinetic energy operator,

$$\hat{T}\Phi_i = -\frac{1}{2}\nabla^2 \quad (2.14)$$

\hat{V}_{NE} , is the nuclear-electron attraction operator,

$$\hat{V}_{NE} = \sum_A^{nuclei} \frac{-Z_A}{r_{iA}} \quad (2.15)$$

$\hat{J}\Phi_i$, is Coulomb operator,

$$\hat{J}\Phi_i(1) = \left\{ \sum_j^{occupied} \int \Phi_j(2) \frac{1}{r_{12}} \Phi_j(2) \delta\tau_2 \right\} \Phi_i(1) \quad (2.16)$$

$\hat{K}\Phi_i$, is the exchange operator,

$$\hat{K}\Phi_i(1) = \left\{ \sum_j^{occupied} \int \Phi_j(2) \frac{1}{r_{12}} \Phi_j(2) \delta\tau_2 \right\} \Phi_i(1) \quad (2.17)$$

$\hat{T}\Phi_i$ represents the kinetic energy of an electron, while \hat{V}_{NE} accounts for the attraction of an electron has for each of the nuclei. The Coulomb operator, $\hat{J}\Phi_i$, represents the coulombic repulsion between an electron and the charge distribution created by another electron.

The $\hat{K}\Phi_i$ operator represents the exchange term: a non-local quantity present as a result of the anti-symmetry requirement of the wavefunction. Notice that the electrons are labeled 1 and 2 to identify the coordinates of the integration. They could be any two electrons of the system.

The summations are over all the occupied spin orbitals. Note that self-interaction and self-exchange are included and cancel one another out since the two integrals are equivalent when $i = j$. It is clear from the two integral quantities that the Fock operator itself depends on the orbitals in order to be evaluated. This unique feature of the equations

requires us to solve them iteratively, using a process known as the self-consistent field (SCF) approach. The computation process is illustrated on the figure 2.8 below.

Steps involving Hartree-Fock calculation is summarized in flowchart as illustrated in figure 2.8. The first assumption is made for HF calculation in which wavefunction is written as products of HF, HP:

$$\Psi_{HP}(r_1, r_2, \dots, r_n) = \Psi_1(r_1)\Psi_2(r_2) \dots \Psi_n(r_n) \quad (2.18)$$

Where molecular orbital, Ψ_i is defined as the individual one-electron wavefunction. Based on Eq. 10.0, $\psi_i(\mathbf{r})$ is a function for spatial coordinate of single electron, thus defined as spatial orbital. Since electron possessed fermion property and having more than three spatial coordinate, spin coordinate should be included, ω . Inclusion of space-spin coordinate results in:

$$\Psi_{HP}(x_1, x_2, \dots, x_n) = \chi_1(x_1)\chi_2(x_2) \dots \chi_n(x_n) \quad (2.19)$$

In which the set of space-spin coordinates is $x = \{r, \omega\}$ and spin variable is defined as ω that can have a spin up (α or \uparrow) or spin down (β or \downarrow) value. Function of space and spin coordinate for single electron is denoted as spin orbital, $\chi(x)$.

Antisymmetry principle is another quantum mechanics postulate stating that “for a fermions system, the wavefunction must be antisymmetric with respect to the interchange of all (space and spin) coordinates of one fermion with those of another” (Sherrill, 2001).

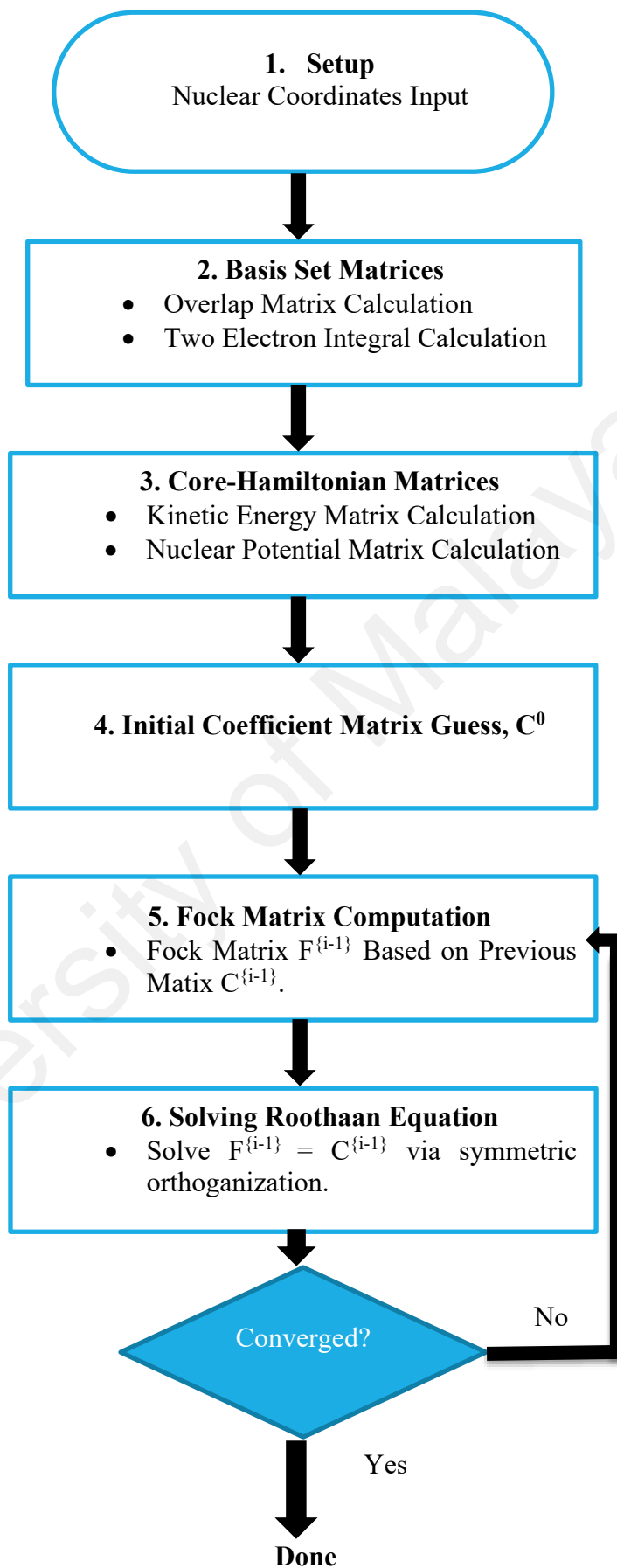


Figure 2.8: Gaussian Algorithm for Self-Consistent Field (SCF).

This gives rise to Pauli exclusion principle which states that no two or more identical fermions (two or more) can have the same quantum state simultaneously.

Slater determinant, SD introduced by John Slater can be built to satisfy an antisymmetric solution (Slater, 1929):

$$\Psi_{SD}(x_1, x_2, \dots, x_n) = \frac{1}{\sqrt{N!}} \begin{bmatrix} \chi_1(x_1) & \chi_2(x_1) & \cdots & \chi_n(x_1) \\ \vdots & \vdots & \ddots & \vdots \\ \chi_1(x_n) & \chi_2(x_n) & \cdots & \chi_n(x_n) \end{bmatrix} \quad (2.20)$$

From SD in equation 2.20, single-particle wave function is normalized as χ_i s are normalized respectively for every particle. For a determinant to be non-zero. All single particle wave function must be different. Thus, confirming Pauli's Exclusion principle. The exchange between two fermions as a result of sign change is obtained by the interchange of two rows or columns. All electrons are indistinguishable since each column correspond to orbital function (x_1, x_2, \dots, x_N).

Integration on spin variable with assumption that electrons with doubly occupied spatial, i.e. closed-shell system yield electronic energy of Slater determinant wavefunction in terms of spatial orbital:

$$E_{SD} = 2 \sum_{i=1}^{\frac{N}{2}} h_i + \sum_{i=1}^{\frac{N}{2}} \sum_{j=1}^{\frac{N}{2}} (2J_{ij} - K_{ij}) \quad (2.21)$$

Where the kinetic and nuclear attraction energy of an electron in orbital is denoted as h_i and expressed as:

$$h_i = \int \Psi_i^*(\mathbf{r}) \hat{h} \Psi_i(\mathbf{r}) d\mathbf{r} \quad (2.22)$$

$$\hat{h} = -\frac{1}{2} \nabla^2 - \sum_{A=1}^M \frac{Z_A}{|r-R_A|} \quad (2.23)$$

Based on equation 2.21, electrostatic interaction energy or Coulomb energy, J_{ij} and Exchange interaction energy, K_{ij} of electron between orbital Ψ_i and Ψ_j are derived as follow respectively where both J_{ij} and K_{ij} are positive:

$$J_{ij} = \iint \frac{|\Psi_i(r_1)|^2 |\Psi_j(r_2)|^2}{r_{12}} dr_1 dr_2 \quad (2.24)$$

$$K_{ij} = \iint \frac{|\Psi_i^*(r_1)\Psi_j(r_1)|^2 |\Psi_i^*(r_{12})\Psi_j(r_2)|^2}{r_1} dr_1 dr_2 \quad (2.25)$$

The exchange interaction energy arose as a consequence of anti-symmetry effect. Also, exchange term is applied in only in orbital Ψ_i having the same spin in neighbouring orbital, Ψ_j . Therefore, HF solution is obtained from the first approximation that the interaction between electrons are independent. The only interaction considered is the exchange interaction energy. Electron correlation is not taken into consideration in HF theory thus, providing poor electronic structure description.

Hartree-Fock ab initio calculation is dependent on the number of electrons. Also, electronic structure calculation approach is based on the electronic wavefunction, which depends on three spatial coordinate and spin coordinate. The higher the number of electrons involved in the system, the higher is the calculation complexity, thus increases complexity increases exponentially.

2.7 Density Functional Theory

Ab initio calculation can be proceeded by Density Functional Theory (DFT). Rather than obtaining properties of interest via wavefunction, DFT calculation are based on ground state and excited state electron density. Hence, DFT is independent on the number of electrons which makes it simpler than HF approach.

X-ray fluorescent, electron diffraction and X-ray diffraction analysis provide electron density measurement (Zhou, 2013). Since DFT is based on electron density calculation, an experimental data can be compared, thus providing experimental observable as opposed to wavefunction which derived from quantum postulate and mathematic expression.

DFT calculation stands on the firm theoretical basics of two Hohenberg–Kohn theorems. The first theorem states that for a given ground state electron density, $\rho_0(\mathbf{r})$ the total electronic energy, E_{el} can be determined (Martin & Martin, 2004; Nava, 2005).

Based on Born-Oppenheimer approximation, the nuclear attraction energy is defined as external potential $V_{ext}(\mathbf{r})$. Nuclei are bigger than electron thus, fixed and exert their Coulomb potential energy on to electrons, thus the term external. Therefore, the total electronic energy can be expressed as follow(Nava, 2005):

$$E_{el}(\rho) = V_{ee}(\rho) + T(\rho) + V_{Ne}(\rho) = F_{HK}(\rho) + \int V_{ext}(\mathbf{r}) \rho(\mathbf{r}) d\mathbf{r} \quad (2.26)$$

where universal functional denoted as $F_{HK}(\rho)$ contain the electron-electron repulsion potential energy $V_{ee}(\rho)$ and electron kinetic energy, $T(\rho)$. $F_{HK}(\rho)$ is independent on external potential.

The nuclei-electron attraction is a derivation of external potential and represented by the term $V_{Ne}(\rho)$. Based on HF theory, the $V_{ee}(\rho)$ can be expressed in two parts, that is charge distribution of a classical Coulomb energy, $J(\rho)$:

$$J(\rho) = \frac{1}{2} \iint \frac{\rho(\mathbf{r}_1)\rho(\mathbf{r}_2)}{r_{12}} d\mathbf{r}_1 d\mathbf{r}_2 \quad (2.27)$$

Energy term that accounts for spin correlation effect arose from anti-symmetrization, the non-classical exchange-correlation energy term, $Exc'(\rho)$ (Cuyper & Bulte, 2001; Jensen, 2017). Variational principle for DFT is established in second theorem. According to the second theorem, any calculation on electron density function, considered as trial will exhibit higher energy or equal to the true ground state minimum energy.

Due to lack of kinetic energy functional approximation, deducing density functional for all terms in Eq. 2.23 are less accurate. This is known as orbital free approach. In order to overcome this problem, Kohn-Sham, KS approach is proposed to DFT. However, KS approach will not be elaborated as this research emphasized on the metal-free organic dye sensitizer design through in-silico.

2.8 Research Aims and Objectives.

In general, aims for this research include selecting ideal density functional to benchmark experimental value and ultimately propose new dye sensitizer for DSSC. Specifically, the objectives of this research are:

- 1) To locate the minimum position of theoretical dye sensitizer in the Potential Energy Surface, PES by optimization and frequency calculation employing Density Functional Theory, DFT methods.
- 2) To compare the most efficient method to benchmark experimental Highest Occupied Molecular Orbital via Vertical Ground State Oxidation Potential, $GSOP_v$, Adiabatic Ground State Oxidation Potential, $GSOP_a$, and Koopman's Theorem theoretical Highest Occupied Molecular Orbital, $HOMO_{cal}$.
- 3) To design metal-free organic dye sensitizer through possibility of substitution on the π -linkage bridge of an existing dye via Dewar's Rule.

CHAPTER 3: RESEARCH METHODOLOGY

3.1 Introduction

Six squaraine dyes (SQM) are taken into account to benchmark the highest occupied molecular orbital (HOMO) using various density functional and be used for rational structural design. Studied dye will be divided into 2 categories, they are symmetrical and unsymmetrical squaraine dyes. As mentioned in previous chapter, symmetrical squaraine dyes comprise SQM1a, VG1 and VG10. Unsymmetrical dyes comprise SQM1b, MSQ, SQ01 and VG13.

At experimental and fabrication stage, DSSC dye is evaluated by conversion efficiency η obtained from equation 2.10. Within the formula, the short-circuit current density, J_{sc} can be increased by extending the absorption region of dye sensitizer. In other words, the desired dye should absorb light at longer wavelength that reside at red spectrum region (Kamlet & Taft, 1976).

A molecule is said to experience bathochromic shift when the absorption of spectral band occurs at longer wavelength (lower frequency). Hence, a bathochromic shift is needed as part of desired dye property. UV-VIS spectrum for every investigated dye are made available. The absorption range and spectral bandwidth are taken into account for comparison with theoretical values.

At theoretical stage, bathochromic shift is achieved by lowering the HOMO-LUMO gap (Adachi & Nakamura, 1994). Molecules are distinguished by geometrical shape, type and position of atoms. Molecular geometry or structure is defined as set of three dimensional coordinates with x, y and z coordinates. Hence, properties of a compound can be obtained from the derivation of molecular structure function (Charton, 2002; Katritzky et al., 2010; Seybold et al., 1987).

3.2 Ground State Calculation

All calculations at ground state are carried out using DFT. The structure is fully optimized in order to locate the lowest energy on the PES. Frequency calculation is included to verify that the minima obtained does not reside on transition state. Default integration grid in Gaussian 09W package is used.

For SQM1a, SQM1b and MSQ, (Maeda et al., 2013), optimization in both vacuum and chloroform are employed. The following keyword to optimize dye in vacuum is inserted into calculation route since the three dyes are synthesised with the same environment:

```
opt freq b3lyp/6-31g(d) geom=connectivity formcheck
0 1
molecule specification (3.0)
```

The opt freq keyword are the keyword for optimization and frequency calculation is employed. Optimization is calculated before single point energy calculation for frequency assessment.

The next keyword is for density functional input. In keyword above, b3lyp density functional is used. 5 other density funtionals are employed to determine the true minimum of compound being studied. Hence, b3lyp keyword is replaced by either pw91pw91, pbepbe, mpw1pw91, m062x and wb97xd which stands for pw91, pbe0, mpw1k, m062X and ω B97XD respectively.

The charge is set to 0 denoting that a neutral molecule is calculated and spin = 1 for ground state calculation. Molecule structure are expressed as cartesian coordinates and inserted into the molecule specification route.

The formcheck keyword is specified so that the checkpoint file can be opened. All calculation details including molecular orbital are written in *.chk* file. Since calculations are done on a supercomputer which operates in UNIX, specifying formcheck in the calculation route converts checkpoint file into formatted file that can be read and suitable for data visualization in other operating system such as windows, linux or Macintosh.

Most compound that exist as solid are analysed using X-ray crystallography. Hence, true molecular structure at minimum is done in vacuum. Calculation to obtain structure at ground state is done in vacuum. However, when dealing with DSSC system, inclusion of solvation effect is essential.

Molecular properties calculation that deals with ground state and excited states are done in solvent dielectric constant since their experimental measurement utilize solvent. For instance, calculation of experimental HOMO is obtained using cyclic voltammetry measured in the presence of solvent. Also, measurement of experimental LUMO using UV-Vis Spectrometry takes place in solvent environment.

Since SQM1a, SQM1b and MSQ are measured in chloroform, the following keyword to optimize dye in chloroform is inserted into calculation route since the three dyes are synthesised with the same environment:

```
opt freq b3lyp/6-31g(d) geom=connectivity formcheck scrf=(cpcm,solvent=chloroform)
```

0 1

molecule specification (3.1)

Additional keyword is specified in the calculation route, that is the “scrf=(cpcm,solvent=chloroform)”. The keyword SCRF is the abbreviation for Self-Consistent Reaction Field. When SCRF is specified, Gaussian will treat the compound to be studied in a solvent model.

Onsager is the first person to proposed the application of SCRF (Kirkwood, 1934). Based on this model, the compound to be analysed or solute molecule is treated as dipole while the cavity around is a sphere.

In ideal situation, solvation effect should derive from the calculation of explicit inclusion of solvent particles. Unfortunately, this method is too expensive in terms of computational demanding task and time.

In response, solvent effect is obtained by derivation of implicit solvation methods that treat solute in a cavity of solvent reaction field. Thus, the surface of the cavity is treated with solvent that act as a structure-less particle that possessed dielectric medium having specific dielectric constant, depending on the type of solvent used (Tomasi et al., 2005).

Simulation of such approach is called continuum solvation approximation. There are three continuum solvation model and they are the Polarizable Continuum Model, (PCM) Conductor-like Polarizable Continuum Model, (C-PCM) and Solvation Model Based on Desntiy, (SMD). In this research, simulation for molecular properties are obtained by employing C-PCM.

Solvent used for other compounds like VG1, SQ01, VG10 and VG13 are done in n,n-di-Methyl Formamide. Since methyl formamide is not listed in the option given, the dielectric constant for this solvent is manually inserted. The following keywords are inserted into the calculation route for VG1, SQ01, VG10 and VG13 optimization:

```
opt freq b3lyp/6-31g(d) geom=connectivity formcheck scrf=(cpcm,solvent= generic,read)
0 1
molecule specification (3.2)
```

B3LYP as the manipulated variable and will be changed for other density functionals. The dielectric constant and solvent details are inserted at the bottom part of the input file:

```
stoichiometry=C3H7N1O1
solventname=n,n-DiMethylFormamide
eps=37.219
epsinf=2.04633025 (3.3)
```

Based on equation 3.3, the EPS specify the zero-frequency or the specific static of the dielectric constant for a given solvent. EPSINF keyword specify the optical or dynamic dielectric constant of a given solvent. The EPS and EPSINF can be obtained from the refractive index of a solvent and derivation of Maxwell's equation.

3.3 Ground state oxidation potential

Employing DFT level calculation, theoretical HOMO energy is closer to experimental values when calculation is proceeded via ground state oxidation potential (GSOP) (Pastore & Angelis, 2013). Therefore, value obtained from GSOP calculation may provide better description on HOMO energy level for a dye sensitizer. GSOP is defined as the difference in free energy between neutral and oxidized species. GSOP calculation involve the Gibbs free energy of a species in vacuum and the solvation free energy.

This technique is rather cumbersome and expensive since DSSC system involve large molecules. An alternative method to acquire GSOP can be done by calculating the vertical

energy difference, $GSOP_v$ comprise the dielectric constant between neutral and oxidized species. Both calculations are done in ground state geometry, employing DFT calculation.

Another assumption is to calculate the adiabatic energy difference, $GSOP_a$ between neutral and oxidized species in solution. The third assumption is based on Koopman's theorem, $HOMO_{cal}$ which assume the negative orbital energy of HOMO as the first ionization energy for a chemical species.

For this section, calculation of $GSOP_v$, $GSOP_a$ and HOMO are done to benchmark experiment HOMO energy value. All GSOP calculation are done by DFT employing 6 different density functionals. Little emphasize is put on basis set thus, it is kept constant since all investigated dye belong to Squarine group. Instead, energy changes will be based on the variety of HF exchange term in a density functional.

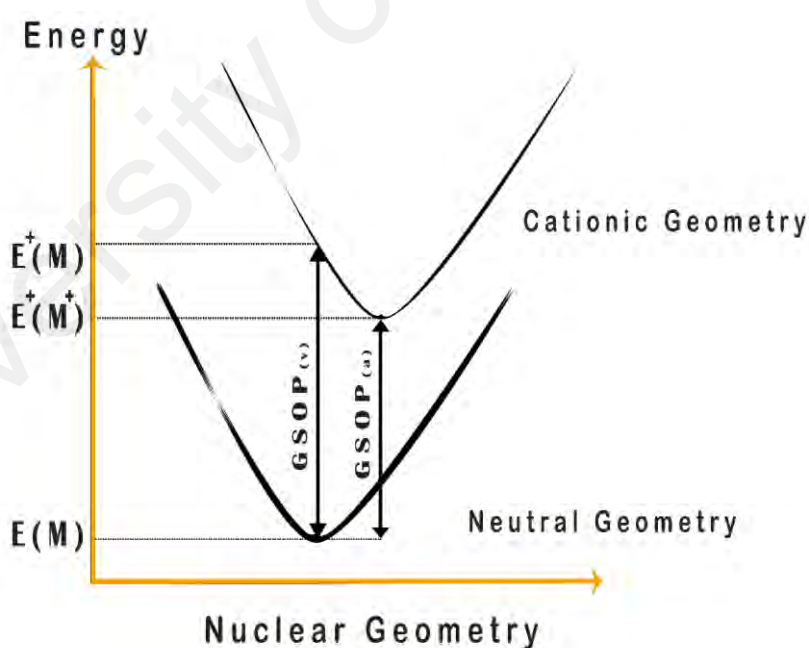


Figure 3.1: Representation of the Potential Energy Curves Used in Determining $GSOP_v$ and $GSOP_a$.

From this study, theoretical values which is obtained via GSOP_v, GSOP_a, and HOMO are compared with experimental value. Based on figure3.1, GSOP_v and GSOP_a are obtained by:

$$\text{GSOP}_v = E(M) - E^+(M) \quad (3.4)$$

$$\text{GSOP}_a = E(M) - E^+(M^+) \quad (3.5)$$

Where the neutral molecule ground state energy is denoted as $E(M)$, the neutral molecule cationic energy is denoted as $E^+(M)$, and the ground state cationic energy of the cationic molecule is denoted as $E^+(M^+)$.

Therefore, GSOP_v is obtained by the difference between $E^+(M)$ with $E(M)$ as stated in equation 3.2. GSOP_a is obtained by subtracting $E(M)$ with $E^+(M^+)$. The ground-state energy of the neutral molecule, $E(M)$ is obtained through optimization similar to equation 3.1.

Inclusion of C-PCM is necessary in order to include solvent dielectric constant, thus similar environment as experimental measurement is ensured. Once the desired molecule has been optimized, single point calculation is performed on the ground state molecule, M. To perform single point calculation onto the optimized M, the following keywords are inserted into calculation route:

```
b3lyp/6-31g(d) scrf=(cpcm,solvent=chloroform) geom=connectivity formcheck
```

```
1 2
```

```
molecule specification (3.6)
```

where the charge is set to one while the spin for a cationic species is 2. $E^+(M^+)$ is obtained by optimizing the cationic molecule obtained from equation 3.4. Thus, the keyword specified for ground-state energy of the cationic structure is as follow:

```

opt freq b3lyp/6-31g(d) scrf=(cpcm,solvent=chloroform) geom=connectivity formcheck
1 2
molecule specification

```

(3.7)

where the charge is set to one while the spin for a cationic species is 2.

3.4 Excited State Calculation

Excited state oxidation potential (ESOP) is obtained by the inclusion of first excitation energy obtained from GSOP. This translate to LUMO of the studied molecule. However, to arrive at ESOP, the excited dye must be optimized. Unfortunately, convergence for excited state optimization has failed. One explanation for these phenomena is due to the broad excitation energy.

Therefore, any attempt to optimize structure at excited state will fail since the energy are similar with the initial attempt and no lower energy can be found on the PES of an excited state energy.

LUMO is obtained via Koopman's theorem and Time- Dependent Density Functional Theory is employed. The following keyword is inserted into the calculation route:

```

td=(nstates=40, root = 1) b3lyp/6-31+g(d)
scrf=(cpcm,solvent=chloroform) geom=connectivity formcheck pop=full
0 1
molecule specification

```

(3.8)

This is simply translated to as calculating geometry to be studied in 40 excited states level using B3LYP as the density functional of choice with 20% HF E_{xc} term and basis set of 6-31G, incorporating together polarization function d and p on heavy atoms and hydrogen atom respectively.

Root = 1 means that first excited state gradient is to be optimized. In other word, the first excited state minimum is calculated. Root = 2 simply means calculation to find the second excited state minimum.

The CPCM model is specified since UV-Vis is sensitive towards solvent used in the experimental measurement. In order to maintain the same environment in experiment, CPCM is included. The solvent keyword is changed to suit molecule to be studied.

To provide a baseline for benchmarking oxidation potential, Squarine based dye at excited states are analyzed. Many options are available in performing excited state calculation using Gaussian 09 namely, time-dependent density functional theory (TD-DFT), configuration interaction singles (CIS) or complete active space self-consistent field (CASSCF).

Due to the large size and complexity of the studied molecule, CIS and CASSCF calculation are computationally expensive. Many studies have followed an approximate method in acquiring low-lying excited states via Koopmans theorem. This is because the difference between orbital energies, $\epsilon_\alpha - \epsilon_i$ exhibit excitation energy for an independent electron. Thus, transitions between HOMO to LUMO involves the lowest excited states.

Such approximation is rather crude as the hole-electron attraction (also known as electron-electron interaction) and orbital relaxation are neglected. In consequence to that: (i) an in finite systems such as molecules tends to predict excitation energies that are too high; (ii) same excitation energies are predicted for singlet and triplet states.

Apart from that, valence character is retained in the lowest excited state when diffuse orbitals are loaded onto the valence HOMO-LUMO cavity in diffuse bases. Another caveat following Koopmans theorem is seen from previous discussion at describing GSOP level.

Since Koopmans theorem unable to accurately determine the starting point of energy level at optimized geometry, exciting an electron will exhibit inaccurate excited state property. Excited state calculation is proceeded by following either excited state oxidation potential (ESOP) method or single-point calculation using TD-DFT on optimized geometry.

Geometry optimization at excited state is required for ESOP calculation. Calculation proceeded via ESOP for squarine based dye failed to converge. One of the reason would be the large character change between the Franck-Condon geometry and the excited state minima (Fong, 1976; Richards et al., 1963).

The two states are said to be close in energy and constantly flipped from one another during optimization, unable to converge. Output files are examined and it has been confirmed that the two states are constantly switched during optimization with small changes in energies within the last steps.

Number of states have been increased by changing the job keyword section, `nstates=3` is replaced with 6 (`nstates = 6`) and 20 (`nstates = 20`). Convergence point at excited state still failed to be detected. 2 years of research is spent to locate the minima of the excited state.

One way is to include multi-reference method such as state averaging- complete active space self-consistent field (SA-CASSCF) to find minima of the desired state (Luis et al., 2004). However, this method is in practical as the investigated system comprise large number of atoms and the complexity of electron interactions.

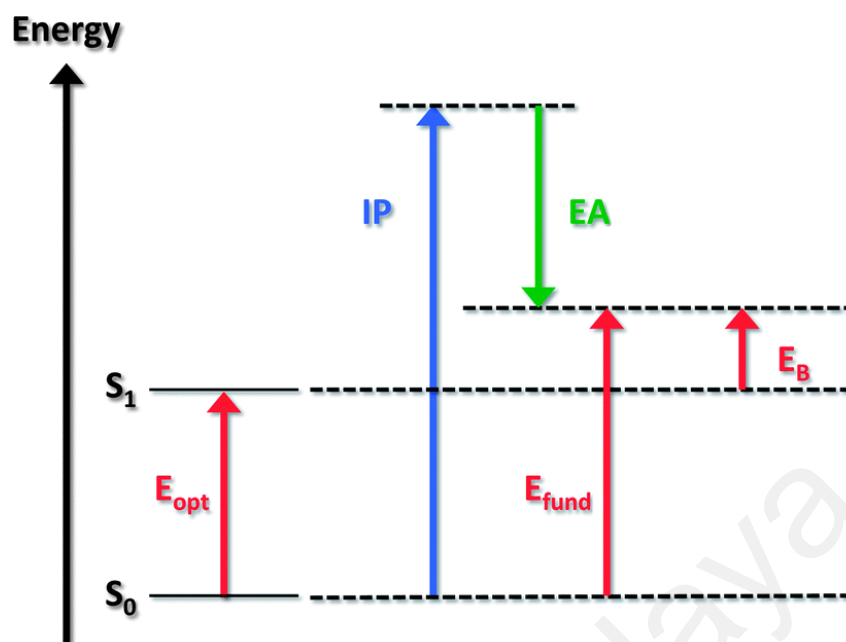


Figure 3.2: Gap Energies in Molecular Ground State and Excited State.

Illustration on gap energies in the molecular case is shown in diagram above: S_0 denotes the (singlet) electronic ground state and S_1 the lowest (singlet) excited state (considered here to be accessible via one-photon absorption).

The $S_1 - S_0$ energy difference then corresponds to the optical gap E_{opt} . The magnitude of the ionization potential is given by the blue vertical line and the magnitude of the electron affinity by the green vertical line; the $IP - EA$ difference represents the fundamental gap, E_{fund} . The electron-hole pair binding energy, E_B , is given by $E_{fund} - E_{opt}$.

Therefore, theoretical modelling to benchmark squaraine based dye LUMO level will not be covered in this research. Instead, single point calculation at excited state is performed on the optimized ground state geometry. In other word, squaraine based band gaps are analyzed.

3.5 Dewar's Rule

Electron distribution is expected to have a unidirectional flow from the donor group to the anchoring group before it is injected into TiO₂ nanocluster. Rational structural designed will involve a number of electron-donating (ED) and electron-withdrawing (EW) units based on Dewar's rules. Substitution will be done on the π -conjugated bridge, thus, obtaining different level of HOMO and LUMO energy.

Using Gaussian 09W, the molecular geometry, frontier molecular orbital energy level will be altered and computed by DFT. The effects of these alternations on the molecular structures and the electron absorption spectra are continued at the excited states by employing TD-DFT and compared with UV-Vis absorption spectra of the experimental data. The designed indolenine group is expected to provide a good electron distribution to TiO₂ nanocluster. Thus, the optical band gap can be lowered as part of the rational designed of the desired dye.

Structural design follows perturbational molecular orbital theory in which starred and unstarred part of the π -conjugated chain is labelled. Electron donating group substitution on starred position will result in increase of HOMO energy while substitution of electron withdrawing group on unstarred position will decrease LUMO energy. Therefore, the band gap will be reduced giving a bathchromic shift (red shift) in the UV-Vis spectrum and an increase in short-circuit current density, J_{sc} .

Organic sensitizer in DSSC can be divided into three section. Firstly, the acceptor moiety act as the binding site that anchor onto TiO₂ nanocluster. Second section is marked in the figure 3.3 as conjugated π -bridge denoted as π -B. The third part dictates majorly the optical property of a dye sensitizer, the electron rich donor group (D).

SQM1a is said to adopt a $D-\pi-A$ configuration since it comprises donor, π -conjugated bridge and acceptor group. This is a common configuration for an organic dye sensitizer. The two butyl groups are used to suppress π -stack aggregation between the donor group and TiO_2 nanocluster.

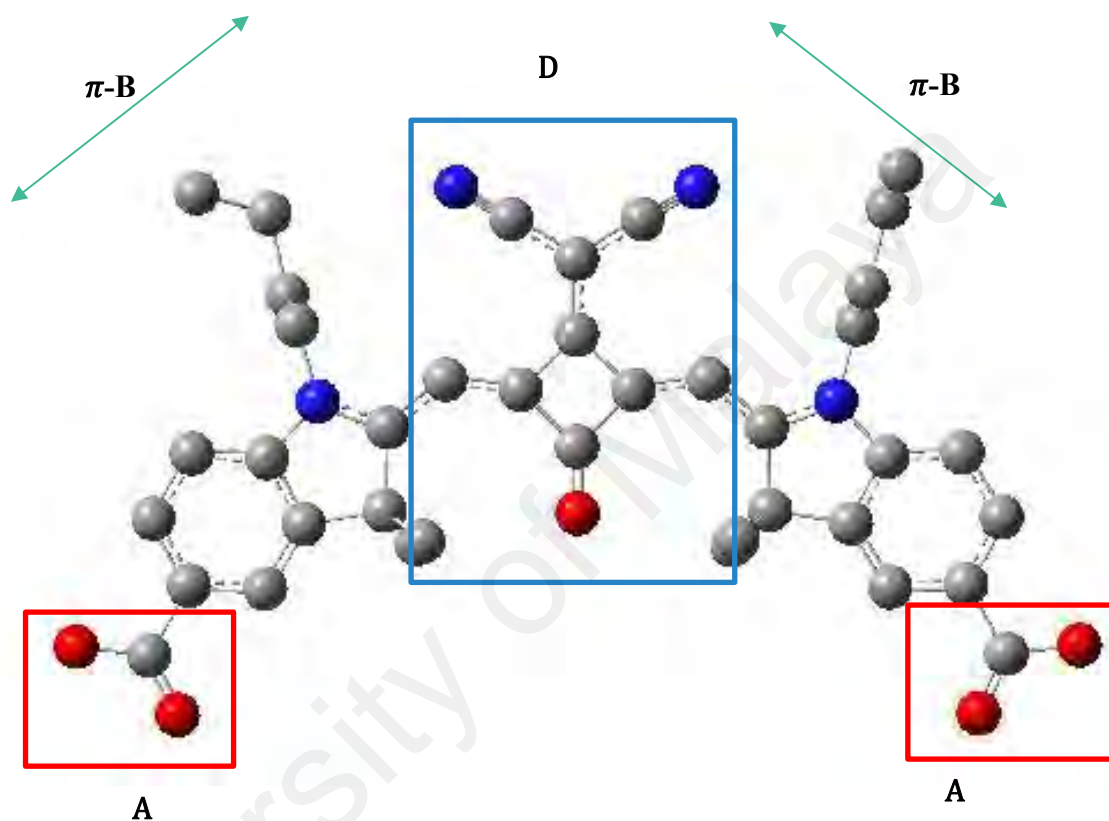


Figure 3.3: Optimized 3D Structure of SQM1a Dye Sensitizer (Red: Oxygen; Blue: Nitrogen; Grey: Carbon). Hydrogen Atoms Are Not Displayed to Aid Visualization.

Intermolecular quenching is a phenomenon where the excited electron from the donor group is injected into adjacent dye instead of TiO_2 nanocluster. Also, dye sensitizers are not able to bind well with TiO_2 when aggregation occurred. Thus, the two butyl groups aid in shaping the dye sensitizer into a non-coplanar structure while $D-\pi-A$ configuration planarity be maintained.

Thermal stability can be enhanced by retaining the non-coplanar structure by reducing the contact between D-group. For long term functional stability, thermal stability is an important factor to be considered in DSSC rational design. The nitrogen attached in

pentagon ring forms the pinnacle of the π -bridge. More stable organic dye can be achieved in high polarity electrolytes when this type of chromophore is employed.

A squaraine dye is able to isomerise between trans/cis like conformer. However, SQM1a is locked via steric effect in cis-like conformer by the core substitution in D-group. This is to prevent photoisomerization that could decrease the quantum yield of a dye sensitizer.

Photoisomerization is an effect of conformational change during excitation. Hence, quantum yield decreases as a result of conformational change instead of electron excitation. As mentioned in previous chapter, *D- π -A* configuration can be altered based on Dewar's rule in order to maximise solar absorption in the long wavelength region and ultimately increase the J_{sc} of an organic dye sensitizer.

There are many studies that account for structural modification on donor and acceptor group. For this study, designing an organic dye sensitizer that is able to shift absorption to long wavelength is desired. This is done by decreasing HOMO-LUMO through modification on the π -bridge. Structural modification using Dewar's Rule as a guideline, the π -bridge SQM1a is connected with either an electron donating group (ED) or electron withdrawing group (EW).

As mentioned in previous chapter, substituting ED onto a starred π -bridge linkage results in increasing in HOMO energy. Alternatively, EW substitution along π -bridge linkage at unstarred position decreases LUMO energy. Since SQM1a has alternate double bonded carbon, starred and unstarred position of SQM1a can be determined based on Coulson-Rushbrooke Longuet-Higgins theorem (Coulson & Rushbrooke, 1940).

According to Coulson-Rushbrooke Longuet-Higgins theorem, for alternate hydrocarbon with N conjugated atom, here identified as carbon, has at least $N-2D$ number of non-bonding molecular orbital (NBMO) where D is the maximum number of conjugated

bond (double or triple bonds) experienced in resonance structure. Therefore, SQM1a can be represented as in figure 3.4 where starred position is labelled as asterisk, * while unstarred position is not labelled, instead alternate with starred position within π -bridge linkage.

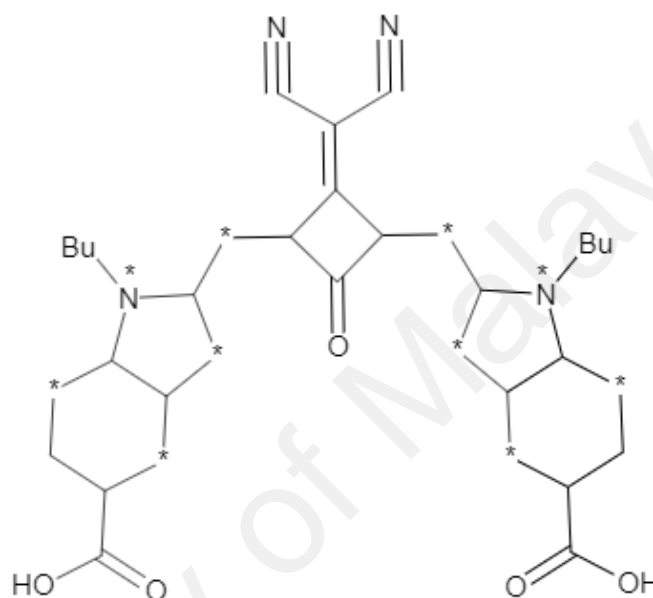


Figure 3.4: Schematic Diagram for SQM1a with Starred and Unstarred Labelled Position. Take Note That Starred Position is Put Asterisk and Unstarred Position is Left Empty, Alternating Starred Position.

Figure 3.5 below illustrates the work flow of the entire methods, starting from geometry optimization to benchmarking GSOPs. All works are done in-situ and dyes are taken from experimental work with permission from authors. Experimental values for all dyes are taken into account to benchmark experimental and theoretical band gap. SQM1a, SQM1b, and MSQ are taken from the work of Maeda et. al. (Maeda et. al., 2013). SQ01 and VG1 dyes are taken from Barolo et. al., 2012 while VG10 and VG13 are taken from the work of Barbero (Barolo et. al., 2012; Barbero et. al., 2014)

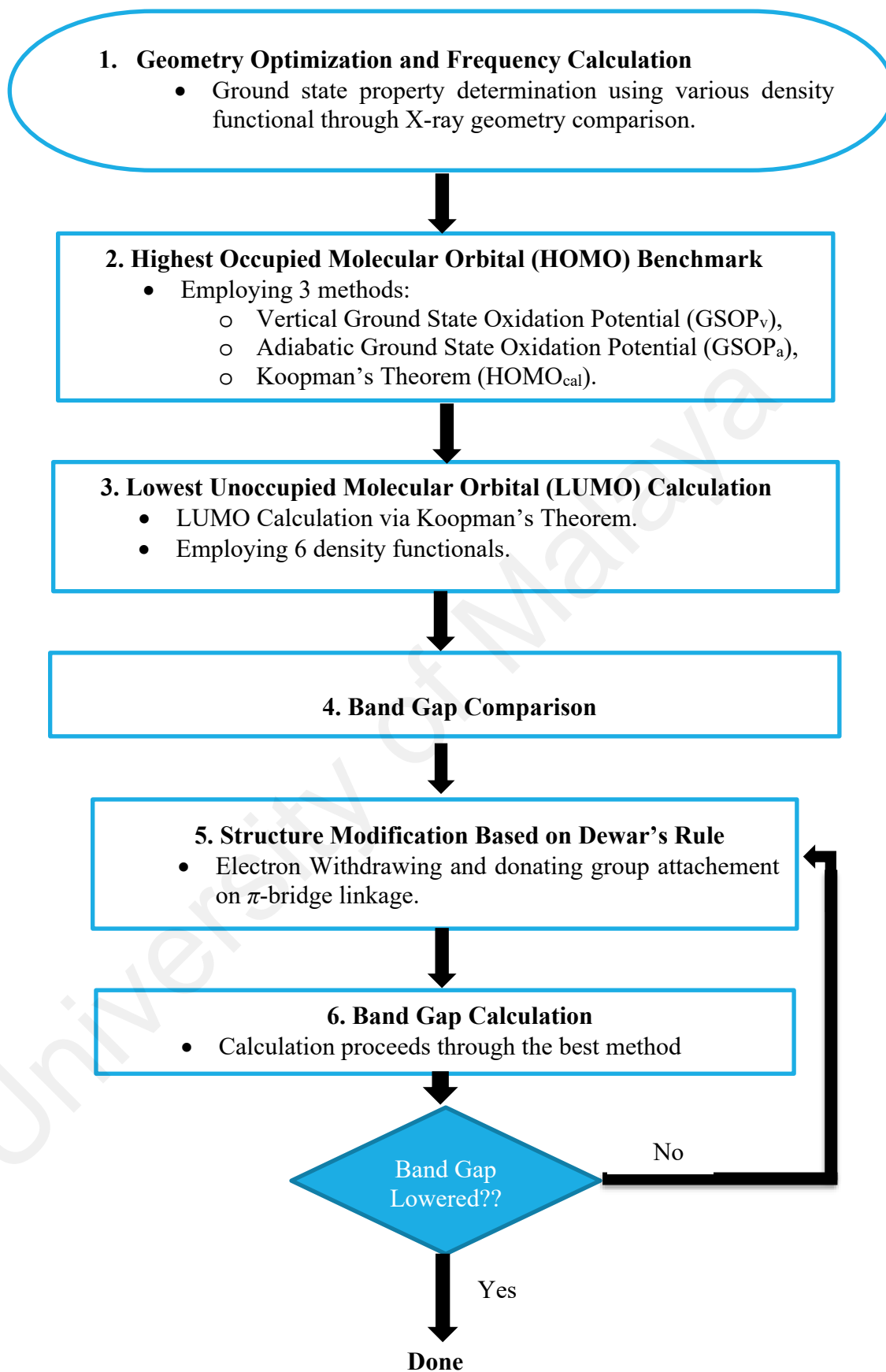


Figure 3.5 Research Process Flow Chart.

CHAPTER 4: RESULT AND DISCUSSION

4.1 Ground State Determination

4.1.1 Conformation Study

Since SQM1a is the only dye published with X-ray data, comparison of geometrical parameters (bond length, angles and dihedral angle) related to the X-ray data with the theoretical data for SQM1a are listed in table 4.1 (Maeda et al., 2013). Experimental X-ray is used to determine the choice of XC functional based on the bond length, bond angle and dihedral angles. These are crucial parameters at describing the behaviour of molecules thus, locating the correct position of ground state on the potential energy surface. From this point onward, all experimental data will be based on the work of Maeda et. al., since they have given permission and they are the only group that publish X-ray structure.

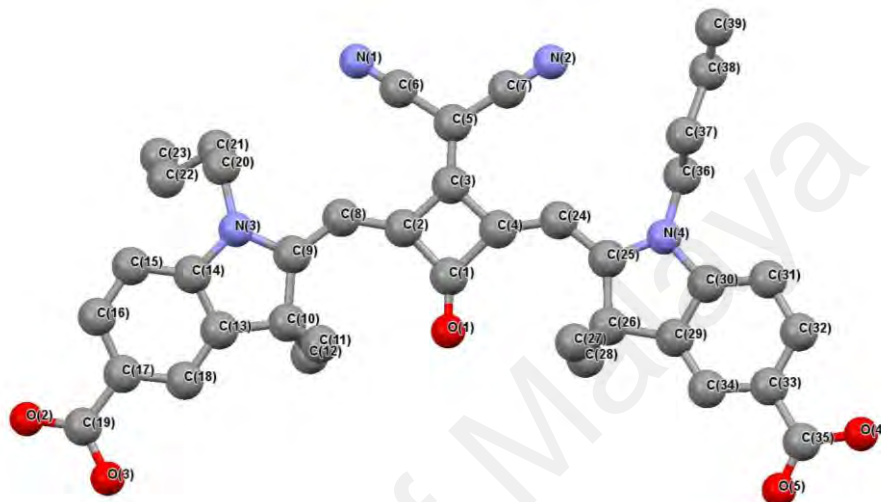
As can be seen, the bond length obtained for B3LYP and PBE0 is promising. The least absolute error in terms of bond length is obtained from B3LYP. PBE0 showed second best density functional to match experimental data. All angles including dihedral angles obtained theoretically exhibit almost similar value and differ with experimental data. This is because, optimization in Gaussian is done in vacuum or solvent where the molecule is calculated in isolation. Thus, no neighboring molecule is inserted during calculation. Thus, a saddle shape is formed to counter every steric hindrance and arriving at the lowest part of the PES.

On the contrary, molecule obtained via X-ray crystallography exhibit planar shape as the molecules are stacked in an orderly arrangement. It is impossible to isolate molecule and calculate the true minimum experimentally. Nevertheless, the bond length and angle provide information on the properties of the molecules to be studied since molecular geometry is associated with the energy in the PES. Density functional with large HF

exchange term provide the worst description on the experimental bond length and angles.

These include MPW1k, M062X and ω B97XD.

Table 4.1: Bond Distances (Å) and Angles (°) for Compound SQM1a, Calculated at DFT Level Using Various Functional/ 6-31G (d). (Experimental X-ray values are taken with permission of Maeda et. al., in Journal of Material Chemistry, 2013).



	Experiment	PW91	B3LYP	PBE0	MPW1K	ω B97XD	M062X
Bond length(Å)							
C ₁ – O ₁	1.215	1.224	1.217	1.218	1.224	1.380	1.222
C ₁ – C ₂	1.472	1.480	1.475	1.477	1.478	1.382	1.482
C ₂ – C ₃	1.430	1.447	1.433	1.436	1.447	1.392	1.443
C ₃ – C ₄	1.444	1.446	1.446	1.446	1.447	1.412	1.443
C ₃ – C ₅	1.380	1.391	1.385	1.382	1.391	1.454	1.390
C ₂ – C ₈	1.397	1.395	1.396	1.395	1.400	1.422	1.396
C ₈ – C ₉	1.370	1.386	1.380	1.387	1.386	1.218	1.385
C ₉ – N ₃	1.370	1.366	1.374	1.365	1.366	1.353	1.361
N ₃ – C ₁₄	1.397	1.395	1.402	1.394	1.395	1.353	1.400
C ₄ – C ₂₄	1.364	1.395	1.360	1.375	1.395	1.353	1.397
C ₂₄ – C ₂₅	1.384	1.386	1.390	1.386	1.386	1.353	1.384
C ₂₅ – N ₄	1.346	1.366	1.344	1.345	1.366	1.353	1.362
N ₄ – C ₃₀	1.423	1.395	1.402	1.394	1.395	1.353	1.399
Bond Angle(°)							
C ₂ – C ₈ – C ₉	133.7	132.9	133.1	132.9	132.9	118.0	132.2
C ₈ – C ₉ – N ₃	119.7	120.1	120.1	120.0	120.1	118.7	120.1
C ₉ – N ₃ – C ₁₄	110.8	111.5	111.5	111.5	111.5	111.5	111.5
C ₄ – C ₂₄ – C ₂₅	133.0	132.9	133.1	132.8	133.0	130.9	132.0
C ₂₄ – C ₂₅ – N ₄	120.1	120.1	120.1	120.0	120.1	130.9	120.2
C ₂₅ – N ₄ – C ₃₀	110.6	111.5	111.5	111.5	111.5	130.9	111.5
Dihedral Angle ^a (°)							
C ₂ – C ₈ – C ₉ – N ₃	-	178.4	178.4	178.3	178.4	178.2	178.3
C ₈ – C ₉ – N ₃ – C ₁₄	-	178.1	178.3	177.8	178.1	177.1	176.2
C ₄ – C ₂₄ – C ₂₅ – N ₄	-	178.1	178.1	178.0	178.1	177.1	179.3
C ₂₄ – C ₂₅ – N ₄ – C ₃₀	-	177.5	177.7	177.2	177.5	176.8	174.9

4.2 Ground State Oxidation Potential (GSOP)

4.2.1 GSOP Obtained from Energy Difference

We have compared below three methodologies employed to benchmark dye oxidation potentials. GSOP is obtained from calculation of an approximation energy difference in solution between neutral and oxidized species. As explained in Chapter 3, $GSOP_v$ and $GSOP_a$ are taken into account to estimate the total energy from the changes of nuclear position as a result of electron removal. On the other hand, $HOMO_{cal}$ is obtained from inclusion of negative sign onto oxidation potential obtained from Koopman's Theorem.

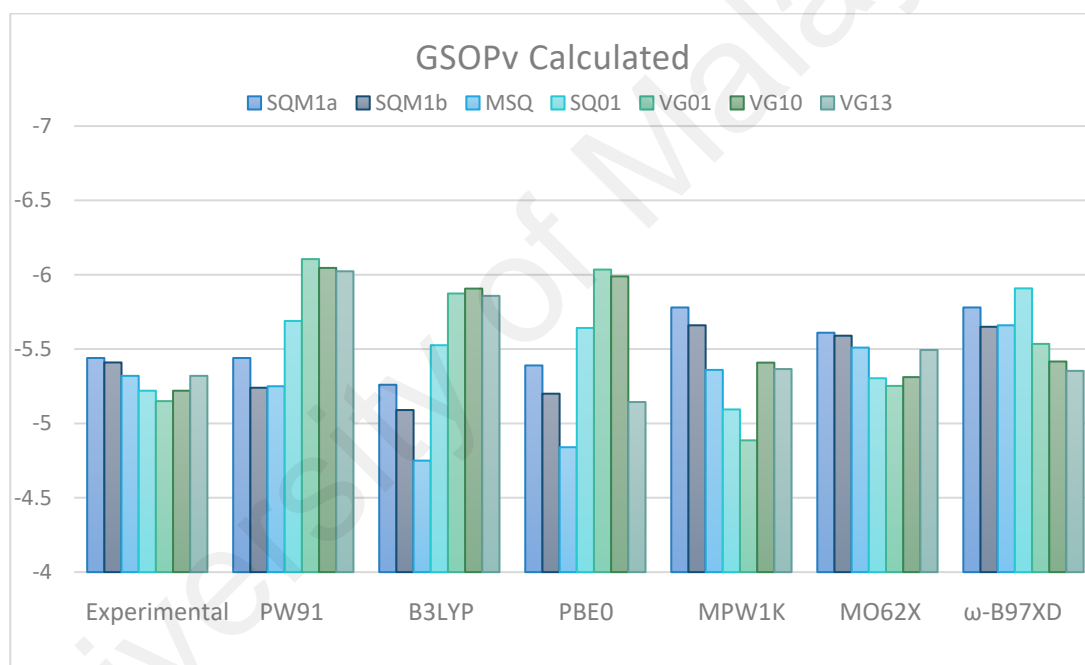


Figure 4.1: $GSOP_v$ versus the calculated $GSOP_v$ using various density functionals in DCM employing the C-PCM framework.

A benchmark evaluation of $GSOP_v$ on different percentage of exchange and correlation functional against experimental squaraine dyes are summarized in Figure 4.1. Reliable results are obtained only for dicyanovinylene squaraine (SQM1a and SQM1b) dyes calculation when pure density functional, PW91 is employed. PW91 functional overshoot oxidation potential for squarylium (MSQ), trimethyl-indolenine squaraine (VG1 and SQ01) and bis-benzoindolenine squaraine (VG10 and VG13) dyes.

The above trend can also be seen for DFT hybrids with relatively moderate percentage of HF E_{xc} term (20-25%). B3LYP and PBE0 comprise 20% and 25% HF E_{xc} term surpassed squarylium, trimethyl indolenine and bis-benzoindolenine squarine experimental value. Well ground results are obtained only for dicyanovinylene squarine dyes calculation. Calculation involving large HF E_{xc} term such as MPW1k, M062X and ω B97XD deliver oxidation potential which compare well with all dyes.

This can be explained through conformational effect in squarine dyes. GSOP_v involved removing one electron to bring about energy changes in nuclear position. Elongation of π -conjugation system in the usage of C-C double bond, known as photoisomerizable bonds affect overall conformation and electrochemical properties of a compound (Ince, 2012). A cis-like conformation is possible over trans-conformer since squarine dyes are obtained from the condensation between heterocyclic group such as 2,3,3-trimethyl-3H-indolenine moiety and squaric acid (Ohira et al., 2008; Pandey et al., 2010; Yan et al., 2012).

The thermodynamically stable trans-conformer can be photoisomerized to cis-conformer upon electron removal. A photophysical process studied by Tatikolov where by long chain π -conjugation system experience cis to tran-like conformer via twisted intramolecular charge transfer state, TICT (Tatikolov & Costa, 2001). No excited state is required since dye sensitizer experience charge transfer via GSOP_v that brought energy changes thru ionization or removal of electron. TICT is induced by solvent polarity that affect dye sensitizer dipole moment.

Once induced, an increased in dipole moment on dye sensitizer (solute) resulted in intramolecular charge transfer that involve solute relaxation via twisting on photoisomerizable bond (Gude & Rettig, 2000; Tatikolov & Costa, 2001).

Hence, all squaraine dyes except for dicyanovinylene squaraine (SQM1a and SQM1b) experience TICT. The unique feature that dicyanovinylene squaraine possessed is the presence of bulky electron withdrawing group on the centre cyclobutene core and a relatively optimum alkyl chain length (Mayerhöffer et al., 2009; Tatarets et al., 2005; Völker et al., 2011).

A cis-like conformer is locked when bulky electron withdrawing group is substituted into cyclobutene core. Hence, photoisomerization is suppressed by bulky core substitution owing to steric effect. In other word, the conformer is locked when one electron is removed (Maeda et al., 2013).

From structural effect point of view, steric effect is also exhibited on indolenine moiety. Other dyes being investigated have alkyl chain of 7-8 on the indolenine moiety except for dicyanovinylene squaraine and squarylium dye. Both of these dyes are sensitized to have butyl as the substituent on the indolenine moiety. A saddle shape geometry is obtained when all dyes are optimized. A slight planar shape is exhibited for dyes with small amount of alkyl chain on the indolenine moiety. Hence, a good delocalization of π -electron is obtained for dicyanovinylene squaraine and squarylium dyes.

Although squarylium dye has a slight planar shape, photoisomerization is contributed by the presence of small oxygen on cyclobutene core. Therefore, a less accurate result is obtained for DFT with small HF E_{xc} term. Oxidation potential accuracy is not affected when large fraction of HF E_{xc} term is used via GSOP_v. Based on Figure 4.1, reliable oxidation potential is obtained over the entire set of squaraine dyes from calculation of DFT with large fraction of HF E_{xc} term. In contrast, benchmarking oxidation potential using small HF E_{xc} term against experimental value of a saddle shape geometry would be difficult. Theoretical oxidation potential will either aligned below or above experimental energy line.

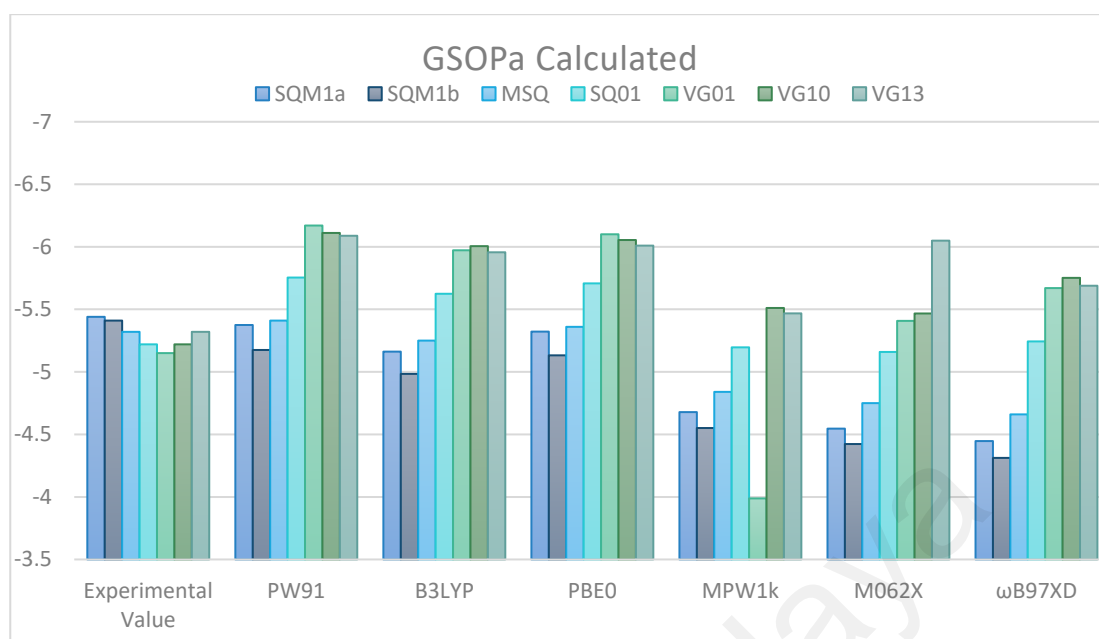
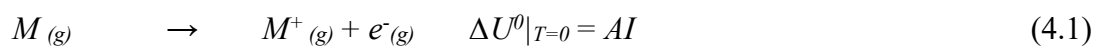
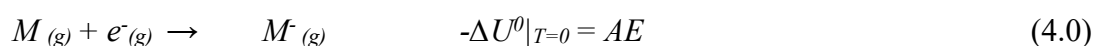


Figure 4.2: GSOP_a versus the calculated GSOP_a using various density functionals in DCM employing the C-PCM framework.

Cation geometry optimization is required to calculate adiabatic energy difference (GSOP_a). Geometry optimization is calculated on oxidized species instead of single point energy calculation in GSOP_v. Therefore, degree of photoisomerization in VG1, SQ01, VG1, VG10 and MSQ would be greater. Based on Figure 4.2, range separated hybrid functionals and global hybrids with large HF E_{xc} term underestimate oxidation potential for VG1, SQ01, VG10 and VG13. On the other hand, the same density functionals overestimate oxidation potential for SQM1a, SQM1b and MSQ.

The above trend can be explained from the GSOP_a equation below. Assuming that adiabatic ionization potential (AI) and adiabatic electron affinity (AE) for a given molecule such as M are calculated. These quantities are defined as follows:



Note that U^0 denotes standard internal energy defined as below:

$$U^0 = E^{elec} + ZPE \quad (4.2)$$

Where $M_{(g)}$ denote neutral molecule in gas phase, $M_{(g)}^-$ is an anionic molecule in gas phase, $e_{(g)}^-$ is an electron in gas phase, E^{elec} and ZPE are the total electronic energies and zero-point vibrational energies respectively. Considering the above definition, optimization followed by frequency calculation is performed for M , M^- and M^+ . Hence, AE and AI can be easily calculated as follow:

$$AE = (E^{elec} + ZPE)_M - (E^{elec} + ZPE)_{M^-} \quad (4.3)$$

$$AI = (E^{elec} + ZPE)_{M^+} - (E^{elec} + ZPE)_M \quad (4.4)$$

In the other words, to calculate an adiabatic quantity, geometry relaxation should be considered after adding and/or removing an electron; i.e. optimization for anion and cation form of M is mandatory indicating that nuclear positions are allowed to be reorganized. The unique, but important, difference between an adiabatic and vertical quantity is that geometry relaxation is not considered when a vertical quantity is calculated; i.e. nuclear positions are not allowed to be changed. In the other words, external potential is kept constant. Vertical ionization potential (IP) and electron affinity (EA) for a given molecule, M , are defined as follows:

$$IP = E^{elec+}_M - E^{elec}_M \quad (4.5)$$

$$EA = E^{elec}_M - E^{elec}_{M^-} \quad (4.6)$$

Hence, geometry optimization is calculated first for neutral molecule, M , in order to obtain the total electronic energy. Next, a single point energy calculation on the neutral optimized geometry in which one electron is added (M^-) yields corresponding total

electronic energy for anion. Similarly, a single point energy calculation on the neutral optimized geometry in which one electron is removed (M^+) yields corresponding total electronic energy for cation.

Severe photoisomerization on push-pull dye sensitizer is exhibited as a result of geometry optimization on cation structure. Since photoisomerization is suppressed for dicyanovinylene squarone (SQM1a and SQM1b), incorporating pure DFT and DFT hybrids with medium HF E_{xc} term extent correlate well with experiment value.

In contrast, dye sensitizer coded MSQ, VG1, SQ01, VG10, and VG13 experience greater degree of photoisomerization. Thus, theoretical oxidation potential obtained using different functionals yield erroneous results as a result of TICT.

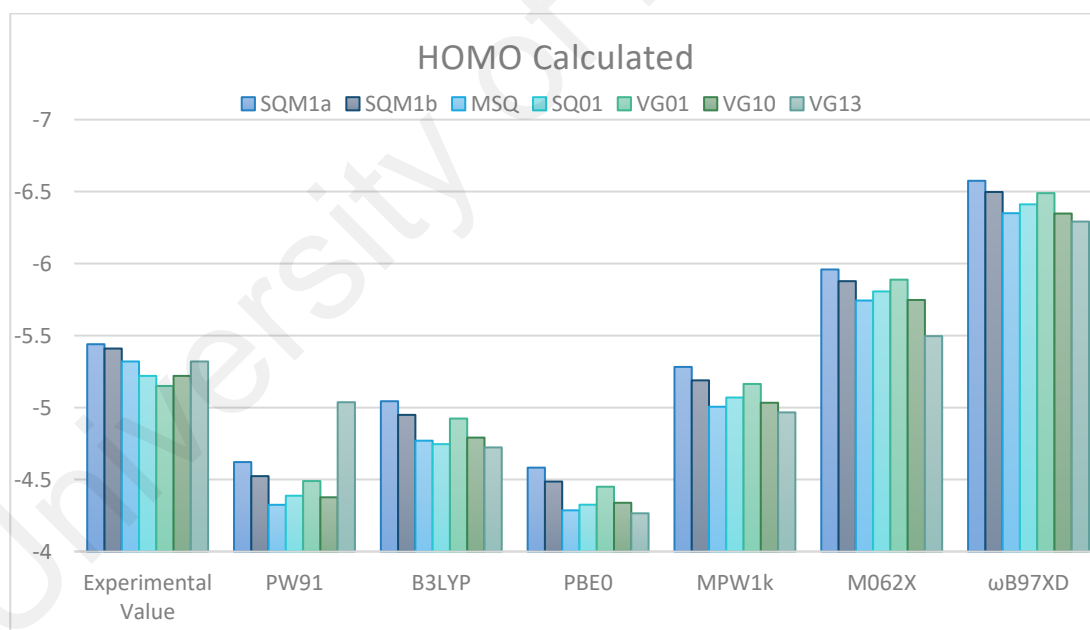


Figure 4.3: $HOMO_{exp}$ versus the calculated $HOMO_{cal}$ based on Koopman's Theorem using various density functionals in DCM employing the C-PCM framework.

The rigorous way to obtain theoretical oxidation is simplified by the minus value of the HOMO energy, $-\varepsilon_{HOMO}$, for a neutral species. Hence, calculation involving cation is avoided and the third methodology employed to benchmark oxidation potential would follow Koopman's Theorem, $HOMO_{cal}$.

In particular, an upper bound to ΔG_{ox} is represented by neglecting structural and orbital relaxation of cation species. Based on Figure 4.3, oxidation potential overestimate/underestimate experimental value. They are obtained from DFT calculation using all of the hybrid/ pure employed HF E_{xc} term. A debate on the physical meaning of the Kohn-Sham orbitals (KS) for the exact Kohn-Sham functional has been raised. The work of Perdew (Perdew et al., 1982) showed that for an atom of nuclear charge Z can be relate to

$$\mu = \begin{cases} -IP & (Z - 1 < N < Z) \\ -EA & (Z < N < Z + 1) \end{cases} \quad (4.7)$$

Where μ is defined as the first derivative of total energy, E against chemical potential, N :

$$\mu = \frac{\delta E}{\delta N} \quad (4.8)$$

In which, chemical potential, N is also the total number of electrons representing a continuous variable, IP as the ionization potential and EA as the electron affinity. The above equation is proven earlier by Janak through which KS orbital energy is denoted as ε_i (Janak, 1978). The mathematical expression for the KS orbital energy is formulated as:

$$\varepsilon_i = \frac{\delta E}{\delta n_i} \quad (4.9)$$

With n_i as the KS orbital ψ_i occupational number and ε_i corresponds to KS orbital energy. Maximum occupied KS orbital energy can be interpreted as

$$\varepsilon_{max} = \begin{cases} -IP & (Z - 1 < N < Z) \\ -EA & (Z < N < Z + 1) \end{cases} \quad (4.10)$$

This proves that within KS density functional, for N-electron system at the highest occupied KS orbital energy is represented by the negative exact ionization potential (Almbladh & von Barth, 1985; Katriel et al., 1980; Perdew et al., 1997; von Barth, 1984). A better definition would be to state that the minus ionization energy term is described as the exact highest-occupied KS eigenvalue (Kleinman, 1997). However, discontinuity derivative on the exact exchange-correlation potential exist at $N = Z$. Due to the $\partial E/\partial N$ discontinuity, at $N = Z$ is calculated as the average value of μ through which,

$$\mu = -\frac{IP+EA}{2} \quad (4.11)$$

Hence, ε_{max} represents one of the KS energy that corresponds to the ground state oxidation potential (HOMO) of the Z-electron system when $Z - 1 < N < Z$. The LUMO can also be obtained through KS orbital energy, ε_{max} for Z+1 electron system. However, discussion of LUMO will be covered in later chapter.

The IP obtained from DFT HOMO energy ($HOMO_{cal}$) is usually too big for small exchange-correlation functionals. This is proven from results obtained in Figure 4.3. Clearly, experimental oxidation potential can be related to KS orbitals by a constant shift in ε -value. Pure DFT comprised pure GGA functionals underestimate experiment value in greater extent. This is due to the result of occupied Molecular Orbital, MOs energy level experienced an up-shift when the non-local Hartree-Fock exchange is induced (Zhan et al., 2003).

On the other hand, small oxidation potential is exhibited from calculation involving big exchange-correlation functional. A good experimental oxidation potential is put on view for DFT calculation using MPW1k. Experiment value is slightly overestimated for density functional that comprise 0.42 gradient generalized approximation mixing fraction. A down-shift on MOs energy level is experienced as the non-local HF E_{xc} is induced (Abbotto et al., 2008).

The corresponding absolute error for squarine derivative calculation using different density functionals are taken into account for oxidation potential assessment. Considering all functionals employed, the mean absolute error (MAEs) for each $GSOP_v$, $GSOP_a$ and $HOMO_{cal}$ are -0.21, -0.28 and 0.68 eV respectively. Hence, the least erroneous error is obtained by calculation of $GSOP_v$ using different functionals. In particular, based on Figure 4.4, calculation of $GSOP_v$ employing M062X functional exhibited the smallest absolute error.

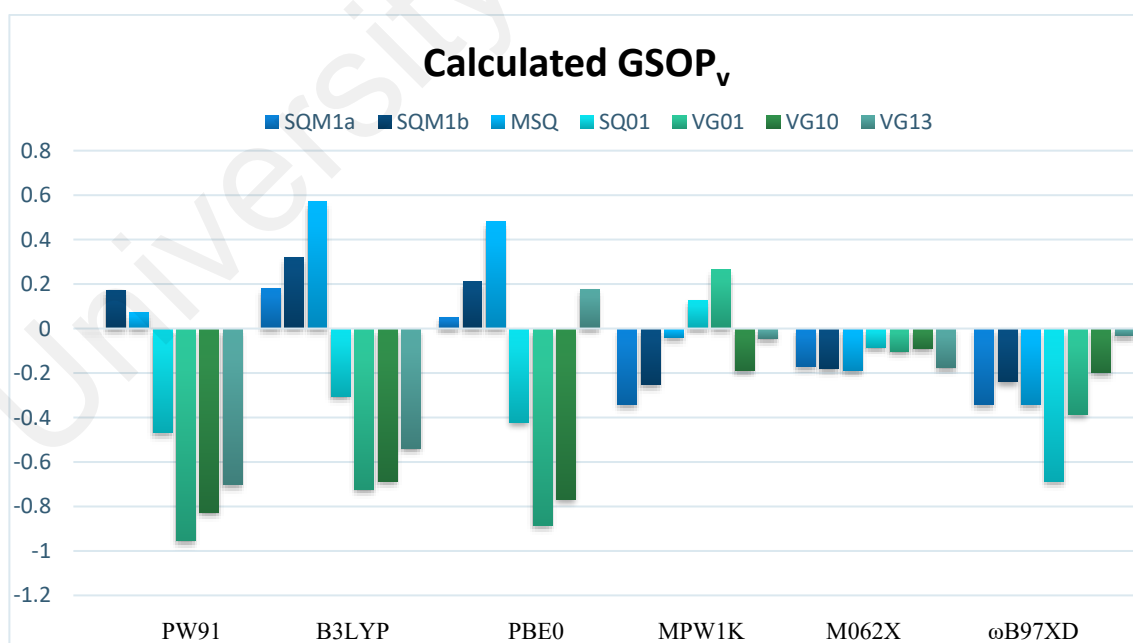


Figure 4.4: Absolute errors for the calculated Squarine Dyes via $GSOP_v$ using different functionals based on the C-PCM framework.

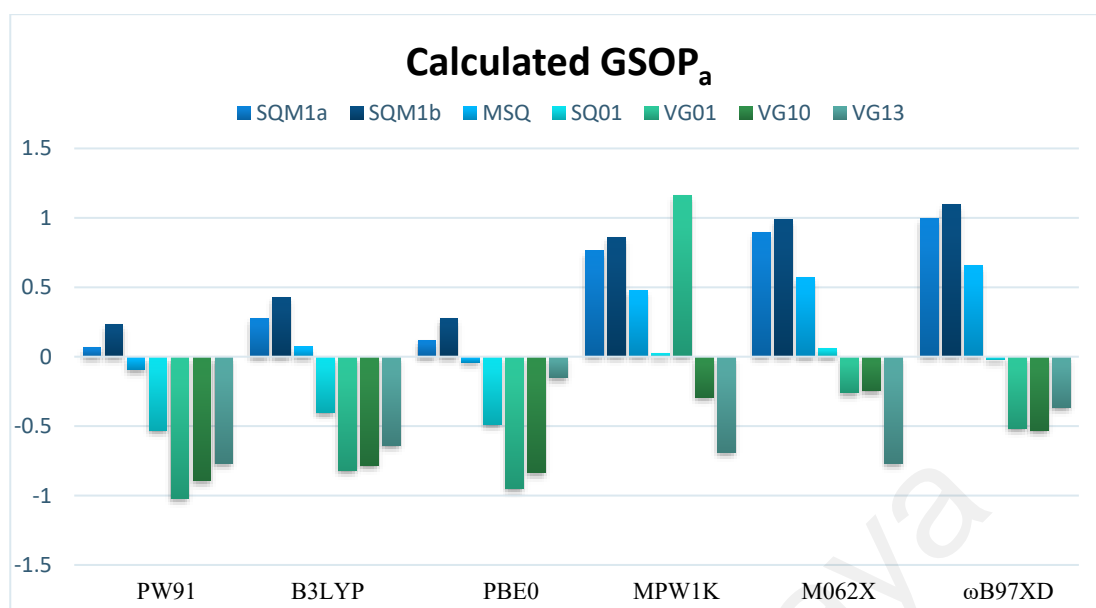


Figure 4.5: Absolute errors for the calculated Squarine Dyes via GSOP_a using different functionals based on the C-PCM framework.

The corresponding absolute error for squarine derivative obtained via calculation of GSOP_a using different density functionals are displayed in figure 4.5. Considering all functionals employed, the least absolute error is obtained from M062X with 0.177 eV. Therefore, calculation of GSOPs involving free energy difference between neutral and oxidized species favour large amount of non-local Hartree-Fock exchange.

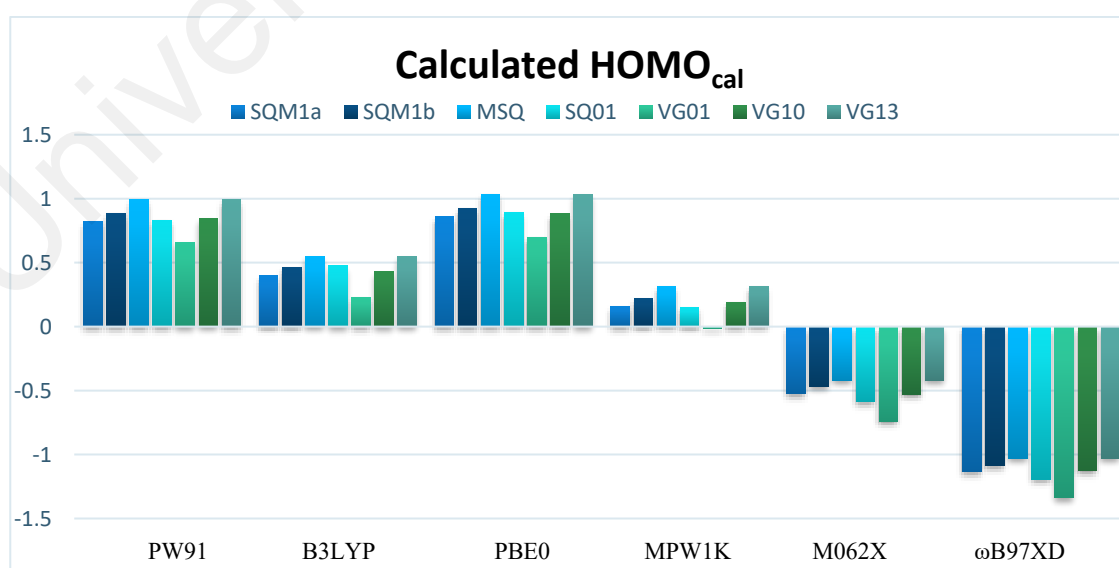


Figure 4.6: Absolute errors for the calculated Squarine Dyes via HOMO_{cal} using different functionals based on the C-PCM framework.

Based on Figure 4.6, for oxidation potential obtained based on Koopmans' Theorem, MPW1k is favoured with absolute error of 0.19 eV. Since both MPW1k and M062X density functionals have successfully benchmark experiment oxidation potential, it can be said that the true oxidation potential resides in between 42 – 54% HF E_{xc} term. This opens up to a new research line as more parameter can be considered and investigated such as ESOP, dye polarity and solvent effect in order to confirm the exact HF E_{xc} term percentage needed to benchmark squaraine dye HOMO.

A better correlation is seen for calculated $GSOP_v$ using different density functional than calculated $GSOP_a$ and $HOMO_{cal}$. Among density functional employed, M062X showed theoretical oxidation potential that correlate well with experiment value with absolute error of 0.14 eV. Theoretical oxidation potential obtained from calculated $GSOP_v$ employing M062X functional followed the same trend in energy level over series of differently structured squaraine.

Two major points are proven from this finding. Calculation method chosen and density functional employed are independent on structurally symmetry or unsymmetrical dye sensitizer. Secondly, the correct relative HOMO level for squaraine based dye can be obtained from calculated $GSOP_v$ using M062X. The commonly employed density functional, B3LYP is analyzed over 3 methods. However, neither the theoretical oxidation potential correlate well with experiment value nor the experimental trend. Thus, B3LYP can be said to give inaccurate results for these types of compound. In recent study, Gapol et al has proven that B3LYP is not suitable to benchmark tetraphenylbenzidine (TPB) oxidation potential (Gapol et al., 2017).

On the contrary, the reliability of B3LYP to simulate band gap is unquestionable as many studies have been done, providing a cheaper method in simulating the optical property of a dye sensitizer. Therefore, M062X is chosen to simulate SQM1a compound according to Dewar's rule. The calculated GSOP_v, GSOP_a, and HOMO_{cal} using different density functional over series of squarine based dye are assessed deeply in section below.

Table 4.2: Calculated GSOP_v, GSOP_a, HOMO_{cal} for Compound SQM1a Using Various Density Functional.

SQM1a	Density Functional	E(M) a.u	E ⁺ (M) a.u	E(M)-E ⁺ (M) a.u	GSOP _v eV
	B3LYP	-2105.3841	-2105.5774	-0.1933	-5.26
M062X	-2104.5168	-2104.7229	-0.2061	-5.61	
MPW1K	-2104.9026	-2105.1150	-0.2124	-5.78	
PBE0	-2102.8237	-2103.0217	-0.1980	-5.39	
PW91	-2104.6191	-2104.8190	-0.1999	-5.44	
ωB97XD	-2104.7363	-2104.9487	-0.2124	-5.78	
Density Functional	E(M) a.u	E ⁺ (M) a.u	E(M)-E ⁺ (M) a.u	GSOP _a eV	
B3LYP	-2105.3841	-2105.1945	-0.18969	-5.16	
M062X	-2104.5168	-2104.3130	-0.20381	-4.55	
MPW1K	-2104.9026	-2104.6939	-0.20866	-4.68	
PBE0	-2102.8237	-2102.6281	-0.19557	-5.32	
PW91	-2104.6191	-2104.4216	-0.19751	-5.37	
ωB97XD	-2104.7363	-2104.5361	-0.20015	-5.45	
Density Functional	E(M) a.u	E ⁺ (M) a.u	HOMO _{cal} a.u	HOMO _{cal} e.v	
B3LYP	-	-	-0.18536	-5.04	
M062X	-	-	-0.219	-5.96	
MPW1K	-	-	-0.19412	-5.28	
PBE0	-	-	-0.16841	-4.58	
PW91	-	-	-0.16983	-4.62	
ωB97XD	-	-	-0.24163	-6.58	
Experimental Value, (Oxidation Potential)				-5.44	

Table 4.2 shows calculated HOMO_{cal} and GSOPs using different functional to benchmark the oxidation potential level for SQM1a dye. Based on Table 4.2, calculation employed via GSOP_v using pure DFT functional, PW91 yields the exact experimental value for compound SQM1a. Pure DFT has successfully benchmark the oxidation potential level for SQM1a. Calculation via GSOP_v from B3LYP and PBE0 density functional overestimate the experimental value. In the case of using PBE0 density functional via GSOP_v , a result close to the experimental value (oxidation potential) is obtained. Calculation using PBE0 overestimate oxidation potential level by 0.05 eV. Decreasing the HF E_{xc} term to 20% and following the B88 gradient correction to local LSDA E_{xc} term, B3LYP overestimate the oxidation potential value by 0.18 eV.

In contrast, calculation obtained from MPW1K, M062X and ω B97XD density functional underestimate the oxidation potential value. A third calculated HOMO is obtained via M062X density functional, underestimate experimental oxidation potential by -0.17 eV. A trend can be seen by looking at the gradient corrected exchange and correlation functional. A pure DFT with 0% HF E_{xc} term yields an accurate result, an indication of a good density functional to benchmark SQM1a oxidation potential level. Incorporating the HF exchange term will either overestimate or underestimate the oxidation potential value. B3LYP and PBE0 having 20% and 25% HF E_{xc} term respectively overestimate the oxidation potential value. Increasing further the HF E_{xc} will eventually underestimate the oxidation potential value as proven by calculation via GSOP_v obtained from MPW1K (42% HF E_{xc}), M062X (54% HF E_{xc}) and range separated hybrid functional ω B97XD.

Calculation via GSOP_a follows different trend. Range separated hybrid functional is more favourable than pure DFT. ω B97XD density functional has successfully benchmark oxidation potential by -0.01 eV. The reason is because ω B97XD is capable of capturing short range and long ranges interaction.

Hence, a range separated functional will be more suitable to describe a charge transfer system like GSOP_a. Pure DFT functional, PW91 overestimate oxidation potential level by 0.07 eV. Third density functional that close to benchmarking experimental value is the meta-hybrid GGA, M062X. M062X underestimate oxidation potential value by -0.11 eV, consistent with previous method obtained via GSOP_v.

Moving away from a 54% HF E_{xc} term, MPW1k density functional with 42 % HF E_{xc} term underestimate oxidation potential value by -0.24 eV. Decreasing the HF E_{xc} term percentage results in overestimation on oxidation potential level. Both PBE0 and B3LYP overestimate oxidation potential energy level by 0.12 eV and 0.28 eV respectively.

Based on Figure 4.7, calculation via GSOP_v using PW91 density functional gives zero absolute error, indicating that a pure density functional is the most favourable among other functionals for benchmarking SQM1a oxidation potential energy level. Next, the smallest absolute error is obtained via GSOP_a using the range separated hybrid functional, ω B97XD with an absolute error of -0.01 eV.

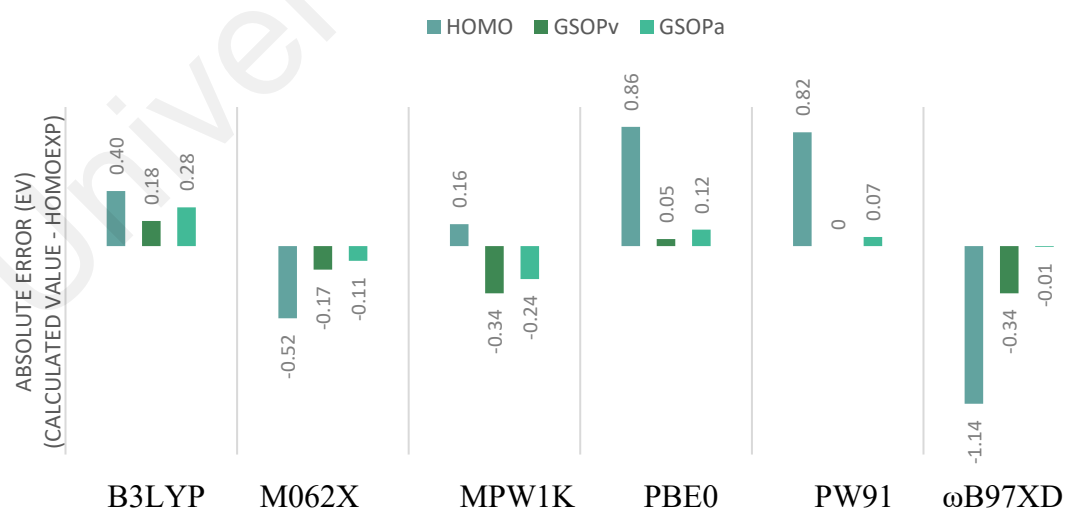


Figure 4.7: Absolute errors of the calculated HOMO_{cal}, GSOP_v, and GSOP_a of SQM1a using different functionals in Chloroform based on the C-PCM framework.

Considering all three methods employed based on Figure 4.7, pure density functional, PW91, and two global hybrid functionals, B3LYP and PBE0, show positive absolute errors, indicating an overestimation in oxidation potential energy level.

An exception for method calculated via HOMO_{cal} using MPW1K, all density functionals with big HF E_{xc} term underestimate SQM1a oxidation potential energy level with negative absolute error. Method proceed via HOMO_{cal} favours MPW1K density functional, a special case with the least absolute error as compared to other functionals. An absolute error of 0.16 eV is obtained which overestimate the oxidation potential value.

Both calculation via GSOP_v and GSOP_a using MPW1K underestimate the HOMO energy level with negative absolute error. There is no clear correlation for HOMO_{cal} due to the fact that the second and third lowest absolute errors belong to B3LYP functional with 20% HF E_{xc} term and M062X functional with 25 % HF E_{xc} term respectively.

In sequence for the least absolute error, benchmarking SQM1a oxidation potential via HOMO_{cal} favours density functional of MPW1K ($\alpha = 42$) < B3LYP ($\alpha = 20$) < M062X ($\alpha = 54$) < PW91 ($\alpha = 0$) < PBE0 ($\alpha = 25$) < ω B97XD, where α is the mixing fraction for generalized gradient approximation.

Three different methods in benchmarking oxidation potential level for unsymmetrical dye, SQM1b compound are recorded in Table 4.3. Based on table below, calculation employed via GSOP_a using meta-hybrid GGA functional, M062X yields -5.42 eV, the closest value to SQM1b oxidation potential, -5.41 eV, as compared to other density functionals.

It can be said that GSOP_a using M062X density functional has successfully benchmark the oxidation potential level for SQM1b. Considering all density functionals used by GSOP_a , the calculated oxidation potential varies from -4.98 eV to -5.55 eV.

Density functional with HF E_{xc} term of less than 25%, an exception for ω B97XD, will give a value lower than the actual oxidation potential. In contrast, calculation of GSOP_a using density functional of more than 25% yield an oxidation potential much lower than the actual oxidation potential value.

Table 4.3 shows three different methods in benchmarking oxidation potential level for unsymmetrical dye, SQM1b compound. Based on table above, calculation employed via GSOP_a using meta-hybrid GGA functional, M062X yields -5.42 eV, the closest value to SQM1b oxidation potential, -5.41 eV, as compared to other density functionals. It can be said that GSOP_a using M062X density functional has successfully benchmark the oxidation potential level for SQM1b.

Considering all density functionals used by GSOP_a, the calculated oxidation potential varies from -4.98 eV to -5.55 eV. Density functional with HF E_{xc} term of less than 25%, an exception for ω B97XD, will give a value lower than the actual oxidation potential. In contrast, calculation of GSOP_a using density functional of more than 25% yield an oxidation potential much lower than the actual oxidation potential value.

Following GSOP_v method to describe the oxidation potential level for unsymmetrical dye, SQM1b, calculated oxidation potential varies from -5.09 eV to -5.66 eV. The closest calculated value of oxidation potential obtained is -5.24 eV, obtained from a pure density functional, PW91. An overestimation of oxidation potential value by 0.17 eV, PW91 is still the most favourable density functional for SQM1a and SQM1b following the GSOP_v method.

Table 1.3: Calculated GSOP_v and GSOP_a for Compound SQM1b Using Various Density Functional.

COMPOUND	Density Functional	E(M) a.u	E ⁺ (M) a.u	E(M)- E ⁺ (M) a.u	GSOP _v eV
SQM1b	B3LYP	-1916.8069	-1916.6199	-0.1871	-5.09
	M062X	-1916.0027	-1915.7973	-0.2054	-5.59
	MPW1K	-1916.3702	-1916.1622	-0.2080	-5.66
	PBE0	-1914.4312	-1914.2402	-0.1911	-5.20
	PW91	-1916.0872	-1915.8947	-0.1926	-5.24
	ωB97XD	-1916.2142	-1916.0066	-0.2076	-5.65
	Density Functional	E(M) a.u	E ⁺ (M) a.u	E(M)- E ⁺ (M) a.u	GSOP _a eV
B3LYP	-1916.8069	-1916.6238	-0.1832	-4.98	
M062X	-1916.0027	-1915.8034	-0.1993	-4.42	
MPW1K	-1916.3702	-1916.1662	-0.2040	-4.55	
PBE0	-1914.4312	-1914.2426	-0.1886	-5.13	
PW91	-1916.0872	-1915.8971	-0.1902	-5.18	
ωB97XD	-1916.2142	-1916.0190	-0.1952	-4.31	
Density Functional	E(M) a.u	E ⁺ (M) a.u	IP a.u	HOMO _{cal} e.v	
B3LYP	-	-	-0.1819	-4.95	
M062X	-	-	-0.2160	-5.88	
MPW1K	-	-	-0.1907	-5.19	
PBE0	-	-	-0.1649	-4.49	
PW91	-	-	-0.1662	-4.52	
ωB97XD	-	-	-0.2388	-6.50	
Experimental Value				-5.41	

Calculated oxidation potential for SQM1b obtained by B3LYP and PBE0 overestimate the experimental value with -5.09 eV and -5.20 eV respectively. Following the same GSOP_v trend as obtained from SQM1a, hybrid density functional with 20% - 25% HF E_{xc} term will overestimate oxidation potential value.

Increasing the HF E_{xc} term from 42% - 100% will underestimate oxidation potential value. There is no clear trend in the percentage of HF E_{xc}, towards the oxidation potential.

M062X with 54% HF E_{xc} term has a value of -5.59eV , the closest oxidation potential value obtained among two other density functionals with big HF E_{xc} term. Density functional ωB97XD showed a reading of -5.65 eV and MPW1K drifted the furthest in oxidation potential value from experiment, with -5.66 eV .

MPW1K has the smallest HF E_{xc} term compared to M062X and ωB97XD , yet it produces a more negative oxidation potential value. Hence, no clear relationship between the percentage of HF E_{xc} term and oxidation potential is proven. However, there is a clear indication to where the actual value of oxidation potential resides based on the percentage range of HF E_{xc} term used.

Obtaining calculated oxidation potential for unsymmetrical dye, SQM1b via Koopman's theorem, HOMO_{cal} , has been unpromising. Considering all functionals used via HOMO_{cal} , the absolute error obtained vary from $0.22 - 1.09\text{ eV}$. The value obtained from MPW1K is the closest among other density functional used, -5.19 eV which overestimate oxidation potential by $+0.22\text{ eV}$. -6.50 eV is obtained using ωB97XD , which gives the worst description of oxidation potential.

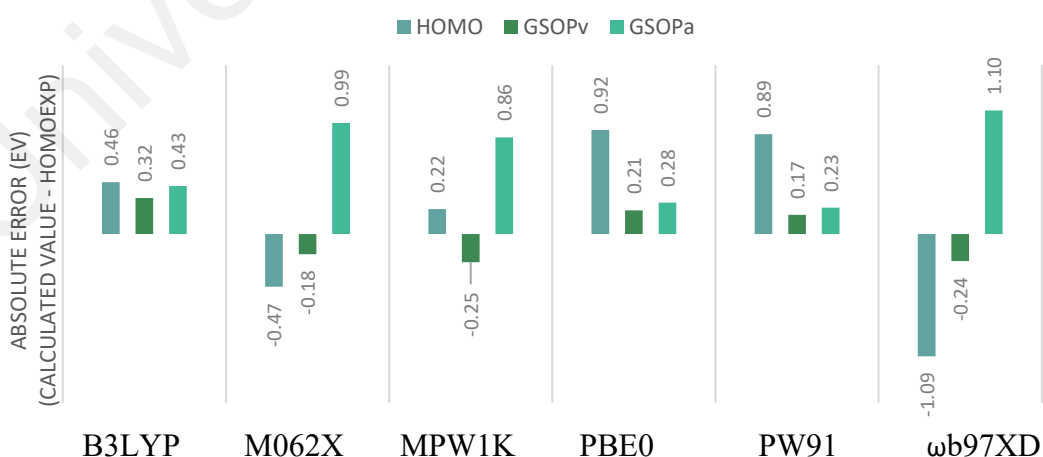


Figure 4.8: Absolute errors of the calculated HOMO_{cal} , GSOPv, and GSOPa of SQM1b using different functionals in Chloroform based on the C-PCM framework.

All calculations for oxidation potential using HOMO_{cal} obtained for compound SQM1b follow the same trend as obtained from SQM1a. MPW1K density functional gives the least absolute error with 0.22eV from the experimental oxidation potential. Range separated functional, ωB97XD portrayed the biggest absolute error for both dyes.

Following Koopman's Theorem, there were no clear trend in the usage of density functionals. Density functional with 0 - 25% HF E_{xc} term will overestimate oxidation potential value. GGA mixing fraction, α with more than 42, ($\alpha > 42$) results in underestimation of oxidation potential.

In sequence for the least absolute error, benchmarking SQM1b oxidation potential via HOMO_{cal} favours density functional of MPW1K ($\alpha = 42$) < B3LYP ($\alpha = 20$) < M062X ($\alpha = 54$) < PW91 ($\alpha = 0$) < PBE0 ($\alpha = 25$) < ωB97XD , where α is the mixing fraction for generalized gradient approximation. On the contrary, calculation via GSOP_v favours density functional of PW91 ($\alpha = 0$) < M062X ($\alpha = 54$) < PBE0 ($\alpha = 25$) < ωB97XD < MPW1K ($\alpha = 42$) < B3LYP ($\alpha = 20$). GSOP_a favours density functional of PW91 ($\alpha = 0$) < PBE0 ($\alpha = 25$) < B3LYP ($\alpha = 20$) < MPW1K ($\alpha = 42$) < M062X ($\alpha = 54$) < ωB97XD .

For both SQM1a and SQM1b consistently displayed the least absolute error on density functional employed and calculation methodologies. HOMO_{cal} favours MPW1k, and both GSOP_v and GSOP_a favour pure density functional, PW91.

Table 4.4: Calculated GSOP_v, GSOP_a and HOMO_{cal} for Compound MSQ Using Various Density Functional.

COMPOUND MSQ	Density Functional	E(M) a.u	GSOP _v E ⁺ (M) a.u	E(M)- E ⁺ (M) a.u	IP eV
	B3LYP	-1768.2429	-1768.0499	-0.1929	-4.75
M062X	-1767.4839	-1767.2814	-0.2025	-5.51	
MPW1K	-1767.8484	-1767.6706	-0.1779	-5.36	
PBE0	-1766.0482	-1765.8512	-0.1970	-4.84	
PW91	-1767.5752	-1767.3764	-0.1988	-5.25	
ωB97XD	-1767.7055	-1767.4975	-0.2080	-5.66	
Density Functional	E(M) a.u	GSOP _a E ⁺ (M) a.u	E(M)- E ⁺ (M) a.u	IP eV	
B3LYP	-1768.2429	-1768.0463	-0.1966	-5.25	
M062X	-1767.4839	-1767.3035	-0.1804	-4.75	
MPW1K	-1767.8484	-1767.6665	-0.1819	-4.84	
PBE0	-1766.0482	-1765.8487	-0.1995	-5.36	
PW91	-1767.5752	-1767.3742	-0.2010	-5.41	
ωB97XD	-1767.7055	-1767.5217	-0.1837	-4.66	
Density Functional	E(M) a.u	HOMO E ⁺ (M) a.u	IP a.u	IP e.v	
B3LYP	-	-	-0.17529	-4.77	
M062X	-	-	-0.21107	-5.74	
MPW1K	-	-	-0.18396	-5.01	
PBE0	-	-	-0.15751	-4.29	
PW91	-	-	-0.15892	-4.32	
ωB97XD	-	-	-0.23336	-6.35	
Experimental Value				-5.32	

Based on Figure 4.9, two density functional namely MPW1k and PBE0 obtained from different calculation shared the same absolute error and both displayed the least absolute error. These can also be seen in Table 4.4 whereby, both MPW1k and PBE0 calculated via GSOP_v and GSOP_a possessed the same oxidation potential, -5.36 eV.

For this very reason, conclusion to find the best method in benchmarking oxidation potential cannot be drawn. More organic dyes are required to determine the reliability of calculation performed. Hence, organic dyes VG1, SQ01, VG10 and VG13 are introduced.

Both density functionals underestimate oxidation potential level for compound MSQ. Calculation employed via GSOP_a favours density functional with less HF E_{xc} term. In decreasing order, pure density functional, PW91 underestimate oxidation potential level by 0.09 eV. Next, 20% HF E_{xc} term density functional, B3LYP overestimate oxidation potential level by 0.07.

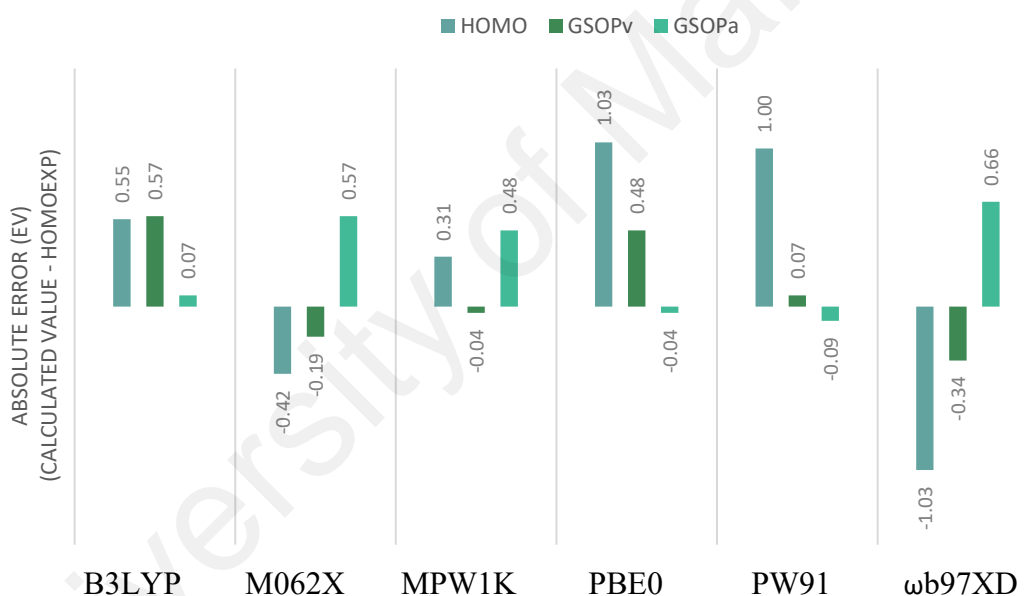


Figure 4.9: Absolute errors for the calculated HOMO_{cal}, GSOP_v, and GSOP_a of MSQ using different functionals in Chloroform based on the C-PCM framework.

Lastly, PBE0 density functional underestimate oxidation potential by 0.04 eV. MPW1k having $\alpha = 42$ overestimate oxidation potential level by 0.48 eV with the least absolute error among the 2 other compatriots, M062X and ωB97XD. All large GGA mixing fraction, α density functionals employed via GSOP_a overestimate oxidation potential with increasing absolute error. The order of absolute error increased with increasing GGA mixing fraction, α .

Calculation employed via GSOP_v showed a different trend than GSOP_a. All small GGA mixing fraction, α overestimate MSQ dye oxidation potential level. Pure density functional, PW91 with 0% HF E_{xc} term displayed the least absolute error following GSOP_v method. Calculated dye overestimate MSQ oxidation potential by 0.07 eV. B3LYP overestimate oxidation potential tremendously by 0.57 eV and increasing HF E_{xc} term decreases the absolute error.

Absolute error drop by 0.9 eV when 20% HF E_{xc} term is decreased to 25% HF E_{xc} term, PBE0. The order of absolute error increased with increasing GGA mixing fraction, α . MPW1k ($\alpha = 42\%$) having only 0.04 eV below MSQ oxidation potential level and M062X and ω B97XD with 0.19 and 0.34 eV respectively.

Initially, this research is meant to explore symmetrical and unsymmetrical dye between SQM1a and SQM1b with MSQ as dye reference. Since MPW1k and PBE0 generated the same energy level when calculated via GSOP_v and GSOP_a respectively, more organic dyes are required for determination on the best method to benchmark oxidation potential. Hence, symmetrical organic dyes, VG1 and VG10 as well as unsymmetrical dyes, SQ01 and VG13 are introduced.

Based on results obtained from SQM1a, SQM1b and MSQ, Koopman's Theorem displayed an unpromising outcome in simulating oxidation potential. However, the case for VG1 has proven that Koopman's Theorem is still one of the possible candidates in benchmarking oxidation potential. Based on Table 4.5, oxidation potential obtained from HOMO_{cal} employing MPW1k density functional displayed -5.16 eV, underestimate the experimental oxidation potential by 0.01 eV. In contrast, using the same density functional, calculation proceeded via GSOP_a displayed a towering oxidation potential of -3.99 eV while GSOP_v showed -4.89 eV, overestimate experimental energy by 0.26 eV. Second close value to experimental oxidation potential is obtained by M062X calculated via

GSOP_v. -5.41 eV is obtained, underestimate oxidation potential by 0.1 eV. A small margin to be compared with B3LYP obtained via HOMO_{cal}. B3LYP proceeded via HOMO_{cal} produced -4.92 eV, overestimate oxidation potential by 0.13 eV from M062X calculated via GSOP_v. Despite the good calculation record obtained by HOMO_{cal}, a large HF E_{xc} term cannot be employed since a very large absolute error is produced.

Table 4.5: Calculated GSOP_v and GSOP_a for Compound VG1 Using Various Density Functional.

COMPOUND VG1	Density Functional	E(M) a.u	GSOP _v		IP eV
			E ⁺ (M) a.u	E(M)- E ⁺ (M) a.u	
	B3LYP	-2271.3355	-2271.1197	-0.2159	-5.87
	M062X	-2270.3454	-2270.1524	-0.1930	-5.25
	MPW1K	-2270.8278	-2270.6483	-0.1796	-4.89
	PBE0	-2268.4957	-2268.2739	-0.2218	-6.03
	PW91	-2270.4578	-2270.2334	-0.2244	-6.11
	ωB97XD	-2270.6576	-2270.4542	-0.2034	-5.53
	Density Functional	E(M) a.u	GSOP _a		IP eV
			E ⁺ (M) a.u	E(M)- E ⁺ (M) a.u	
	B3LYP	-2271.3355	-2271.1161	-0.2195	-5.97
	M062X	-2270.3454	-2270.1467	-0.1987	-5.41
	MPW1K	-2270.8278	-2270.6445	-0.1833	-3.99
	PBE0	-2268.4957	-2268.2715	-0.2242	-6.10
	PW91	-2270.4578	-2270.2310	-0.2268	-6.17
	ωB97XD	-2270.6576	-2270.4493	-0.2084	-5.67
	Density Functional	E(M) a.u	HOMO		IP e.v
			E ⁺ (M) a.u	IP a.u	
	B3LYP	-	-	-0.1809	-4.92
	M062X	-	-	-0.2164	-5.89
	MPW1K	-	-	-0.1898	-5.16
	PBE0	-	-	-0.1635	-4.45
	PW91	-	-	-0.1650	-4.49
	ωB97XD	-	-	-0.2385	-6.49
Experimental Value					-5.15

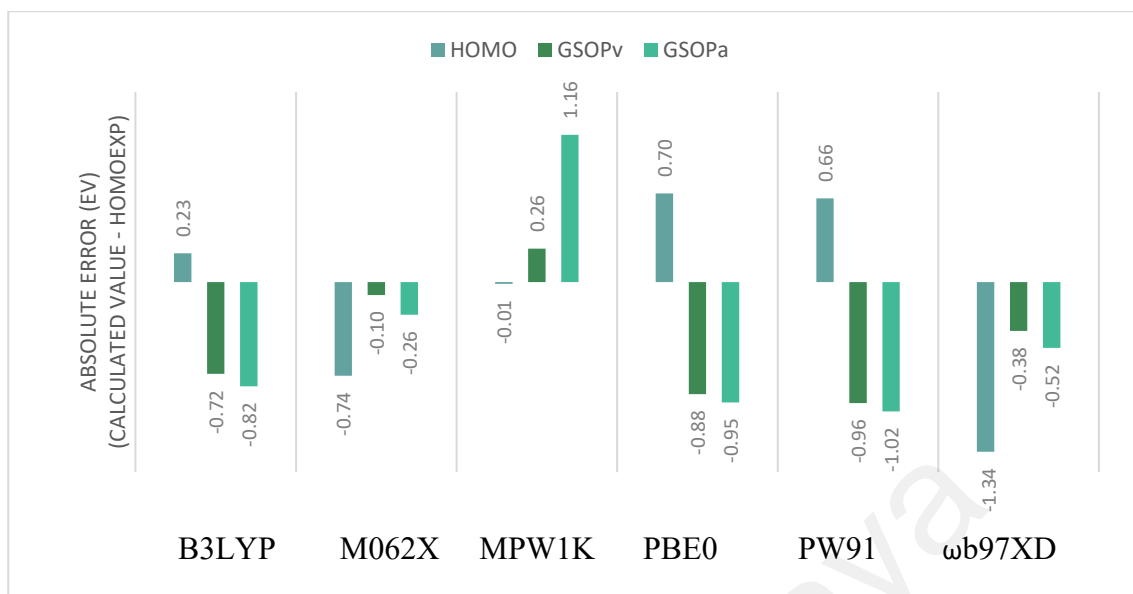


Figure 4.10: Absolute errors for the calculated HOMO_{cal}, GSOP_v, and GSOP_a of VG1 using different functionals in Chloroform based on the C-PCM framework.

Calculation by ωB97XD density functional via HOMO_{cal} produced -6.49 eV, underestimate oxidation potential by -1.34 eV. Hence, oxidation potential calculation by HOMO_{cal} can be accurate when 42% HF E_{xc} term is used. Increasing HF E_{xc} term underestimate oxidation potential significantly. On the contrary, decreasing HF E_{xc} term overestimate oxidation potential with an exception for oxidation potential calculated by 20% HF E_{xc} term.

Based on Figure 4.10, experimental oxidation potential is best described by MPW1k density functional calculated via HOMO_{cal}. However, calculation using the same density functional but proceeded via GSOP_a portrayed worse absolute error, overestimate oxidation potential by 1.16 eV and 0.18eV away from being the worst calculated oxidation potential. This proves that density functional alone cannot be used solely for benchmarking oxidation potential. The best density functional that provide a good agreement between experimental and theoretical data is obtained by either HOMO_{cal}, GSOP_v, or GSOP_a.

Table 4.6: Calculated GSOP_v and GSOP_a for Compound SQ01 Using Various Density Functional.

COMPOUND SQ01	Density Functional	E(M) a.u	GSOP _v E ⁺ (M) a.u	E(M)- E ⁺ (M) a.u	IP eV
	B3LYP	-1846.8740	-1846.6709	-0.2031	-5.53
M062X	-1846.0729	-1845.8779	-0.1949	-5.30	
MPW1K	-1846.4626	-1846.2754	-0.1872	-5.09	
PBE0	-1844.5641	-1844.3568	-0.2073	-5.64	
PW91	-1846.1651	-1845.9560	-0.2091	-5.69	
ωB97XD	-1846.3151	-1846.0979	-0.2171	-5.91	
Density Functional	E(M) a.u	GSOP _a E ⁺ (M) a.u	E(M)- E ⁺ (M) a.u	IP eV	
B3LYP	-1846.8740	-1846.6673	-0.2067	-5.62	
M062X	-1846.0729	-1845.8833	-0.1896	-5.16	
MPW1K	-1846.4626	-1846.2716	-0.1910	-5.20	
PBE0	-1844.5641	-1844.3544	-0.2097	-5.71	
PW91	-1846.1651	-1845.9536	-0.2115	-5.75	
ωB97XD	-1846.3151	-1846.1224	-0.1927	-5.24	
Density Functional	E(M) a.u	HOMO E ⁺ (M) a.u	IP a.u	IP e.v	
B3LYP	-	-	-0.1744	-4.75	
M062X	-	-	-0.2134	-5.81	
MPW1K	-	-	-0.1863	-5.07	
PBE0	-	-	-0.1590	-4.33	
PW91	-	-	-0.1612	-4.39	
ωB97XD	-	-	-0.2356	-6.41	
Experimental Value				-5.22	

Based on Table 4.6, a good agreement on experimental and theoretical oxidation potential is found using single calculation method, GSOP_a. The two density functionals mentioned are MPW1k and ωB97XD. MPW1k density functional displayed -5.20 eV, overestimate experimental oxidation potential by 0.02 eV. On the contrary, -5.24 eV

oxidation potential is obtained by ω B97XD. Based on figure 4.8, ω B97XD shared the same absolute error with calculation obtained by MPW1k.

However, ω B97XD underestimate experimental oxidation potential by 0.02 eV. From the graph obtained in figure 4.8, calculation on oxidation potential favours GSOP_a method whereby 3 density functionals displayed a close theoretical oxidation potential value in agreement with experimental oxidation potential. The three density functionals have large HF E_{xc} term, they are, MPW1k ($\alpha = 42$), M062X ($\alpha = 54$), and ω B97XD. All three density functionals have small absolute error with both MPW1k and ω B97XD shared the same absolute error, 0.02 eV and M062X with 0.06 eV.

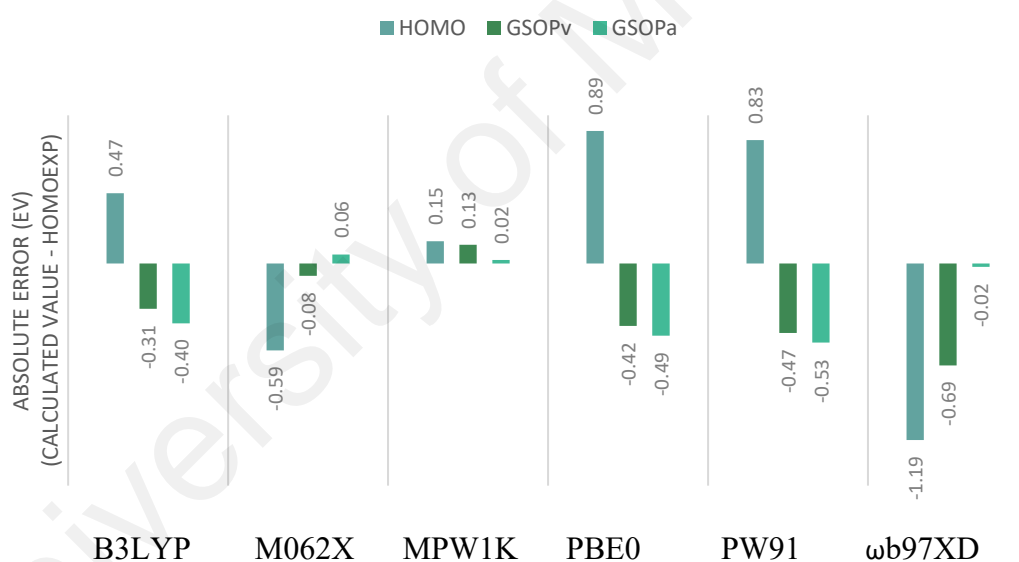


Figure 4.11: Absolute errors for the calculated HOMO_{cal}, GSOP_v, and GSOP_a of SQ01 using different functionals in Chloroform based on the C-PCM framework.

All density functional with small HF E_{xc} terms calculated via GSOP_v and GSOP_a underestimate oxidation potential. B3LYP calculated via GSOP_v and GSOP_a showed the smaller absolute error in comparison with PBE0 and PW91. A different case is displayed for calculation proceeded via HOMO_{cal}.

All calculations proceeded via HOMO_{cal} employing density functionals with small HF E_{xc} term overestimate oxidation potential. Large absolute errors are obtained except for MPW1k. The largest absolute error obtained from ω B97XD density functional underestimate experiment oxidation potential by 1.19 eV.

From Figure 4.11, PBE0 calculated via HOMO_{cal} displayed second largest absolute error, overestimate experiment value by 0.89 eV. An optimum oxidation potential resided on 42% HF E_{xc} term density functional, MPW1k. Continuing discussion for calculation proceeded via HOMO_{cal}, the least absolute error is displayed by MPW1k, overestimate oxidation potential by 0.15 eV. No clear trend in using different density functional when Koopman's Theorem, HOMO_{cal} is employed for benchmarking compound SQ01 oxidation potential.

In contrast, vertical and adiabatic ground state oxidation potential have proven the correlation between HF E_{xc} term in every density functional employed and theoretical oxidation potential obtained. Calculation proceeded via HOMO_{cal} using MPW1k density functional displayed small absolute error for both compound SQ01 and VG1.

This is due to the similar chromophore in both VG1 and SQ01. Both dyes VG1 and SQ01 belong to symmetrical and unsymmetrical squarine dye respectively. Based on Figure 4.11, both density functional calculated via GSOP_a, MPW1k and ω B97XD were found to be the best performing functional since a large HF E_{xc} is needed.

The use of dispersion-corrected effect in ω B97XD does not lead to significantly improved description on dye oxidation potential (Tortorella et al., 2016). Calculation employed via HOMO_{cal} for both VG1 and SQ01 dyes displayed the largest absolute error when ω B97XD is used. Percentage of HF E_{xc} term has proven to be the dominant effect in benchmarking oxidation potential. Two density functionals with small HF E_{xc} term, namely

PW91 and PBE0 provided second and third worst absolute error among series of density functional employed via HOMO_{cal}.

Table 4.7: Calculated HOMO_{cal}, GSOP_v and GSOP_a for Compound VG10 Using Various Density Functional.

COMPOUND VG10	Density Functional	E(M) a.u	GSOP _v E ⁺ (M) a.u	E(M)- E ⁺ (M) a.u	IP eV
	B3LYP	-2106.8514	-2106.6344	-0.2171	-5.91
M062X	-2105.9931	-2105.7979	-0.1952	-5.31	
MPW1K	-2106.3818	-2106.1830	-0.1988	-5.41	
PBE0	-2104.3205	-2104.1004	-0.2201	-5.99	
PW91	-2106.1092	-2105.8871	-0.2222	-6.05	
ωB97XD	-2106.1986	-2105.9996	-0.1991	-5.42	
GSOP _a					
Density Functional	E(M) a.u	E ⁺ (M) a.u	E(M)- E ⁺ (M) a.u	IP eV	
B3LYP	-2106.8514	-2106.6307	-0.2207	-6.01	
M062X	-2105.9931	-2105.7922	-0.2009	-5.47	
MPW1K	-2106.3818	-2106.1793	-0.2025	-5.51	
PBE0	-2104.3205	-2104.0980	-0.2225	-6.05	
PW91	-2106.1092	-2105.8847	-0.2246	-6.11	
ωB97XD	-2106.1986	-2105.9873	-0.2114	-5.75	
HOMO					
Density Functional	E(M) a.u	E ⁺ (M) a.u	IP a.u	IP e.v	
B3LYP	-	-	-0.1761	-4.79	
M062X	-	-	-0.2112	-5.75	
MPW1K	-	-	-0.1850	-5.03	
PBE0	-	-	-0.1594	-4.34	
PW91	-	-	-0.1608	-4.38	
ωB97XD	-	-	-0.2333	-6.35	
Experimental Value				-5.22	

On the contrary, calculations proceeded via GSOP_v and GSOP_a have shown the reliability of PW91 and PBE0 functional. Hence, method to determine theoretical oxidation potential is found to be independent on the the amount of HF E_{xc} term used.

Calculation on symmetrical bis(benzoindolenine) squaraine sensitizers coded as VG10 to simulate theoretical oxidation potential have been done and tabulated in Table 4.7. Among the 3 methods employed, density functional M062X calculated via GSOP_v exhibited the closest oxidation potential to the experimental energy level with -5.31 eV.

Using the same methodology, MPW1k and ω B97XD showed -5.41 and -5.42 eV respectively. Thus, second and third oxidation potential that came close to experimental oxidation potential is evaluated by GSOP_v.

Large HF E_{xc} term dominated the evaluation for VG10 oxidation potential. B3LYP and PBE0 calculation via GSOP_v displayed oxidation potential of -5.91 eV and -5.99 eV respectively. Both density functional underestimate experimental oxidation potential by 0.69 eV and 0.77 eV respectively. Pure density functional, PW91 provided the worst theoretical oxidation potential with -6.05 eV, underestimate experimental oxidation potential by 0.83 eV.

All density functional calculated by GSOP_v and GSOP_a underestimate oxidation potential as shown in Figure 4.12. M062X has been the ideal density functional that best describe VG10 experimental potential with both calculations proceeded via GSOP_v and GSOP_a displayed the least absolute error.

All density functional with large HF E_{xc} term calculated via GSOP_v displayed small absolute error between 0.09 eV to 0.20 eV. However, the least absolute error resides on 54% HF E_{xc} term, M062X. A decrease in 8% HF E_{xc} term brought down absolute error to 0.19 eV. Also, an increase in HF E_{xc} term pulled absolute error to 0.2 eV.

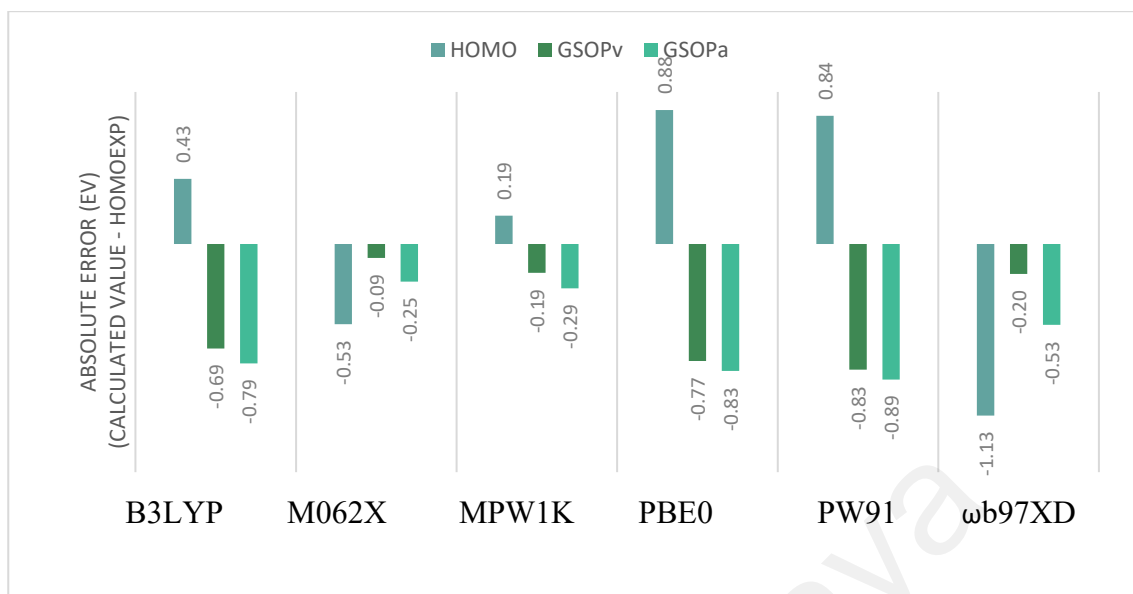


Figure 4.12: Absolute errors for the calculated HOMO_{cal} , GSOP_v , and GSOP_a of VG10 using different functionals in Chloroform based on the C-PCM framework.

Large absolute errors are shown when density functional with small HF E_{xc} term is used. Following GSOP_v calculation, pure density functional, PW91 underestimate experimental oxidation potential by 0.83 eV. The biggest absolute error for compound VG10 when compared with other density functional. B3LYP with 20% HF E_{xc} term underestimate experiment oxidation potential by 0.69 eV. An increased in absolute error is seen when 25% HF E_{xc} term is used when PBE0 is employed. PBE0 underestimate experiment oxidation potential by 0.77 eV.

Theoretical oxidation potential obtained from MPW1k density functional is favoured when calculation is proceeded via HOMO_{cal} . MPW1k produced the least absolute error compared to other density functionals. Second best absolute error is produced by B3LYP with 0.43 eV below experimental oxidation potential. The biggest absolute error is produced when a relatively large HF E_{xc} term is used, with 1.13 eV below experiment oxidation potential.

The trend between percentage of HF E_{xc} term and theoretical oxidation potential produced is not apparent. A large HF E_{xc} term both produced small and large absolute error

when M062X and ω B97XD are used respectively. Third best absolute error is produced when 54% HF E_{xc} term, M062X is employed.

Table 4.8: Calculated GSOP_v and GSOP_a for Compound VG13 Using Various Density Functional.

COMPOUND VG13	Density Functional	E(M) a.u	GSOP _v		IP eV
			E ⁺ (M) a.u	E(M)- E ⁺ (M) a.u	
	B3LYP	-2154.1559	-2153.9406	-0.2153	-5.86
	M062X	-2153.2348	-2153.0329	-0.2019	-5.49
	MPW1K	-2153.6798	-2153.4826	-0.1972	-5.37
	PBE0	-2151.4648	-2151.2757	-0.1890	-5.14
	PW91	-2153.3358	-2153.1144	-0.2213	-6.02
	ω B97XD	-2153.4949	-2153.2982	-0.1967	-5.35
	Density Functional	E(M) a.u	GSOP _a		IP eV
			E ⁺ (M) a.u	E(M)- E ⁺ (M) a.u	
	B3LYP	-2154.1559	-2153.9370	-0.2189	-5.96
	M062X	-2153.2348	-2153.0309	-0.2039	-6.05
	MPW1K	-2153.6798	-2153.4788	-0.2009	-5.47
	PBE0	-2151.4648	-2151.2439	-0.2208	-6.01
	PW91	-2153.3358	-2153.1120	-0.2237	-6.09
	ω B97XD	-2153.4949	-2153.2859	-0.2091	-5.69
	Density Functional	E(M) a.u	HOMO		IP e.v
			E ⁺ (M) a.u	IP a.u	
	B3LYP	-	-	-0.1736	-4.72
	M062X	-	-	-0.2020	-5.50
	MPW1K	-	-	-0.1825	-4.97
	PBE0	-	-	-0.1568	-4.27
	PW91	-	-	-0.1851	-5.04
	ω B97XD	-	-	-0.2312	-6.29
Experimental Value					-5.32

In comparison with other density functional calculated via HOMO_{cal} , ωB97XD produced the worst theoretical oxidation potential. Density functional ωB97XD underestimate experimental oxidation potential by 1.13 eV. Large absolute error is also produced by both PW91 and PBE0 with 0.84 eV and 0.88 eV respectively.

Unsymmetrical bis(benzoindolenine) squaraine sensitizers coded as VG13 is calculated by 3 methods via HOMO_{cal} , GSOP_v and GSOP_a . 6 density functionals are employed and tabulated in Table 4.8. From results obtained in table 9, GSOP_v method is favoured for the calculation of VG13 theoretical oxidation potential.

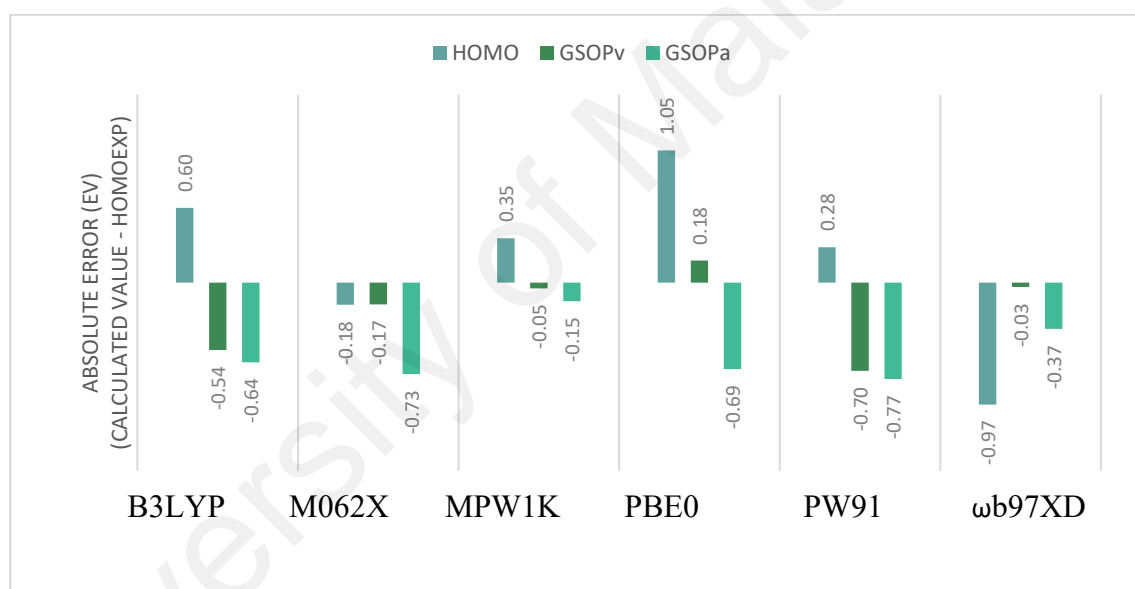


Figure 4.13: Absolute errors for the calculated HOMO_{cal} , GSOP_v , and GSOP_a of VG13 using different functionals in Chloroform based on the C-PCM framework.

Calculation by ωB97XD density functional via GSOP_v with -5.35 eV showed the closest energy level towards VG13 experimental oxidation potential. Second best theoretical oxidation potential in line with experimental oxidation potential is calculated by density functional MPW1k with -5.37 eV obtained via GSOP_v . Following the same method, GSOP_v , an energy level of -5.49 eV is obtained from M062X density functional. M062X density functional displayed the third best theoretical oxidation potential that best match with VG13 experimental oxidation potential.

A large percentage of HF E_{xc} is preferred for the calculation of VG13 theoretical oxidation potential when calculation is proceeded via GSOP_v. Based on figure 4.13, density functional with large HF E_{xc} term displayed the least absolute error following calculation via GSOP_v. Following GSOP_v calculation, ω B97XD with the largest HF E_{xc} term underestimate experimental oxidation potential energy level by 0.03 eV. Hence, among 6 density functional employed, the least absolute error resided on density functional with the largest HF E_{xc} term, ω B97XD.

However, the trend between percentage of HF E_{xc} term employed and theoretical oxidation potential produced is indeterminate. The third largest percentage of HF E_{xc} term used in density functional, MPW1k has produced the second least absolute error with 0.05 eV below experimental oxidation potential energy level. On the contrary, the third absolute error is produced by density functional with second largest HF E_{xc} term belonging to M062X which underestimate experimental oxidation potential by 0.17 eV.

All theoretical oxidation potential produced by GSOP_v calculation underestimate experiment oxidation potential with an exception of PBE0. Oxidation potential produced from calculation of PBE0 via GSOP_v overestimate energy level by 0.18 eV. A different trend is seen for calculation proceeded via GSOP_a.

Based on Figure 4.13, all theoretical oxidation potential underestimate experimental oxidation potential. The least absolute error produced following GSOP_a route belong to MPW1k with 0.15 eV below experimental oxidation potential. Both MPW1k and ω B97XD have shown oxidation potential not too far from the experiment value. Both MPW1k and ω B97XD have large HF E_{xc} term underestimate oxidation potential energy level by 0.15 eV and 0.37 eV respectively.

Incorporating 54% HF E_{xc} term from M062X has resulted in big absolute error. An unreliable theoretical oxidation potential has been generated from the use of M062X with 0.73 eV less in energy against experiment value. The possibility of using small percentage of HF E_{xc} term via GSOP_a to benchmark VG13 oxidation potential were found to be erratic. Based on table 9, density functional with small extent of HF E_{xc} term (0-25%) have produced small oxidation potential. Hence, a disagreement with experiment results with PW91, B3LYP and PBE0 produced an absolute error of 0.77 eV, 0.64 eV and 0.69 eV respectively.

Erratic trend is seen in Figure 4.13 with the incorporation of HF E_{xc} percentage term onto theoretical oxidation potential calculation via HOMO_{cal}. Moderate extent of HF E_{xc} term showed distinct value B3LYP and PBE0. Density functional with 25% HF E_{xc} term in PBE0 displayed a greater absolute error from 20% HF E_{xc} term in B3LYP. From figure 4.13, calculation by PBE0 overestimate oxidation potential by 1.05 eV while B3LYP overestimate oxidation potential by 0.64 eV. For pure density functional, PW91 theoretical oxidation potential obtained escalate experiment value by 0.28 eV.

Two different direction are exhibited on the effect of oxidation potential when density functionals with large HF E_{xc} percentage term are used. Two out of six density functionals appeared to align beneath experimental value. Absolute error of 0.18 eV and 0.97 eV are obtained from M062X and ω B97XD. On the contrary, MPW1k overestimate oxidation potential by 0.35 eV. As a conclusion to this sub-chapter, GSOP has been successfully benchmarked using GSOP_v employing M062X density functional simply because: (i) energy exhibited follow the same experimental trend; (ii) displayed the least MAE; (iii)

4.3 Excited State Calculation

Since GSOP has been successfully benchmarked by GSOP_v employing M062X density functional, single point calculation using TD-DFT over series of density functionals are performed. Optimized geometry by M062X functional via GSOP_v route is used as the starting geometry for TD-DFT calculation.

Due to limited time, SQM1a is the only dye taken to be studied in the excited state. One reason is because of the availability of the X-ray structure. Bond angle and length can be analyzed before and after excitation hence, providing insight to any distortion upon excitation (Hoffmann, 1970; Richards et al., 1963) and location on potential energy surface (PES).

Slight changes in sensitized dye π -spacer group resulted in major changes in frontier molecular orbitals (MOs). A minimal distortion in dye conformation upon excitation is desired. B3LYP calculated at ground state is denoted as B3LYP_{GS}. Density functionals B3LYP, PBE0, MPW1k, ω B97XD and M062X calculated at excited state are denoted as B3LYP_{ES}, PBE0_{ES}, MPW1k_{ES}, ω B97XD_{ES}, and M062X_{ES} respectively. Density functional B3LYP_{ES} showed the least absolute error compared to other density functionals.

All quantum mechanical calculated at excited state are proceeded by employing TD-DFT on the optimized geometry at ground state. Starting geometry of an optimized SQM1a by B3LYP is chosen because it showed the least absolute error between theoretical and experimental X-ray value. Diffused polarized double-zeta polarized basis set, $6-31+G(d)$ is employed in every excited state calculation.

This would add 6 d-type Cartesian Gaussian polarization function onto heavy atoms from Lithium to Calcium (Ditchfield et al., 1971). B3LYP calculated at ground state is denoted as B3LYP_{GS}. TD-DFT employing density functionals B3LYP, PBE0, MPW1k,

ω B97XD and M062X calculated at excited state are denoted as B3LYP_{ES}, PBE0_{ES}, MPW1k_{ES}, ω B97XD_{ES}, and M062X_{ES}. Density functional B3LYP_{ES} showed the least absolute error compared to other density functionals.

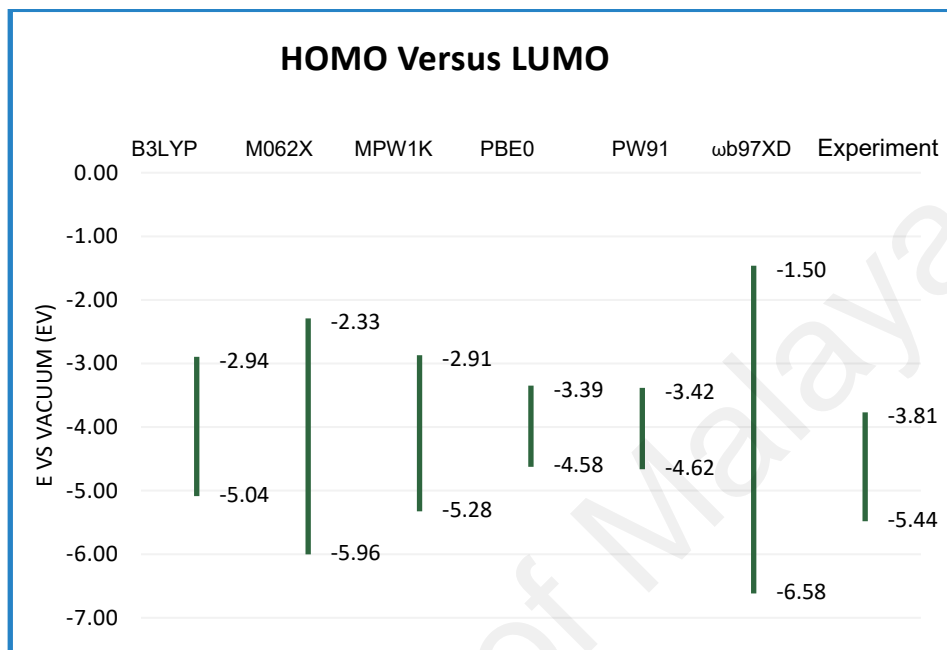


Figure 4.14: SQM1a energies comparison of the HOMOs (ϵ HOMO), the LUMOs (ϵ LUMO), the HOMO–LUMO energy gap ($\Delta\epsilon_{es}$), in CHCl₃ solution calculated with different density functional at excited state.

Band gaps illustrated in Figure 4.14 are obtained via Koopman's Theorem. The ionization potential obtained is put minus sign hence, theoretical HOMO is obtained. As discussed from GSOP section, HOMO obtained via Koopman's theorem underestimate and overestimate experimental HOMO energy when density functional with large and small HF exchange are used respectively.

Also, theoretical HOMOs obtained are scattered in greater degree with MAE of 0.676 eV. Based on calculation proceed via Koopman's Theorem, ω B97XD with the largest HF exchange term displayed the largest bad gap as compared than other density functional. This is due to the fact that the HOMO obtained underestimate experimental value by 1.14

eV while LUMO obtained overestimate experimental value by 2.31 eV. Density functional with large HF exchange term, M062X and ω B97XD displayed wide band gaps.

This is because DFT with large HF exchange parameter underestimate experimental HOMO and overestimate experimental LUMO. Both density functional B3LYP and MPW1k yield theoretical HOMO close to experimental value with overestimation of 40 and 16 eV respectively. However, the down side of using these functionals are poor estimation of excited state system. Both density functionals displayed a higher degree of overestimation on LUMO level. B3LYP overestimate LUMO by 0.87 eV while MPW1k overestimate LUMO by 0.9 eV.

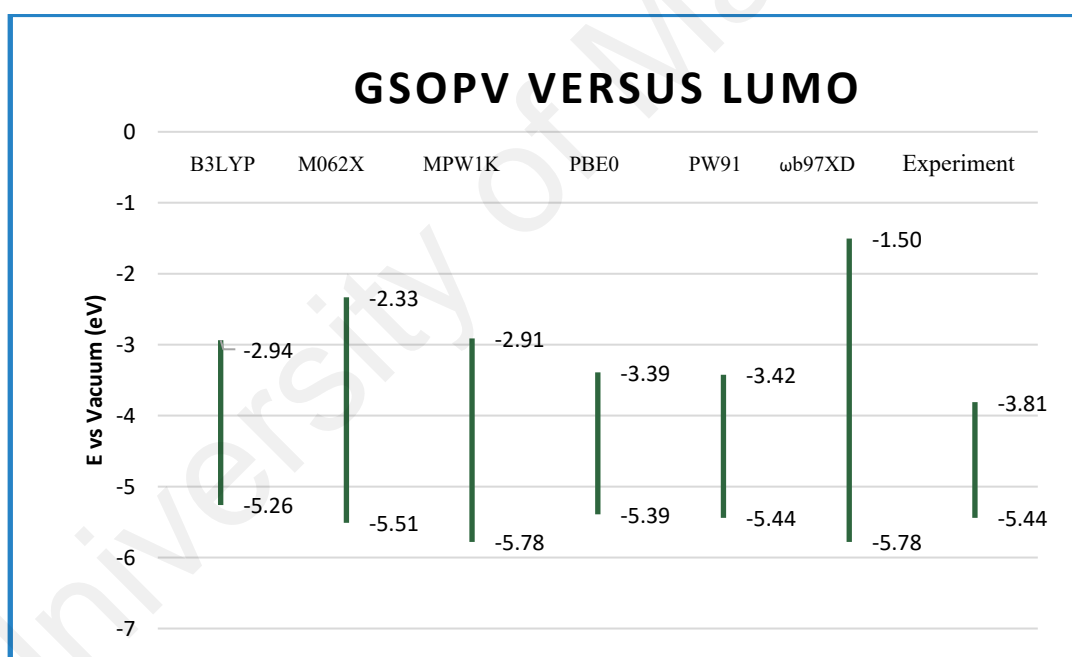


Figure 4.15: SQM1a energies comparison of the HOMOs (ϵ HOMO), the LUMOs (ϵ LUMO), the HOMO–LUMO energy gap ($\Delta\epsilon_{es}$), in CHCl_3 solution calculated with different density functional at excited state.

Based on Figure 4.15, HOMO calculated defined as GSOP_v are more distributed within the range of experimental HOMO. This proves that GSOP_v calculation is necessary to simulate experimental HOMO. Theoretical HOMO obtained via GSOP_v has error distribution of 0.2083 eV.

Due to failure in optimizing SQM1a at excited state, LUMO is obtained via Koopman's Theorem. The true band gap, $\Delta\mathcal{E}_{opt}$ will be less accurate since LUMO obtained is merely an energy that corresponds to electron affinity.

Nevertheless, the assumption of taking the difference between GSOP_v and LUMO, $\Delta\mathcal{E}_{ES}$ is essential for dye construction based on Dewar's rule. One can imagine that the true LUMO will be less in energy than the calculated LUMO due to electron binding energy as discussed above.

Overall, bandgap obtained via $\Delta\mathcal{E}_{fundamental}$ and $\Delta\mathcal{E}_{ES}$ overestimate experimental band gap. This is common since gaussian function is utilized in Gaussian 09W program. Also, molecules being studied in Gaussian 09W program are treated in isolation surrounded by vacuum or solvents defined by dielectric continuum. Hence, the term cluster model is designated for such treatment.

In contrast, a plane-wave-based (PW) algorithm is utilised in Vienna Ab initio Simulation Package, VASP for exact exchange energy calculation. As the number of chromophores increased, number of state commensurate with large amount and saturated as chromophore is spread. As the number of state reach infinity, continuous regularity band of energy levels are generated.

Since the energy levels are in uniform regularity, increasing number of nodes in regular pattern is seen. Take hydrogen for example. Electron in the orbital state treat attractive potential equally for every adjacent atom. Figure 4.16 below illustrate Bloch's theorem explained by single basis s function, namely hydrogen atoms.

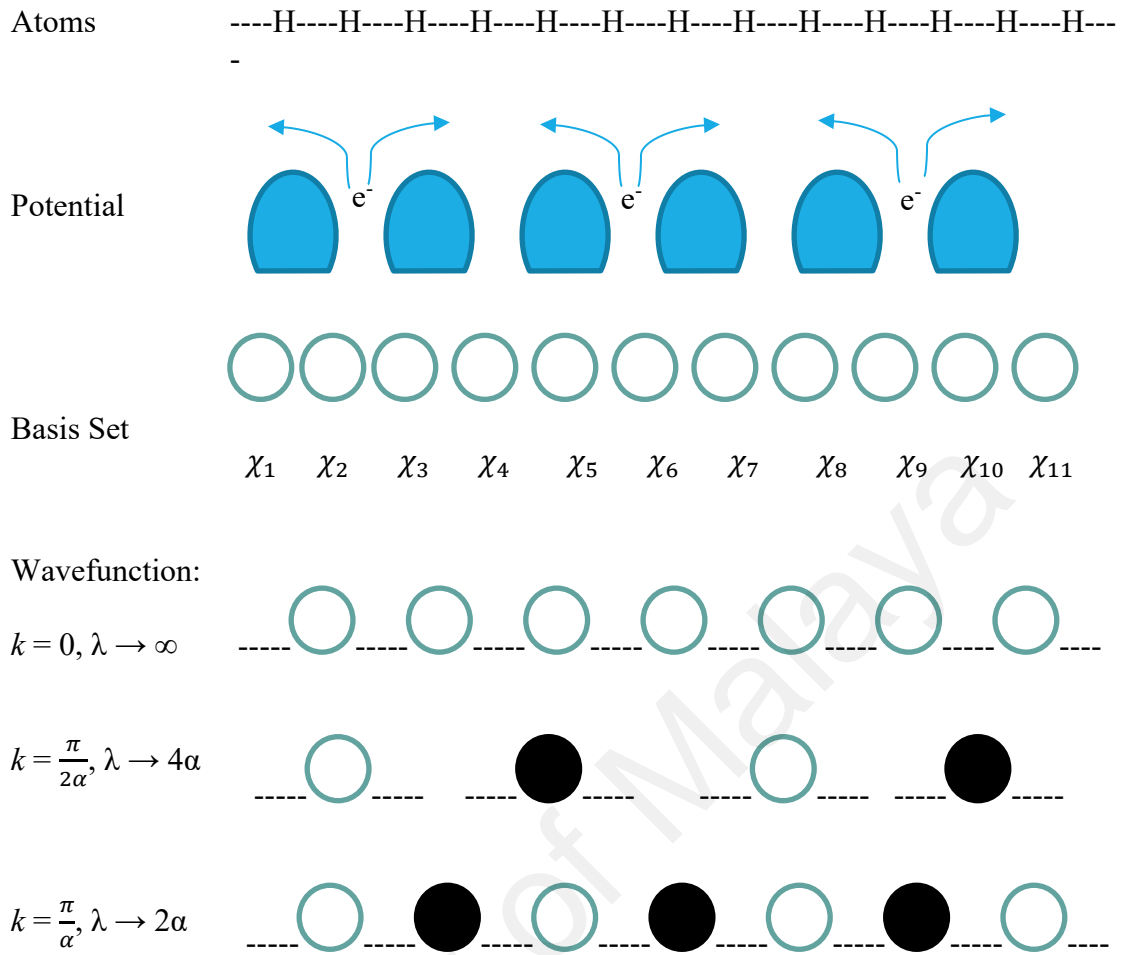


Figure 4.16: Bloch's Theorem Representation Diagram Defining Lattice Constant, α (reproduced from (Bohm, 1949) with permission from Journal of Solid State Physics.

Atoms are arranged in periodic boundary condition. This would mean that total potential energy, $V(x)$ has included the potential energy for each atom and number of lattice constant, α .

$$V(x) = V(x + n\alpha) \quad (4.12)$$

Bloch's theorem states that the periodic wavefunctions is represented by the product of never changing cell part, the 1s hydrogen atom function and cell-periodic part. The periodic part is denoted by k , signifying the wave vector. Basis set is represented by χ . Wave vector k takes the same value as the number of periodic units, N . This can be simplified into:

$$k = \frac{\pi n}{\alpha N} \text{ where by, } n = -\frac{N-1}{2}, -\frac{N-2}{2}, -\frac{N-3}{2}, \dots, -1, 0, 1, \dots, \frac{N-1}{2} \quad (4.13)$$

Below are wavefunction with respect to wave vector, k :

$$k = 0, \lambda \rightarrow \infty. \quad (4.14)$$

Wave function becomes:

$$\Psi^0 = \sum_n e^0 \chi_n^{1s} = \sum_n \chi_n^{1s}, k = \frac{\pi}{2\alpha}, \lambda \rightarrow 4\alpha. \quad (4.15)$$

Wave function becomes:

$$\Psi_{\frac{\pi}{2\alpha}} = \sum_n e^{\frac{i\pi n}{2}} \chi_n^{1s}, k = \frac{\pi}{\alpha}, \lambda \rightarrow 2\alpha. \quad (4.16)$$

Wave function becomes:

$$\Psi_{\frac{\pi}{\alpha}} = \sum_n e^{i\pi n} \chi_n^{1s} = \sum_n (-1)^n \chi_n^{1s} \quad (4.17)$$

In general, wavefunction expressed in wave vector can be written as:

$$\Psi^k = \sum_n e^{ikn\alpha} \chi_n, k \leq \left| \frac{\pi}{\alpha} \right| \quad (4.18)$$

The above equation is known as Bloch's Theorem (Bohm, 1949). Wave vector, k becomes real variable and continuous when n is infinite. This is because k has dimension of 1/length and it is represented within the reciprocal space.

The reciprocal space value of k is known as the first Brillouin Zone. Take note that the $e^{ikn\alpha}$ in Bloch's Theorem is a resemblance of cosine function. The wavelength that is related to $\lambda_k = \frac{2\pi}{k}$ associated with k correspond to the periodic state in the basis function.

For a given energy level, k is associated with momentum of an electron by de Broglie equation. From figure 4.18, each k is treated as degenerate in a way that $E(k) = E(-k)$.

Band structure is defined by the space of endless energy levels in k . In practice, structure treated as coordinate is plotted against $|k|$. The overlapping between periodic cells determine the energy band dispersion.

Notably, the bottom part of the band corresponds to bonding while the top part is the anti-bonding. Figure 4.17 below illustrate energy plotted against periodic phase of a basis function forming band structure diagram.

Based on diagram below, $k = 2\pi/a$ corresponds to the HOMO. Band dispersion depends on overlapping between orbitals. Strong orbital overlap yields big dispersion and the type of overlap dictate bands direction.

Based on Aufbau principle, the size of bonding depends on levels filled by electron. Therefore, electrical properties are associated with band filling. A partial filled band at fermi level correspond to an energy gap. This energy gap is defined as valence band and conduction band.

Valence band (VB) and conduction band (CB) gap are common in semiconductor or insulator material. At zero Kelvin, all VB are filled with electrons and no electrons are filled at CB. At this point, the Fermi energy is located at the middle of the band gap energy. For a pure semiconductor at room temperature, electrons can jump from VB to CB but in low amount.

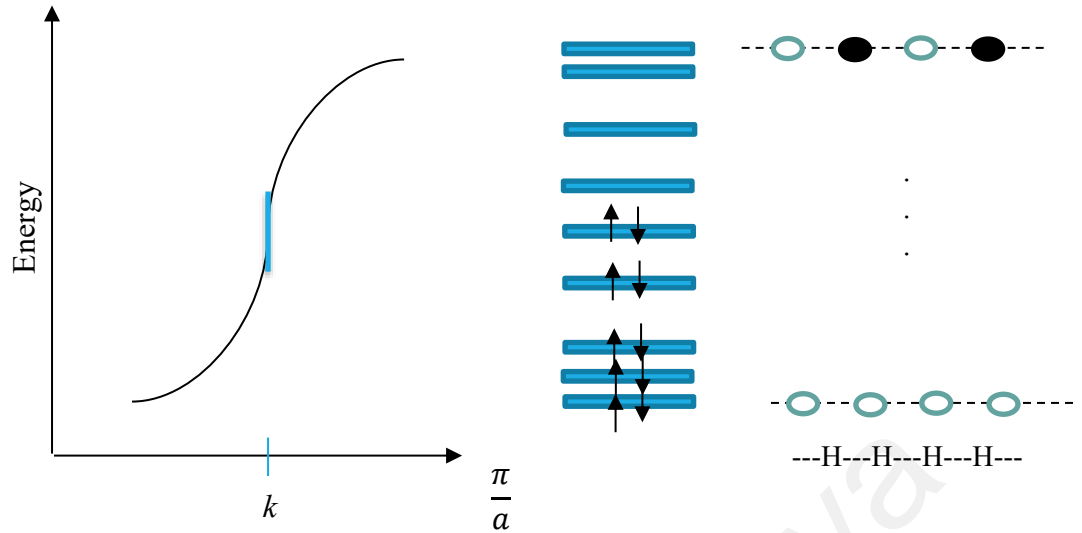


Figure 4.17: Band structure diagram.

Now, the Fermi energy moves toward the edge of CB and is no longer at the middle. Unlike metallic materials, the VB and CB touch each other. Thus, no energy gap in between them. For this kind of materials in zero Kelvin, electrons fill the energy levels from the lowest energy up to a maximum. This maximum energy level is called Fermi energy.

Utilising Bloch's Theorem, the Kohn-Sham equation can be written:

$$\left[-\frac{1}{2}(\nabla + ik)^2 + v_{Coulomb}(\mathbf{r}) + v_{xc}(\rho(\mathbf{r}')) \right] \chi_i^k = \epsilon_i^k \chi_i^k \quad (4.19)$$

The first term corresponds to potential and kinetic energy, taking the form of Hamiltonian operator, followed by coulombic interaction, $v_{Coulomb}(\mathbf{r})$. Vector k are located inside the first Brillouin zone.

Also, the periodicity of Bravais lattice, $v(\mathbf{r})$ are covered by potential terms throughout translation Bravais lattice vector, \mathbf{R} where by $v(\mathbf{r}) = v(\mathbf{r} + \mathbf{R})$. Energy levels are denoted as i . Exchange energy term is expressed as $v_{xc}(\rho(\mathbf{r}'))$ for a Bravais lattice.

Bloch's Theorem states that one electron wave function must form the following term as a consequence of affecting the periodicity of a material:

$$\Psi_i^k = e^{ik \cdot r} \chi_i^k(\mathbf{r}) \quad (4.20)$$

Thus, from the above equation, plane wave is used to express eigenstates Ψ_i to get periodic cell,

$$\chi_i^k : \chi_i^k = \chi_i^k(\mathbf{r} + \mathbf{R}) \quad (4.21)$$

Total energy is obtained from the band structure, e_i^k and wavefunction within periodic cell, χ_i^k . Both e_i^k and χ_i^k can be obtained when all orbitals i in Schrodinger equation is solved together with the possibility of having infinite value for k . However, the size of basis set can be controlled by VASP with cut-off feature. An efficient calculation would depend on the ability to screen potential term in both real and reciprocal space.

Hence, individual plane waves are not suitable for a basis function. They must end up with large plane wave matrices (PW x PW) for diagonalization in order to obtain matrix coefficient.

When dealing with DFT band gap, one must take note that the energy of N+1, N and N-1 electron systems (the Delta SCF method) yield different band gap when calculate as opposed to just calculating the HOMO-LUMO Kohn-Sham states alone.

Delta SCF method cannot be performed in a PW basis because unit cell in a periodic simulation has no charge. In most studies, literature value reported from VASP is merely the difference between Kohn-Sham eigenvalue. Therefore, GSOP cannot be calculated in VASP.

Table 4.9: Band Gap From HOMO-LUMO, $\Delta\mathcal{E}_{fundamental}$ and GSOP_v-LUMO, $\Delta\mathcal{E}_{ES}$ Calculation.

Density	Exp	PW91	B3LYP	PBE0	MPW1K	M062X	ω B97XD
Functional / Molecule	HOMO-LUMO band gap, $\Delta\mathcal{E}_{fundamental}$ (eV)						
SQM1a	1.63	1.20	2.10	1.19	2.37	3.63	5.08
	GSOP _v -LUMO band gap, $\Delta\mathcal{E}_{ES}$ (eV)						
SQM1a	1.63	2.02	2.94	2.00	2.87	3.18	4.28

Discrepancy arose due to the fact that the true, exact Kohn-Sham exchange-correlation functional is dependent on the changes on the electron and electron number. Derivative discontinuity refers to the total electron count that passes through each integer, i . Furthermore, self-interaction error which arises in the occupied states in DFT, and in the unoccupied states in HF term made band-gap calculation more complicated.

Semi-local DFT is a spurious self-interaction in the occupied states if one considers the true band structure calculation. Thus, energy is forced up and able to reduce band gap differences. Similarly, HF forced up energy in the unoccupied states thus, increasing the band gap energy.

From Table 4.9, PBE0 density functional gives the closest band gap difference towards experimental value. Also, PBE0 is seen performing well when in Figure 4.15 This is because the density functional and Fock operator mix ideally (75% DFT and 25% HF term). The self-interaction error in the top part of occupied band and the lower part of unoccupied band are treated approximately equal. Thus, a better assessment on theoretical prediction since band gap are made close to experiment value.

Theoretical and experimental band gaps are tabulated in Table 4.9. Difference between calculated HOMO and LUMO corresponds to fundamental band gap, $\Delta\mathcal{E}_{fundamental}$. From previous chapter, $\Delta\mathcal{E}_{fundamental}$ is defined as the difference between ionization potential and electron affinity of a compound.

Based on Table 4.9, smallest $\Delta\mathcal{E}_{fundamental}$ is acquired by PW91, underestimate experimental value by 0.434 eV. Second best $\Delta\mathcal{E}_{fundamental}$ close to experimental value is obtained by PBE0, underestimate experimental value by 0.436 eV.

However, whilst the PBE0 is a good band gap predictor, other properties obtained are unreliable compared to other density functional. B3LYP are made good for bond length and angle predictor. Thus, optimizing a geometry using B3LYP to locate the true minimum would be ideal.

Introducing a modest Hubbard U term and perform DFT + U calculation is an alternative for DFT self-interaction correction for localized d-block and f-block elements (Hubbard, 1963). A potential is introduced in the Hubbard U which localizes states at which it is applied. In other word, Kohn-Sham DFT are being re-localised and energy is lowered because Hubbard U term possessed a derivative discontinuity. However, this research focuses mainly on organic compound as DSSC and DFT + U will not be covered here.

Based on table 10, HOMO-LUMO gap, $\Delta\mathcal{E}_{fundamental}$ obtained from PW91 and PBE0 underestimate experimental band gap by 0.43 and 0.44 eV respectively. On the contrary, other density functional overestimate $\Delta\mathcal{E}_{fundamental}$ in greater degree.

One can deduce that both PW91 and PBE0 has loose treatment on the exchange energy. All GSOP_v – LUMO, $\Delta\mathcal{E}_{ES}$ overestimate experimental with PBE0 showed the lowest theoretical band gap followed by PW91 (Perdew, 1985).

4.4 Ultraviolet-Visible Spectrophotometer (UV-Vis)

In order to assess the band gap and lowest wavelength for excitation, experimental and theoretical UV-VIS are illustrated in Figure 4.18 below. Experimental spectrum obtained is normalized from each spectra obtained from the literature, namely SMQ1a, SQM1b and MSQ (Maeda et al., 2013). This means that all the spectrum from each material are taken and divided by the peak absorbance so that the optical density is at one.

Simulated absorbance spectra are represented by a unitless quantity, oscillator strength. The oscillator strength, f , corresponds to the strength of electronic transition as explained in previous chapter. From Figure 4.18, all theoretical spectra overestimate experimental spectrum. This is foreseen as Gaussian 09W package employed gaussian function for all calculations.

The closest oscillator strength towards optical density is obtained by M062X. However, wavelength at which it excites should be taken into consideration. Although M062X displayed the closest value to optical density of SQM1a, the wavelength at which it excites is far from experimental value. Spectral properties such as maximum absorption energy (cm^{-1}), maximum absorption wavelengths, λ oscillator strength, f and major transition of intense peak of SQM1a are collected based on TD-DFT calculation employing different density functional.

Based on the experimental value, SQM1a excite at 707 nm with maximum absorbance of 0.885 cm^{-1} . Density functional M062X excites at 616.4 nm with an oscillator strength, f of 1.4448. Theoretical value far from experimental value. PBE0 spectrum excites at 715 nm, giving it the closest excited wavelength to experimental value. Also, an oscillator strength of 0.9476 is exhibited for PBE0, a value close to experimental spectrum.

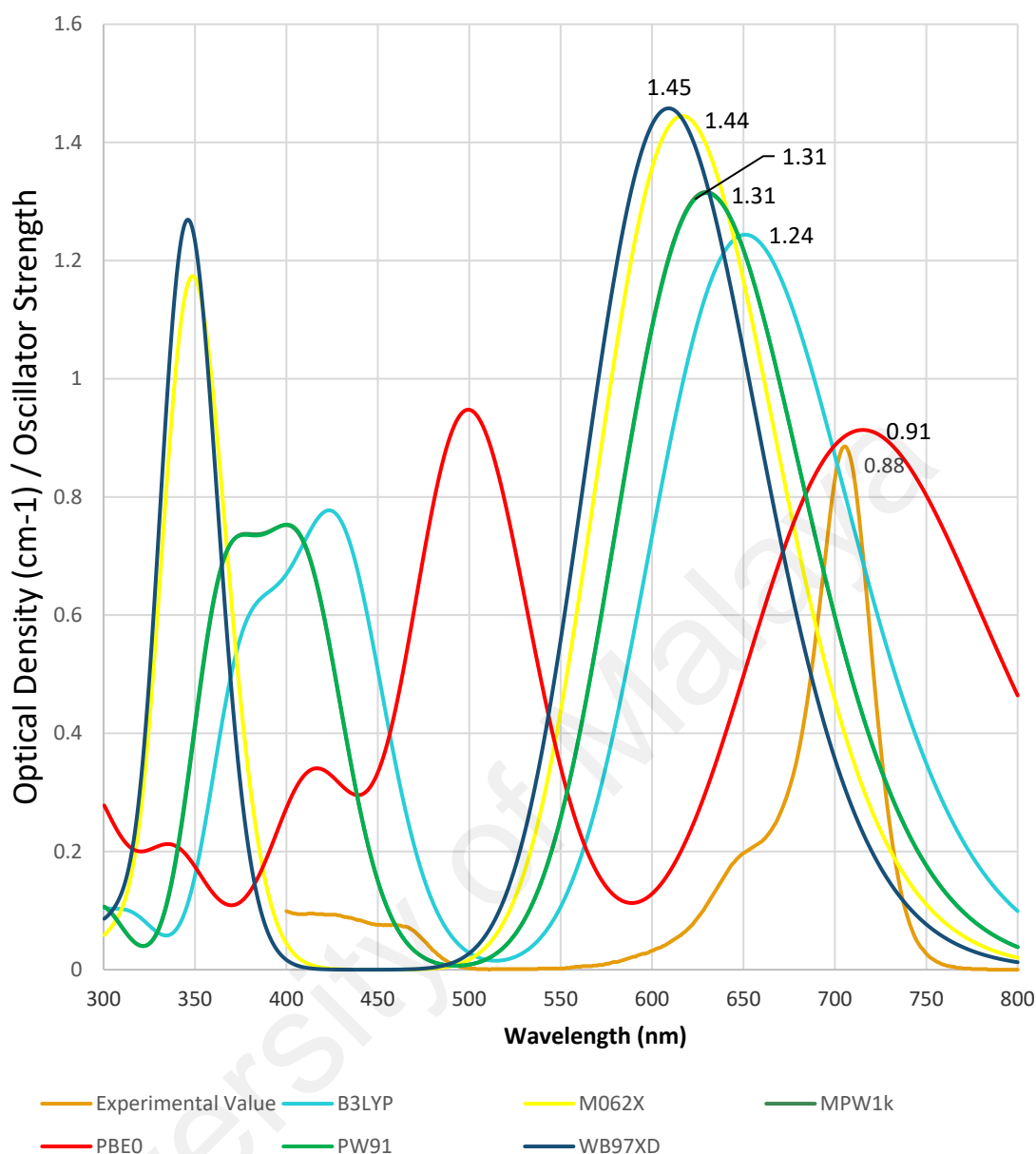


Figure 4.18: Experimental and simulated UV-VIS graph for SQM1a using different Density Functionals.

As expected, ω B97XD with the biggest HF exchange term displayed the biggest oscillator strength. Spectra obtained through PW91 and MPW1k functionals displayed the same trend thus, forming a graph on top of one another. The simulated spectra of SQM1a in chloroform obtained range from 599 to 638 nm. All spectra obtained have successfully predicted major transition from HOMO to LUMO as seen in table below.

Table 4.10: Calculated Excited State Energy (nm), Oscillator Strength and Transition Configuration of SQM1a by TD-DFT Employing Different Density Functional.

Density Functional	Energy (cm ⁻¹)	λ (nm)	f	Major Transition
PW91	15886.7	629.5	1.3144	HOMO->LUMO (99%)
B3LYP	15365.7	637.5	1.2438	HOMO->LUMO (99%)
PBE0	13982.4	715.2	0.9476	HOMO->LUMO (96%)
MPW1K	15890.7	629.3	1.3161	HOMO->LUMO (99%)
M062X	16223.0	616.4	1.4448	HOMO->LUMO (98%)
ω 97XD	16426.3	608.8	1.4577	HOMO->LUMO (96%)

In contrast, M062X with relatively large HF exchange term displayed much lower oscillator strength. This can be explained in terms of dipole strength obtained.

Oscillator strength are evaluated in two ways, they are the velocity form and dipole form. In atomic unit, oscillator strength is expressed as follow:

Dipole form,

$$f^r = \left| \frac{2\omega}{3} \langle \Psi_{ground} | \hat{\mu} | \Psi_{excited} \rangle \right|^2 \quad (4.22)$$

And velocity form,

$$f^v = \left| \frac{2}{3\omega} \langle \Psi_{ground} | \hat{v} | \Psi_{excited} \rangle \right|^2 \quad (4.23)$$

In which transition excitation energy is denoted as ω . The two equations in bracket are the electric dipole transition moment and velocity transition moments respectively.

They are operated on the ground and excited state wavefunctions. TD-DFT calculation proceeded via M062X and ω B97XD possessed dipole moment of 3.14561 and 2.1391 Debye respectively.

At ground state, single point calculation obtained from optimized B3LYP geometry using M062X and ω B97XD exhibit 1.8649 and 2.0084 Debye. Therefore, the bigger the differences for total dipole moment obtained between ground state and excited state, the smaller is the oscillator strength exhibited.

Simulated UV-Vis spectrum obtained by Gaussian 09W is merely an overlapped Gaussian shape line for each excited transition of a molecule. This makes way for f to be proportional to the relative height of each peak. Modelling an electronic spectrum can be achieved by Frank-Condon analysis.

This is done by taking vibrational energy levels for both ground and excited state into consideration at different basis sets. Due to time restriction, only one basis set is used and different density functionals are employed instead.

Density functional PW91, B3LYP, PBE0 and MPW1k showed 99% major transition peak. On the contrary, density with large HF exchange term has very small minor contribution to maximum peak.

M062X and ω B97XD both have HOMO to LUMO transition contribution of 98% and 96%. Calculation for major transition can be done by taking the probability density in the output file generated by Gaussian 09W.

The output line generated from TD-DFT employing M062X with 6-31+G(d) is displayed as:

Excited State 1: Singlet-A 2.0704eV 598.86nm f=1.0657 <S**2>=0.000

170 ->172 -0.10201
 171 ->172 0.69736
 171 <-172 -0.01012

This can be interpreted in figure below:

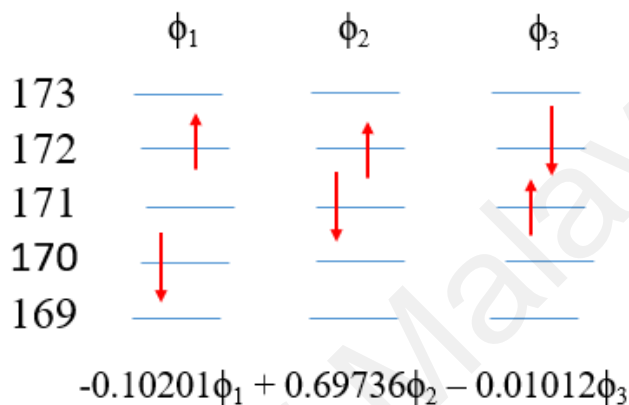


Figure 4.19: Molecular Orbital editor displayed in Gaussview.

Based on the given value, probability density can be extracted out by the following equation:

$$C^2 = \frac{1}{2} \tag{4.24}$$

Where C is the probability density expressed in decimal. One has to multiply 100 to convert decimal into percentage form. Hence, the probability density obtained by ωB97XD is as follow:

$$\phi_1 = (-0.07348)^2 \times 2 = 0.0108 \approx 1.08 \%$$

$$\phi_2 = 0.70000^2 \times 2 = 0.98 \approx 98\%$$

$$\Phi_3 = (-0.01012)^2 \times 2 = 0.0002 \approx 0.02\% \tag{4.25}$$

4.5 Structural Design by Dewar's Rule

Table 4.11: Optimized Three-Dimensional Structure for SQM1a and New Dyes. Carbon is represented by grey Ball, Oxygen by red Ball and Nitrogen by Blue Ball.

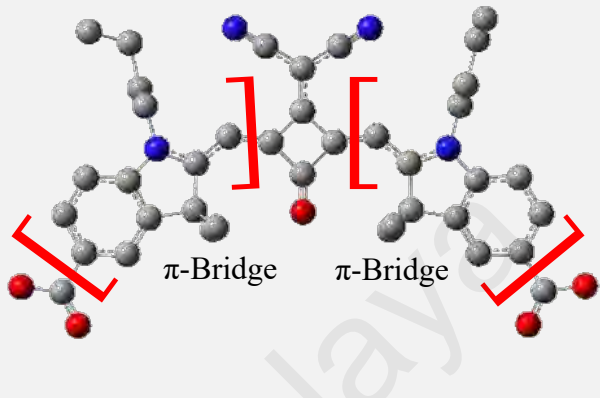
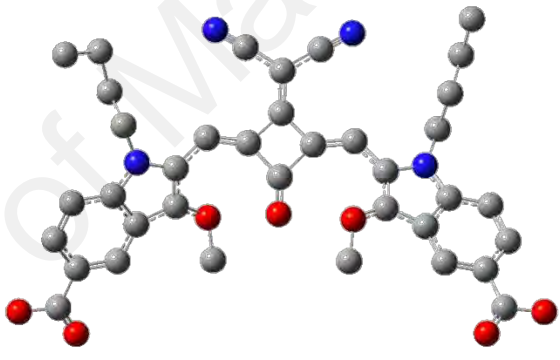
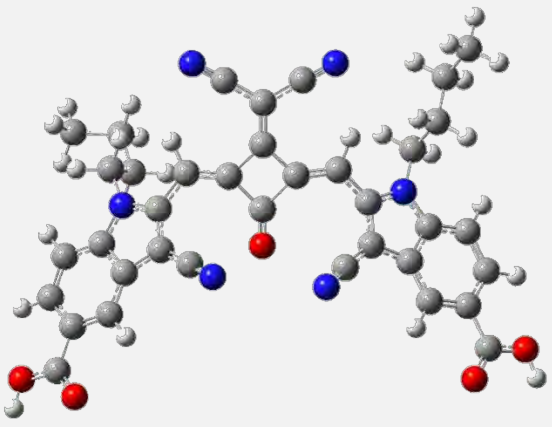
Name	Atoms	Substituent	3-D Structural Representation
<i>SQM1a</i>	-	-	
<i>ED2</i>	- OCH ₃	Electron Donating	
<i>EW2</i>	-CN	Electron Withdrawing	

Table 4.11, continued.

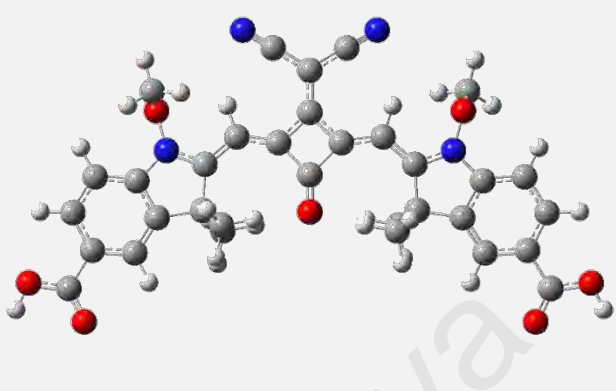
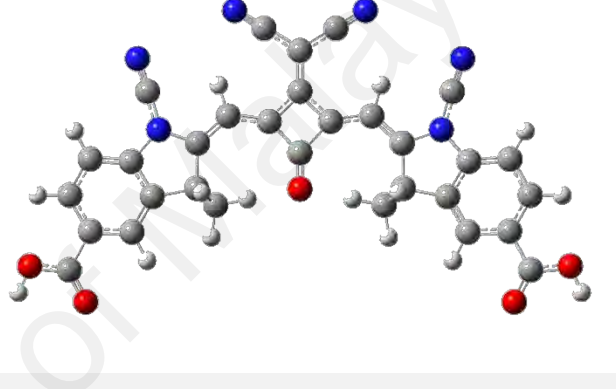
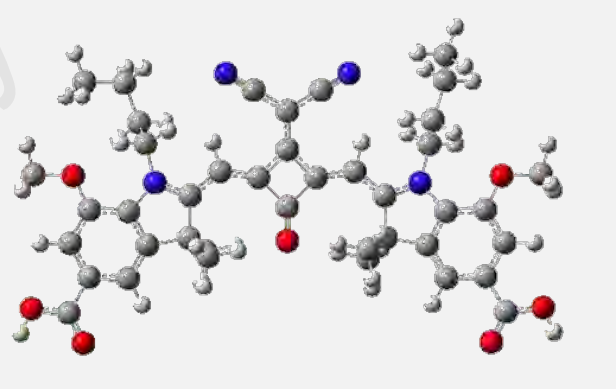
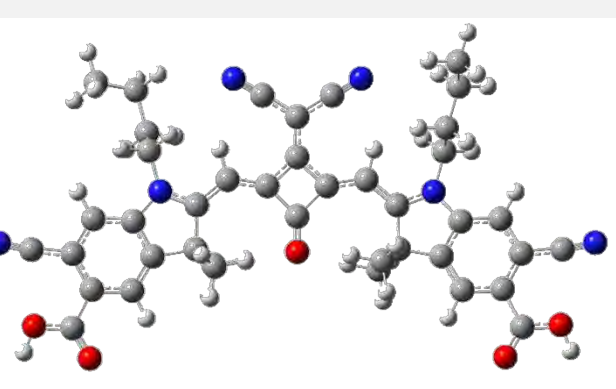
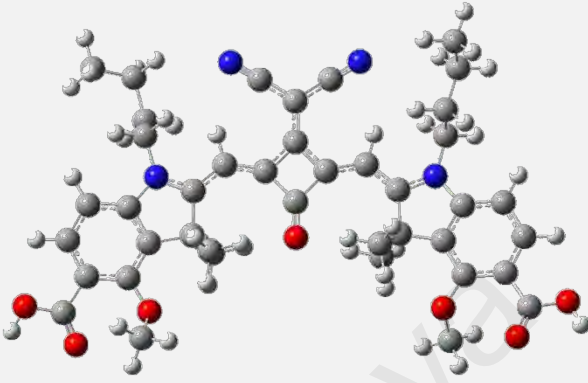
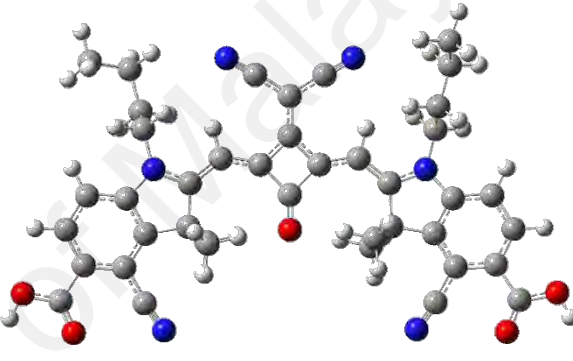
<i>Name</i>	<i>Atoms</i>	<i>Substituent</i>	<i>3-D Structural Representation</i>
<i>ED3</i>	- OCH ₃	Electron Donating	
<i>EW3</i>	-CN	Electron Withdrawing	
<i>ED4</i>	- OCH ₃	Electron Donating	
<i>EW4</i>	-CN	Electron Withdrawing	

Table 4.11, continued.

<i>Name</i>	<i>Atoms</i>	<i>Substituent</i>	<i>3-D Structural Representation</i>
<i>ED5</i>	-OCH ₃	Electron Donating	
<i>EW5</i>	-CN	Electron Withdrawing	

Signifying electron from electron withdrawing group being excited from 171 (HOMO) to 172 (LUMO) with 98% contribution while 1.08 and 0.02% electron move from 170 (HOMO-1) to 172 (LUMO) and 172 (LUMO) to 171 (HOMO) respectively. Least energy is required to excite electron from occupied orbital to unoccupied orbital (virtual). Hence, HOMO-LUMO gap require small energy and therefore remain the most likely transition for excited state system. New dyes are produced and their 3-dimensional structures are illustrated in Table 4.11. The starred position of a π -linkage belongs the closest carbon towards D-group. Methoxy substituent is used as ED group. ED1 is supposedly be attached to the first starred position, closest carbon towards D-group. However, methoxy group attached to the mentioned carbon affect the electronegativity of D-group. Also, cyanide substituent is supposedly be attached on the same ED1 carbon forming EW1.

This would provide comparative study on HOMO energy shift. However, a cyanide substituent will form a ring with D-group. Ultimately, D-group is enlarged and thus, affect the D- π -A configuration. Once the π -linkage is not neutral, Coulson-Rushbrooke Longuet-Higgins cannot be used since D-group has net charge distribution. All unstarred position in π -linkage (closest to D-group) is left empty. This is because theoretical ESOP cannot be obtained and dye optimization in excited state is impossible for SQM1a. Therefore, only substituent on starred position is considered in this study. Next, methoxy substituent is attached onto second starred position, giving rise to ED2 compound.

Cyanide is chosen as EW group. Hence, second starred position is bonded with EW group denoted as EW2. Third starred position is attached with ED and EW group, giving rise to ED3 and EW3 respectively. Same sequence is done for the 4th position. On the contrary, ED5 construction on the 5th carbon starred position is not possible as it will form dimer with carboxy group thus, affecting the A-group. Therefore, ED5 and EW6 are built on 6th starred position. Since B3LYP displayed the best MAE with experimental data, all new dyes are optimized in vacuum using B3LYP/6-31G (d) together with frequency calculation in order to detect imaginary frequency. No imaginary frequency is found indicating that all new dyes are optimized at true ground state. Optimized EW2 does not form planar structure as the π -linkage is seen to be twisted as a result of steric effect.

Steric effect altered the π -linkage of EW2 in great degree and therefore, is not suitable to be used as dye sensitizer in DSSC. For an organic dye sensitizer to be applied onto DSSC, a planar π -linkage is adopted in order to inject electron efficiently onto TiO₂ (Mishra et al., 2009). However, results obtained in EW2 used in order to assess theoretical HOMO. Unlike EW1 and ED5, they are not included in calculation because they do not form π -linkage any longer. Instead EW1 and ED 5 will form a new D-group and A-group respectively.

Table 4.12: Selected π -Bridge Length (L_π), Bond Length, Bond Angle, Dihedral Angle and Dipole Moments for SQM1a and New Dyes.

	SQM1a	ED2	EW2	ED3	EW3	ED4	EW4	ED5	EW5
L_π (Å)	6.07997	6.02474	6.02853	6.05530	6.05189	6.04180	6.05869	6.06164	6.06609
C ₂ -C ₈ (Å)	1.39948	1.36176	1.34926	1.39523	1.40375	1.39433	1.39620	1.39542	1.39606
C-N- L_π (°)	-	-	177.465	-	178.998	-	174.247	-	173.946
CH ₃ -O- L_π (°)	-	118.342	-	110.598	-	117.760	-	118.363	-
C ₈ - C ₉ -C ₁₄ - C ₁₇ (°)	177.563	171.829	-173.834	-177.401	-179.984	170.395	174.112	174.763	174.246
C ₃₅ -C ₄ - C ₂ - C ₁₉ (°)	-2.140	-28.440	2.990	13.919	-0.002	-17.986	-13.136	-15.140	-12.073
Local Minimum Energy (eV)	- 57289.90	- 59186.85	-57975.61	-54940.03	-53730.06	-63496.92	-62285.17	-63496.63	-62285.22

4.6 Ground State Dye Evaluation Based on Dewar's Rule

Since SQM1a is a symmetrical squaraine dye, it comprises 2 sets of π -bridge linkage because they have 2 sets of A-group. They both have the same length as proven in table 2. Hence, only 1 set of π -bridge linkage is taken for length comparison. B3LYP/6-31G(d) model has shown a good agreement with experimental value.

Molecular properties that are essential in evaluating the local minimum of SQM1a are listed in Table 4.12. Length between C (8) and C (17) is taken as the length of π -bridge linkage (L_π). Dihedral of alkyl chain C8- C9- C14- C17 defined the planarity of the π -bridge linkage. Planarity of dye is represented by the dihedral of alkyl chain C19- C2- C4- C35. Insertion of ED or EW do not affect the energy loss as results of photoisomerization. This is because SQM1a as stated previously, is locked by the bulkiness of D-group. Therefore, the shrinking or expansion of L_π do not affect the overall dye performance. However, evaluation of L_π is still necessary in order to assess the local minimum on PES.

All new dyes have L_π that are shorten when ED or EW is substituted into π -bridge linkage. The L_π for EW5 is shorten by 0.014 Å from SQM1a and it is calculated to be 6.066 Å. Also, EW5 displayed the longest L_π among other new dyes. In contrast, ED2 exhibit the shortest L_π . As a result of L_π shrinking, the A-group in ED2 is twisted forming a dihedral angle of 171.8° for C8-C9-C14-C 17. The biggest L_π dihedral angle deviation from SQM1a is seen in ED4. It can also be seen that ED4 formed the second shortest L_π . Not all ED group shorten the L_π since ED3 displayed a relatively longer L_π than ED2, EW2, and EW3. Furthermore, ED3 exhibit the least L_π dihedral deviation from SQM1a. Therefore, ED3 retain the planarity of π -bridge linkage.

Despite the planarity of π -bridge linkage retained by ED3, optimization for this dye exhibits the highest local minimum compared to other new dyes. -54940.03 eV is seen for ED3 local minimum whereas -53730.06 eV is obtained for optimized EW3. In short, substitution of substituent at 3rd starred position increases local minimum energy on the PES. Local minimum is brought down when substituent is inserted at 4th and 5th starred position. Dye conformation planarity is altered when 2nd, 4th and 5th starred positions are inserted with substituent. A twisted geometry is formed for optimized ED2. On the other hand, bent structure is obtained for optimized EW2. See saw conformations are exhibited for ED3, ED4, EW4, ED5 and EW5. SQM1a itself adapt the see saw conformation with dihedral angle of -2.140 for C35-C4- C2-C19. Planar dye is seen in EW3, thus indicating a good π -conjugation between D- π -A group.

4.7 Excited State Dye Evaluation

TD-DFT is performed on all dyes in order to evaluate the UV-Vis shift. As seen in previous excited state evaluation, PBE0 performed as the best density functional when single point calculation is employed. Therefore, single point energy calculation is done at excited state employing PBE0/6-31+G(d) using TD-DFT. Solvent effect is taken into consideration as dielectric constant of chloroform must be included to mimic experimental UV-Vis.

In order to screen new dyes as the best candidate for sensitization onto TiO₂, frontier molecular orbital for reference dye (SQM1a) and new dyes are displayed in Table 4.13. For a good electron distribution, electron should flow from D-group to π -bridge linkage before residing on A-group. Once at A-group, electron is injected into TiO₂ nanocluster. All new dyes showed good electron overlap between HOMO-LUMO except for EW2 and EW3.

Table 4.13: Frontier Molecular Orbital for SQM1a and New Dyes Obtained via Single Point Calculation Employing PBE0/6-31+G(d) at Excited State by TD-DFT.

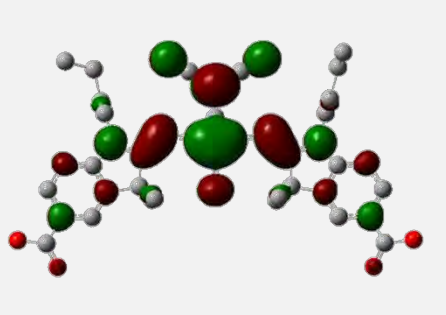
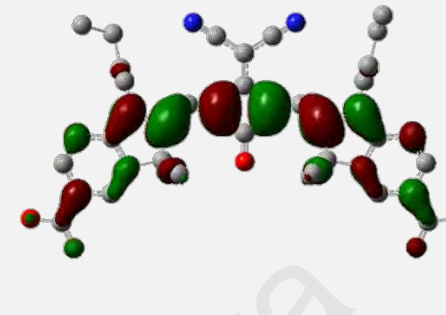
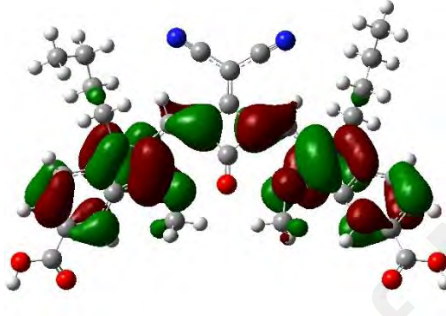
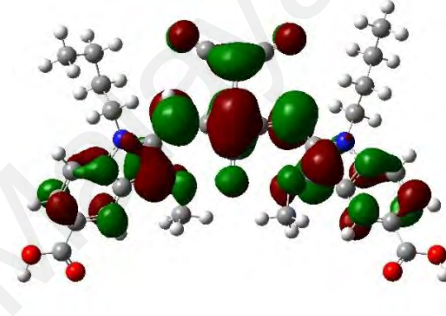
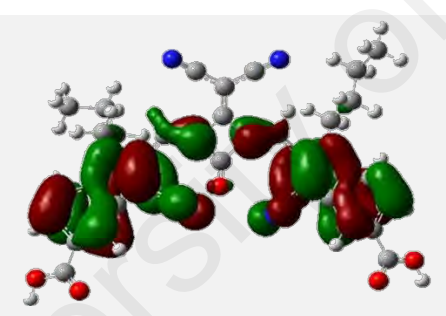
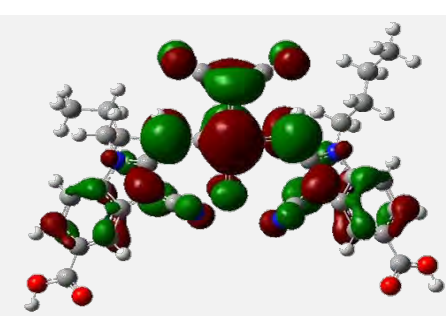
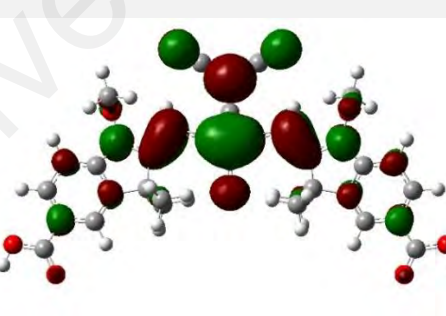
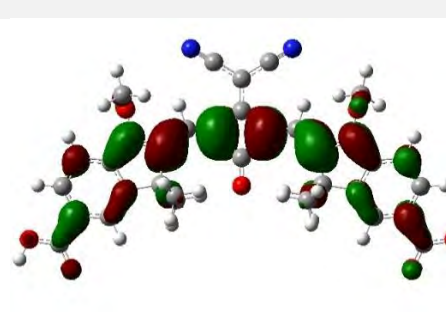
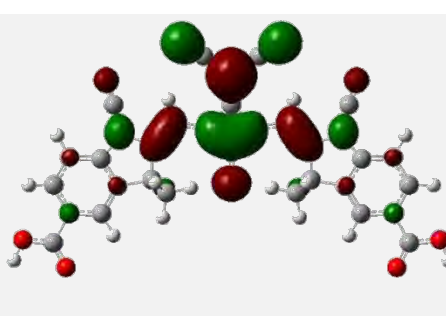
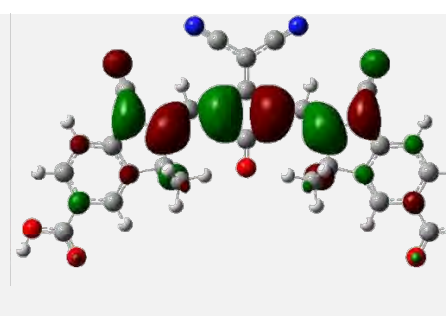
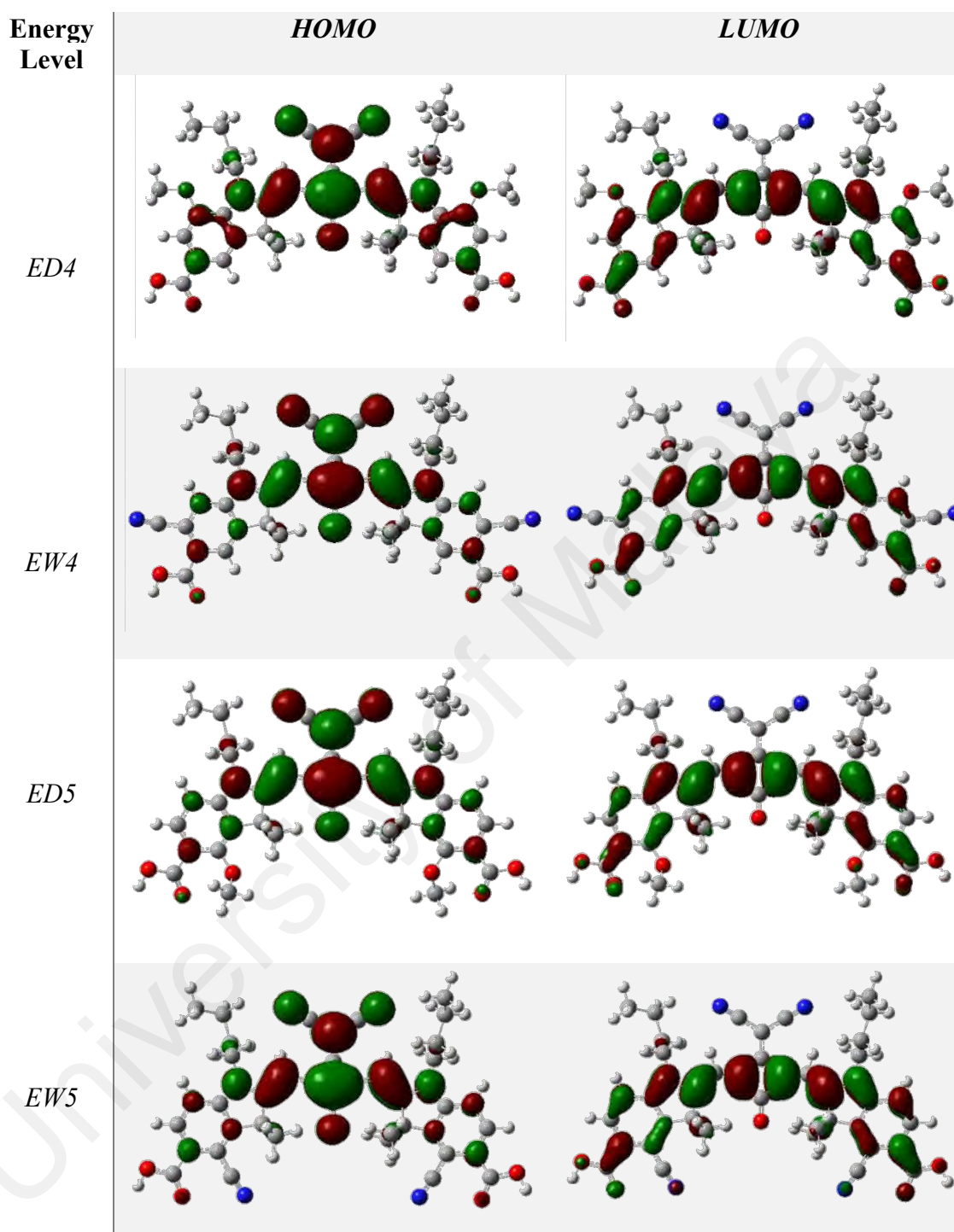
Energy Level	HOMO	LUMO
<i>SQM1a</i>		
<i>ED2</i>		
<i>EW2</i>		
<i>ED3</i>		
<i>EW3</i>		

Table 4.13, continued.



Despite having planar conformation, excited electron remains at D-group for EW3. Hence, electron will not be injected into TiO₂ nanocluster instead, quenched and reside on neighboring molecule. For the case of EW4 and EW5, LUMO are dominated at π -bridge linkage.

Only small portion of electron flow to A-group. Thus, weaken electron coupling with nanocluster surface. On the contrary, LUMO populate the entire π -bridge linkage and A-group when ED group is on starred position. HOMO is dominated by D-group and π -bridge linkage, signifying a good HOMO-LUMO overlap and electron distribution over the entire dye.

The HOMO for ED3, ED4 and ED5 are distributed over the dicyanovinylene group. Their LUMO delocalized over the entire indolenine component bearing the anchoring carboxylic unit. Panchromatic performances for these dyes are promising due to the clear unidirectional electron flow from the D-group to A-group.

An exception to the above phenomena is seen for ED2. This is due to the twisted conformation adapted at local minimum. The chromophore is said to be broken and no longer exhibit D- π -A character. The enhanced molecular charge distribution for ED3-ED5 are attributed to the planarity of the dyes. This type of distribution further provide evidence to Dewar's rule, with every ED group on starred position exhibit an increased in HOMO energy level.

Therefore, one can deduce the HOMO energy obtained for new dyes. HOMO-LUMO energy levels are displayed in Figure 4.20. SQM1a is chosen as the benchmark in order to evaluate the HOMO-LUMO energy change. Elevation in HOMO energy level for ED4 and ED5 are seen in agreement with Dewar's rule.

Substitution of ED group onto starred position therefore, resulted in an increased in HOMO energy provided that the D- π -A character is retained. A different case is seen for ED2 since twisted geometry is adapted. A non-planar chromophore resulted in loss of D- π -A character. Thus, a decreased in HOMO energy is exhibited which broaden the band gap.

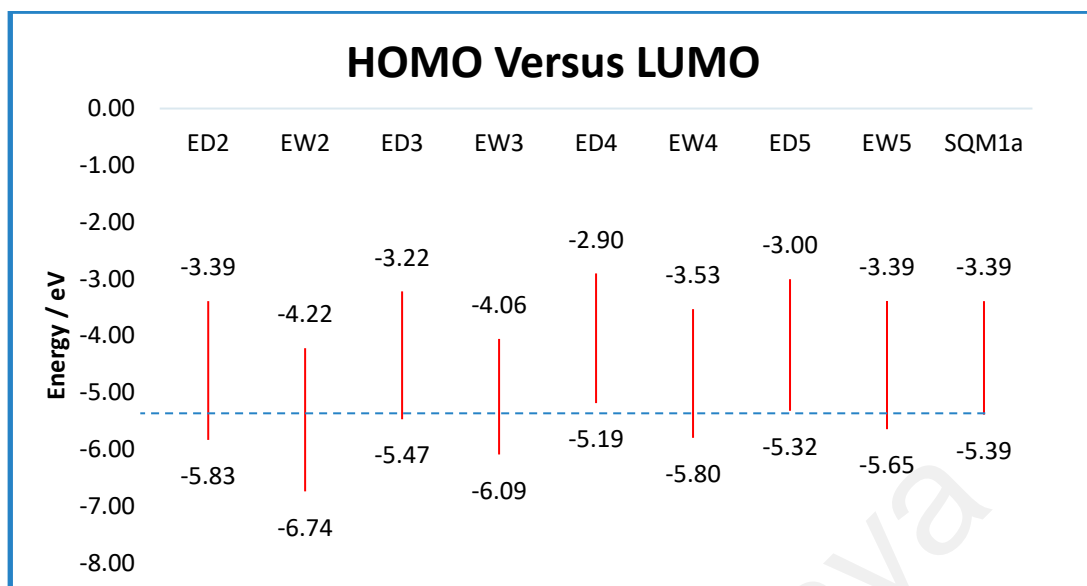


Figure 4.20: HOMO–LUMO energy gap ($\Delta\epsilon_{es}$) Energies Comparison for SQM1a and New Dyes by TD-DFT.

A deviation from the projected trend is exhibited for ED3. Slight decrease in HOMO energy is seen. This is due to the fact that ED group is attached onto nitrogen atom instead of carbon atom. Hence, Dewar's rule does not apply for this case.

The electron affinity for methoxy group decrease due to the fact that nitrogen is more electron negative than carbon. Hence, the strength of methoxy as ED group decreased significantly. In contrast, methoxy is attached to starred carbon for ED4 and ED5. HOMO energy is elevated.

All new dyes based on EW substituent displayed lower HOMO energy than SQM1a. A systematic trend is seen when EW is attached to starred position. For EW2-EW5, HOMO energy is brought down, lower than SQM1a. The biggest drop in HOMO energy is seen in EW2. For a twisted geometry, ED group is attached on starred position thus, HOMO energy decreases significantly.

Table 4.14: Calculated Excited State Energy (nm), Oscillator Strength and Transition Configuration of SQM1a and New Dyes by TD-DFT via Single Point Calculation Employing PBE0/6-31+G(d) at Excited State.

Dye	λ (nm)	f	Major Transition	Minor Transition
SQM1a	706.00	0.885	HOMO->LUMO (100%)	-
ED2	606.96	0.753	HOMO->LUMO (100%)	-
EW2	616.84	0.3105	HOMO->LUMO (97%)	H-1->LUMO (3%)
ED3	649.34	0.6577	HOMO->LUMO (97%)	H-1->LUMO (3%)
EW3	794.41	0.261	HOMO->LUMO (96%)	H-1->LUMO (5%)
ED4	631.12	0.9138	HOMO->LUMO (98%)	H-1->LUMO (2%)
EW4	647.61	0.7452	HOMO->LUMO (97%)	H-1->LUMO (3%)
ED5	626.88	0.7762	HOMO->LUMO (98%)	H-1->LUMO (2%)
EW5	649.44	0.7173	HOMO->LUMO (98%)	H-1->LUMO (2%)

All new dyes are excited with HOMO-LUMO electron excitation as major transition. No minor transition is seen for ED2 while other dyes displayed major and minor transition during excitation. All new dyes displayed HOMO-1 to LUMO excitation except for ED2. ED2 displayed and opposite electron flow direction as compared to other new dyes. At HOMO, electrons are localized on the indolenine part of the dye. Upon excitation, electrons are delocalized on the cyclobutene core. Hence, a reversed electron flow from A-group to D-group is seen only for ED2. Also, the twisted geometry for ED2 exhibit different electron excitation compared to other new dyes. Therefore, major transition differs for ED2.

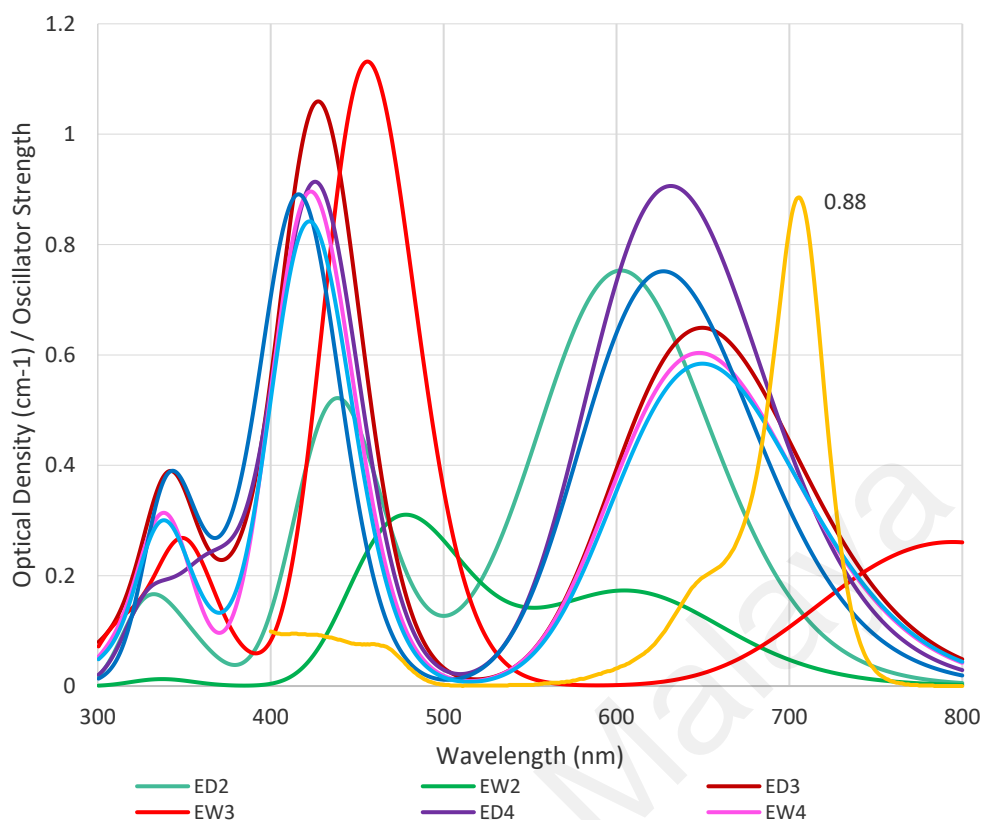


Figure 4.21: Experimental and Simulated UV-VIS Graph for SQM1a and New Dyes Respectively. Single Point Excitation Using TD-DFT at PBE0/6-31+G (d) in Chloroform.

Based on figure 4.21, all new dyes exhibit a band shift from lower energy to higher energy, also known as hypsochromic shift. Shift in band upon excitation is related to molecule substitution series as well as solvent polarity. From the graph obtained, chloroform is used since UV graph for SQM1a is done in chloroform. Thus, dielectric constant should be the same in order to evaluate theoretical UV.

Hypsochromic shift is an undesirable property for DSSC application. Hypsochromic shift correspond to increasing in HOMO-LUMO gap. Only EW3 displayed a bathochromic shift, band shift towards lower energy. However, the oscillator strength is not strong enough, that is 0.261 for a major HOMO-LUMO transition.

CHAPTER 5: CONCLUSION

Location of ground state energy has been successfully described by employing B3LYP density functional. Zero imaginary frequency confirms the optimized structure is at minimum position on the PES. Bond length and angles obtained from B3LYP optimization showed the least mean error as compared to other density functionals.

Best correlation between theoretical HOMO and experimental HOMO is seen for calculation proceeded via GSOP_v. Similar trend in energy level over series of differently structured squaraine is achieved by incorporating 54% HF exchange term employing M062X density functional. Therefore, GSOP_v is the method of choice to benchmark experimental HOMO. Density functional M062X is found to be the most reliable density functional to benchmark HOMO. It can be concluded that the geometry relaxation should be considered after adding and/or removing an electron; i.e. optimization for anion and cation form of M is mandatory indicating that nuclear positions are allowed to be reorganized. However, geometry relaxation in DSSC internal mechanism is not considered when fast electron is injected into TiO₂ semiconductor. This is proven by the performance of GSOP_v method over GSOP_a and HOMO_{cal} method. In other word, nuclear positions are not allowed to be changed and the external potential is kept constant during electron excitation.

Due to failure in optimizing molecule at excited state, an approximation based on Koopman's Theorem to predict LUMO is used. Band Gap is analyzed instead of the LUMO value. PBE0 density functional outperformed all other density functionals in predicting SQM1a band gap.

New dyes are produced based on Dewar's Rule. All new dyes displayed good electron overlap between $\pi \rightarrow \pi^*$ absorption wavelength except for EW2 and EW3. This is because, substitution at unstarred carbon 2 and 3.

Bathochromic shift is obtained from the development of EW3 but with a low oscillator strength. Failure to predict ESOP results in band gap prediction failure. Hence, band gap based on ESOP and GSOP will provide a better band gap correlation with experimental data as compared to LUMO-GSOP band gap (Mariachiara et al., 2012). Potential fabrication of new dye sensitized solar cells can be seen in ED4 and ED5. Synthesis of ED4 and ED5 are made possible through substitution of electron donating group at starred position 4 and 5. Both dyes produced HOMO above experimental value, signifying a closer energy to LUMO. However, failure to predict LUMO causes theoretical LUMO to be above experimental value.

REFERENCES

- Abbotto, A., Barolo, C., Bellotto, L., De Angelis, F., Grätzel, M., Manfredi, N., . . . Nazeeruddin, M. K. (2008). Electron-rich heteroaromatic conjugated bipyridine based ruthenium sensitizer for efficient dye-sensitized solar cells. *Chemical Communications*(42), 5318-5320.
- Adachi, M., & Nakamura, S. (1994). Absorption spectrum shift in the solid state. A MO study of pyrrolopyrrole pigment. *The Journal of Physical Chemistry*, 98(7), 1796-1801.
- Agrawal, S., English, N. J., Thampi, K. R., & MacElroy, J. M. D. (2012). Perspectives on ab initio molecular simulation of excited-state properties of organic dye molecules in dye-sensitized solar cells. *Physical Chemistry Chemical Physics*, 14(35), 12044-12056.
- Ahn, K., Pham-Cong, D., Choi, H. S., Jeong, S.-Y., Cho, J. H., Kim, J., . . . Cho, C.-R. (2016). Bandgap-designed TiO₂/SnO₂ hollow hierarchical nanofibers: Synthesis, properties, and their photocatalytic mechanism. *Current Applied Physics*, 16(3), 251-260.
- Almbladh, C.-O., & von Barth, U. (1985). Exact results for the charge and spin densities, exchange-correlation potentials, and density-functional eigenvalues. *Physical Review B*, 31(6), 3231.
- Bai, Y., Yu, Q., Cai, N., Wang, Y., Zhang, M., & Wang, P. (2011). High-efficiency organic dye-sensitized mesoscopic solar cells with a copper redox shuttle. *Chemical Communications*, 47(15), 4376-4378.
- Bastard, G. (1990). *Wave Mechanics Applied to Semiconductor Heterostructures*.
- Becquerel, A. (1839). Mémoire sur les effets électriques produits sous l'influence des rayons solaires. *Comptes Rendus* 9: 561–567.
- Becquerel, A. E. (1839). Mémoire sur les effets électriques produits sous l'influence des rayons solaires. *Comptes Rendus des Séances Hebdomadaires*, 9, 561-567.
- Bohm, D. (1949). Note on a theorem of Bloch concerning possible causes of superconductivity. *Physical Review*, 75(3), 502.
- Born, M. (1955). Statistical interpretation of quantum mechanics. *Science*, 122(3172), 675-679.
- Boschloo, G., & Hagfeldt, A. (2009). Characteristics of the Iodide/Triiodide Redox Mediator in Dye-Sensitized Solar Cells. *Accounts of Chemical Research*, 42(11), 1819-1826.
- Cann, O. (2016). Citation of World Economic Forum. Retrieved on 24 October 2017 from <https://www.weforum.org/agenda>.

- Charton, M. (2002). *Advances in Quantative Structure-Property Relationships* (Vol. 3): Elsevier.
- Chen, S., Deb, S. K., & Witzke, H. (1978). Dye-titanium dioxide photogalvanic cell. In: Google Patents.
- Chmielewski, A. G. (1999). *Environmental effects of fossil fuel combustion*. Retrieved on 17 August 2017 from <https://inis.iaea.org>.
- Connick, W. B., Geiger, D., & Eisenberg, R. (1999). Excited-state self-quenching reactions of square planar Platinum (II) diimine complexes in room-temperature fluid solution. *Inorganic Chemistry*, 38(14), 3264-3265.
- Coulson, C., & Rushbrooke, G. (1940). *Note on the method of molecular orbitals*. Paper presented at the Mathematical Proceedings of the Cambridge Philosophical Society.
- Das, S., Thomas, K. G., Thomas, K., Kamat, P. V., & George, M. (1994). Photochemistry of squaraine dyes. 8. Photophysical properties of crown ether squaraine fluoroionophores and their metal ion complexes. *The Journal of Physical Chemistry*, 98(37), 9291-9296.
- De Cuyper, M., & Bulte, J. W. (2001). *Physics and chemistry basis of biotechnology* (Vol. 7): Springer Science & Business Media.
- Dessi, A., Calamante, M., Mordini, A., Peruzzini, M., Sinicropi, A., Basosi, R., . . . Di Carlo, A. (2014). Organic dyes with intense light absorption especially suitable for application in thin-layer dye-sensitized solar cells. *Chemical Communications*, 50(90), 13952-13955.
- Dewar, M. (1952). A molecular orbital theory of organic chemistry. I. General principles. *Journal of the American Chemical Society*, 74(13), 3341-3345.
- Ditchfield, R., Hehre, W. J., & Pople, J. A. (1971). Self-consistent molecular-orbital methods. IX. An extended Gaussian-type basis for molecular-orbital studies of organic molecules. *The Journal of Chemical Physics*, 54(2), 724-728.
- Ehrlich, P. R., & Ehrlich, A. H. (2008). *The dominant animal: human evolution and the environment*: Island Press.
- Einstein, A. (1905). Über einen die Erzeugung und Verwandlung des Lichtes betreffenden heuristischen Gesichtspunkt. *Annalen Der Physik*, 322(6), 132-148.
- Fan, W., Tan, D., & Deng, W.-Q. (2012). Acene-Modified Triphenylamine Dyes for Dye-Sensitized Solar Cells: A Computational Study. *The Journal of Chemical Physics*, 13(8), 2051-2060.
- Feng, J., Jiao, Y., Ma, W., Nazeeruddin, M. K., Grätzel, M., & Meng, S. (2013). First Principles Design of Dye Molecules with Ullazine Donor for Dye Sensitized Solar Cells. *The Journal of Physical Chemistry C*, 117(8), 3772-3778.

- Fischer, M. K. R., Wenger, S., Wang, M., Mishra, A., Zakeeruddin, S. M., Grätzel, M., & Bäuerle, P. (2010). D- π -A Sensitizers for Dye-Sensitized Solar Cells: Linear vs Branched Oligothiophenes. *Chemistry of Materials*, 22(5), 1836-1845.
- Fong, F. (1976). Energy upconversion and the minimum quantum requirement in photosynthesis. *Journal of the American Chemical Society*, 98(24), 7840-7843.
- Gapol, M. A. B., Balanay, M. P., & Kim, D. H. (2017). Molecular engineering of tetraphenylbenzidine-based hole transport material for perovskite solar cell. *The Journal of Physical Chemistry A*, 121(6), 1371-1380.
- Gaussian 09, R. A., M. J. Frisch et. al., (2009). Wallingford CT: Gaussian, Inc.
- Grätzel, M. (2003). Dye-sensitized solar cells. *Journal of Photochemistry and Photobiology C: Photochemistry Reviews*, 4(2), 145-153.
- Green, M. (2001). Third generation photovoltaics: Ultra-high conversion efficiency at low cost. *Progress in Photovoltaics: Research and Applications*, 9(2), 123-135.
- Green, M. A., Emery, K., Hishikawa, Y., Warta, W., & Dunlop, E. D. (2014). Solar cell efficiency tables (version 43). *Progress in Photovoltaics: Research and Applications*, 22(1), 1-9.
- Gu, X., Zhou, L., Li, Y., Sun, Q., & Jena, P. (2012). Design of new metal-free dyes for dye-sensitized solar cells: A first-principles study. *Physics Letters A*, 376(38), 2595-2599.
- Guarnieri, M. (2015). More light on information. *IEEE Industrial Electronics Magazine*, 9, 58-61.
- Gude, C., & Rettig, W. (2000). Radiative and nonradiative excited state relaxation channels in squaric acid derivatives bearing differently sized donor substituents: a comparison of experiment and theory. *The Journal of Physical Chemistry A*, 104(34), 8050-8057.
- Hagberg, D. P., Marinado, T., Karlsson, K. M., Nonomura, K., Qin, P., Boschloo, G., Sun, L. (2007). Tuning the HOMO and LUMO Energy Levels of Organic Chromophores for Dye Sensitized Solar Cells. *The Journal of Organic Chemistry*, 72(25), 9550-9556.
- Hagfeldt, A., Boschloo, G., Sun, L., Kloo, L., & Pettersson, H. (2010). Dye-Sensitized Solar Cells. *Chemical Reviews*, 110(11), 6595-6663.
- Hamann, T. W., Farha, O. K., & Hupp, J. T. (2008). Outer-Sphere Redox Couples as Shuttles in Dye-Sensitized Solar Cells. Performance Enhancement Based on Photoelectrode Modification via Atomic Layer Deposition. *The Journal of Physical Chemistry C*, 112(49), 19756-19764.

- Hamann, T. W., Jensen, R. A., Martinson, A. B., Van Ryswyk, H., & Hupp, J. T. (2008). Advancing beyond current generation dye-sensitized solar cells. *Energy & Environmental Science*, 1(1), 66-78.
- Hardin, B. E., Snaith, H. J., & McGehee, M. D. (2012). The renaissance of dye-sensitized solar cells. *Nature Photonics*, 55(6), Article#162.
- Hartree, D. R. (1928). *The wave mechanics of an atom with a non-Coulomb central field. Part I. Theory and methods*. Paper presented at the Mathematical Proceedings of the Cambridge Philosophical Society.
- Heredia, D., Natera, J., Gervaldo, M., Otero, L., Fungo, F., Lin, C.-Y., & Wong, K.-T. (2010). Spirobifluorene-Bridged Donor/Acceptor Dye for Organic Dye-Sensitized Solar Cells. *Organic Letters*, 12(1), 12-15.
- Hoffmann, R. (1970). Geometry changes in excited states. *Pure and Applied Chemistry*, 24(3), 567-584.
- Hubbard, J. (1963). Electron correlations in narrow energy bands. *Proceedings of the Royal Society of London. Series A. Mathematical and Physical Sciences*, 276(1365), 238-257.
- Hung, J., Liang, W., Luo, J., Shi, Z., Jen, A. K.-Y., & Li, X. (2010). Rational design using Dewar's rules for enhancing the first hyperpolarizability of nonlinear optical chromophores. *The Journal of Physical Chemistry C*, 114(50), 22284-22288.
- Ince, M. (2012). Subphthalocyanines, Phthalocyanines and Azulenocyanines: Red and NIR-Absorbing Dyes for Molecular Photovoltaics.
- Janak, J. (1978). Proof that $\partial E/\partial n_i = \epsilon_i$ in density-functional theory. *Physical Review B*, 18(12), 7165.
- Jensen, F. (2017). *Introduction to computational chemistry*. John Wiley & Sons.
- Kamlet, M. J., & Taft, R. (1976). The solvatochromic comparison method. I. The beta.-scale of solvent hydrogen-bond acceptor (HBA) basicities. *Journal of the American Chemical Society*, 98(2), 377-383.
- Kanaparthi, R. K., Kandhadi, J., & Giribabu, L. (2012). Metal-free organic dyes for dye-sensitized solar cells: recent advances. *Tetrahedron*, 68(40), 8383-8393.
- Kashif, M. K., Nippe, M., Duffy, N. W., Forsyth, C. M., Chang, C. J., Long, J. R., Bach, U. (2013). Stable Dye-Sensitized Solar Cell Electrolytes Based on Cobalt(II)/(III) Complexes of a Hexadentate Pyridyl Ligand. *Angewandte Chemie International Edition*, 52(21), 5527-5531.
- Kato, F., Kikuchi, A., Okuyama, T., Oyaizu, K., & Nishide, H. (2012). Nitroxide Radicals as Highly Reactive Redox Mediators in Dye-Sensitized Solar Cells. *Angewandte Chemie*, 124(40), 10324-10327.

- Katriel, J., & Davidson, E. R. (1980). Asymptotic behavior of atomic and molecular wave functions. *Proceedings of the National Academy of Sciences*, 77(8), 4403-4406.
- Katritzky, A. R., Kuanar, M., Slavov, S., Hall, C. D., Karelson, M., Kahn, I., & Dobchev, D. A. (2010). Quantitative correlation of physical and chemical properties with chemical structure: utility for prediction. *Chemical Reviews*, 110(10), 5714-5789.
- Kim, B.-G., Chung, K., & Kim, J. (2013). Molecular Design Principle of All-organic Dyes for Dye-Sensitized Solar Cells. *Chemistry – A European Journal*, 19(17), 5220-5230.
- Kim, B. G., Chung, K., & Kim, J. (2013). Molecular Design Principle of All-organic Dyes for Dye-Sensitized Solar Cells. *Chemistry-A European Journal*, 19(17), 5220-5230.
- Kirkwood, J. G. (1934). Theory of solutions of molecules containing widely separated charges with special application to zwitterions. *The Journal of Chemical Physics*, 2(7), 351-361.
- Kleinman, L. (1997). Significance of the highest occupied Kohn-Sham eigenvalue. *Physical Review B*, 56(19), 12042.
- Labat, F., Le Bahers, T., Ciofini, I., & Adamo, C. (2012). First-Principles Modeling of Dye-Sensitized Solar Cells: Challenges and Perspectives. *Accounts of Chemical Research*, 45(8), 1268-1277.
- Lee, C.-P., Li, C.-T., & Ho, K.-C. (2017). Use of organic materials in dye-sensitized solar cells. *Materials Today*, 20(5), 267-283.
- Lee, J. Y., Lee, C., Lee, Y. M., Cho, K. Y., Choi, J. W., & Park, J.-K. (2012). Thiophene–nitroxide radical as a novel combination of sensitizer–redox mediator for dye-sensitized solar cells. *Journal of Solid State Electrochemistry*, 16(2), 657-663.
- Levi, A. F. J. (2006). *Applied Quantum Mechanics*: Cambridge University Press.
- Li, D., Li, H., Luo, Y., Li, K., Meng, Q., Armand, M., & Chen, L. (2010). Non-Corrosive, Non-Absorbing Organic Redox Couple for Dye-Sensitized Solar Cells. *Advanced Functional Materials*, 20(19), 3358-3365.
- Li, H., Koh, T. M., Hagfeldt, A., Gratzel, M., Mhaisalkar, S. G., & Grimsdale, A. C. (2013). New donor-[small pi]-acceptor sensitizers containing 5H-[1,2,5]thiadiazolo [3,4-f]isoindole-5,7(6H)-dione and 6H-pyrrolo[3,4-g]quinoxaline-6,8(7H)-dione units. *Chemical Communications*, 49(24), 2409-2411.
- Li, S.-L., Jiang, K.-J., Shao, K.-F., & Yang, L.-M. (2006). Novel organic dyes for efficient dye-sensitized solar cells. *Chemical Communications*(26), 2792-2794.

- Li, T. C., Spokoyny, A. M., She, C., Farha, O. K., Mirkin, C. A., Marks, T. J., & Hupp, J. T. (2010). Ni(III)/(IV) Bis(dicarbollide) as a Fast, Noncorrosive Redox Shuttle for Dye-Sensitized Solar Cells. *Journal of the American Chemical Society*, 132(13), 4580-4582.
- Luan, F., Xu, X., Liu, H., & Cordeiro, N. (2013). *Review of quantitative structure-activity/property relationship studies of dyes: Recent Advances and Perspectives* (Vol. 129).
- Luis, J. M., Bishop, D. M., & Kirtman, B. (2004). A different approach for calculating Franck–Condon factors including anharmonicity. *The Journal of Chemical Physics*, 120(2), 813-822.
- Luque, A., & Hegedus, S. (2011). *Handbook of photovoltaic science and engineering*. John Wiley & Sons.
- Maeda, T., Mineta, S., Fujiwara, H., Nakao, H., Yagi, S., & Nakazumi, H. (2013). Conformational effect of symmetrical squaraine dyes on the performance of dye-sensitized solar cells. *J. Mater. Chem. A*, 1(4), 1303-1309.
- Mao, M., & Song, Q.-H. (2016). The Structure-property Relationships of D- π -A BODIPY Dyes for Dye-sensitized Solar Cells. *The Chemical Record*, 16(2), 719-733.
- Mariachiaro, P., Edoardo, M., Simona, F., & Filippo De, A. (2012). Computational Investigations on Organic Sensitizers for Dye-Sensitized Solar Cell. *Current Organic Synthesis*, 9(2), 215-232.
- Marszalek, M., Nagane, S., Ichake, A., Humphry-Baker, R., Paul, V., Zakeeruddin, S. M., & Gratzel, M. (2013). Structural variations of D-[small pi]-A dyes influence on the photovoltaic performance of dye-sensitized solar cells. *RSC Advances*, 3(21), 7921-7927.
- Martin, R. M., & Martin, R. M. (2004). *Electronic Structure: Basic Theory and Practical Methods*: Cambridge university press.
- Mathew, S., Yella, A., Gao, P., Humphry-Baker, R., CurchodBasile, F. E., Ashari-Astani, N., Grätzel, M. (2014). Dye-sensitized solar cells with 13% efficiency achieved through the molecular engineering of porphyrin sensitizers. *Natural Chemistry*, 6(3), 242-247.
- Mayerhöffer, U., Deing, K., Groß, K., Braunschweig, H., Meerholz, K., & Würthner, F. (2009). Outstanding Short-Circuit Currents in BHJ Solar Cells Based on NIR-Absorbing Acceptor-Substituted Squaraines. *Angewandte Chemie International Edition*, 48(46), 8776-8779.
- Mishra, A., Fischer, M. K., & Bäuerle, P. (2009). Metal-free organic dyes for dye-sensitized solar cells: From structure: Property relationships to design rules. *Angewandte Chemie International Edition*, 48(14), 2474-2499.

- Mishra, A., Fischer, M. K. R., & Bäuerle, P. (2009). Metal-Free Organic Dyes for Dye-Sensitized Solar Cells: From Structure: Property Relationships to Design Rules. *Angewandte Chemie International Edition*, 48(14), 2474-2499.
- Mohammadi, N., & Wang, F. (2014). First-principles study of Carbz-PAHTDDT dye sensitizer and two Carbz-derived dyes for dye sensitized solar cells. *Journal of Molecular Modeling*, 20(3), 2177.
- Nava, P. (2005). *Density functional theory calculations on palladium clusters and on an AgInS semiconductor compound*. Cuvillier Verlag.
- Nazeeruddin, M. K., De Angelis, F., Fantacci, S., Selloni, A., Viscardi, G., Liska, P., . . . Grätzel, M. (2005). Combined Experimental and DFT-TDDFT Computational Study of Photoelectrochemical Cell Ruthenium Sensitizers. *Journal of the American Chemical Society*, 127(48), 16835-16847.
- Nazeeruddin, M. K., Kay, A., Rodicio, I., Humphry-Baker, R., Mueller, E., Liska, P., . . . Grätzel, M. (1993). Conversion of light to electricity by cis-X₂bis(2,2'-bipyridyl-4,4'-dicarboxylate)ruthenium(II) charge-transfer sensitizers (X = Cl-, Br-, I-, CN-, and SCN-) on nanocrystalline titanium dioxide electrodes. *Journal of the American Chemical Society*, 115(14), 6382-6390.
- Nazeeruddin, M. K., Péchy, P., Renouard, T., Zakeeruddin, S. M., Humphry-Baker, R., Comte, P., Grätzel, M. (2001). Engineering of Efficient Panchromatic Sensitizers for Nanocrystalline TiO₂-Based Solar Cells. *Journal of the American Chemical Society*, 123(8), 1613-1624.
- Ning, Z., Zhang, Q., Wu, W., & Tian, H. (2009). Novel iridium complex with carboxyl pyridyl ligand for dye-sensitized solar cells: High fluorescence intensity, high electron injection efficiency? *Journal of Organometallic Chemistry*, 694(17), 2705-2711.
- Noufi, Rommel. & Zweibel, Kenneth. & National Renewable Energy Laboratory (U.S.). (2006). *High-efficiency CdTe and CIGS thin-film solar cells highlights and challenges : preprint*. Golden, CO : National Renewable Energy Laboratory
- Nusbaumer, H., Moser, J.-E., Zakeeruddin, S. M., Nazeeruddin, M. K., & Grätzel, M. (2001). CoII(dbbip)₂²⁺ Complex Rivals Tri-iodide/Iodide Redox Mediator in Dye-Sensitized Photovoltaic Cells. *The Journal of Physical Chemistry B*, 105(43), 10461-10464.
- O'Regan, B., & Gratzel, M. (1991). A low-cost, high-efficiency solar cell based on dye-sensitized colloidal TiO₂ films. *Nature*, 353(6346), 737-740.
- Ohira, S., Rudra, I., Schmidt, K., Barlow, S., Chung, S. J., Zhang, Q., . . . Brédas, J. L. (2008). Electronic and Vibronic Contributions to Two-Photon Absorption in Donor–Acceptor–Donor Squaraine Chromophores. *Chemistry–A European Journal*, 14(35), 11082-11091.

- Ooyama, Y., Sato, T., Harima, Y., & Ohshita, J. (2014). Development of a D-[small pi]-A dye with benzothienopyridine as the electron-withdrawing anchoring group for dye-sensitized solar cells. *Journal of Materials Chemistry A*, 2(10), 3293-3296.
- Pandey, S. S., Inoue, T., Fujikawa, N., Yamaguchi, Y., & Hayase, S. (2010). Alkyl and fluoro-alkyl substituted squaraine dyes: A prospective approach towards development of novel NIR sensitizers. *Thin Solid Films*, 519(3), 1066-1071.
- Park, J., Barbero, N., Yoon, J., Dell'Orto, E., Galliano, S., Borrelli, R., . . . Nazeeruddin, M. K. (2014). Panchromatic symmetrical squaraines: a step forward in the molecular engineering of low cost blue-greenish sensitizers for dye-sensitized solar cells. *Physical Chemistry Chemical Physics*, 16(44), 24173-24177.
- Park, J., Barolo, C., Sauvage, F., Barbero, N., Benzi, C., Quagliotto, P., . . . Nazeeruddin, M. K. (2012). Symmetric vs. asymmetric squaraines as photosensitisers in mesoscopic injection solar cells: a structure-property relationship study. *Chemical Communications*, 48(22), 2782-2784.
- Parnas, D. L., & Clements, P. C. (1985). A rational design process: How and why to fake it. In H. Ehrig, C. Floyd, M. Nivat, & J. Thatcher (Eds.), *Formal Methods and Software Development: Proceedings of the International Joint Conference on Theory and Practice of Software Development (TAPSOFT) Berlin, March 25-29, 1985* (pp. 80-100). Berlin, Heidelberg: Springer Berlin Heidelberg.
- Pastore, M., & De Angelis, F. (2014). Modeling Materials and Processes in Dye-Sensitized Solar Cells: Understanding the Mechanism, Improving the Efficiency. In D. Beljonne & J. Cornil (Eds.), *Multiscale Modelling of Organic and Hybrid Photovoltaics* (pp. 151-236). Berlin, Heidelberg: Springer Berlin Heidelberg.
- Pastore, M., Fantacci, S., & De Angelis, F. (2010). Ab Initio Determination of Ground and Excited State Oxidation Potentials of Organic Chromophores for Dye-Sensitized Solar Cells. *The Journal of Physical Chemistry C*, 114(51), 22742-22750.
- Pastore, M., Fantacci, S., & De Angelis, F. (2013). Modeling excited states and alignment of energy levels in dye-sensitized solar cells: successes, failures, and challenges. *The Journal of Physical Chemistry C*, 117(8), 3685-3700.
- Pastore, M., Mosconi, E., De Angelis, F., & Grätzel, M. (2010). A Computational Investigation of Organic Dyes for Dye-Sensitized Solar Cells: Benchmark, Strategies, and Open Issues. *The Journal of Physical Chemistry C*, 114(15), 7205-7212.
- Perdew, J., Parr, R., Levy, M., & Balduz, J. (1982). The result for $N=Z$ is correct, and corresponds to (5). *N*, 49, 1691.
- Perdew, J. P. (1985). Density functional theory and the band gap problem. *International Journal of Quantum Chemistry*, 28(S19), 497-523.

- Perdew, J. P., & Levy, M. (1997). Comment on "Significance of the highest occupied Kohn-Sham eigenvalue". *Physical Review B*, 56(24), 16021.
- Peter, L. M. (2011). The Grätzel Cell: Where Next? *The Journal of Physical Chemistry Letters*, 2(15), 1861-1867.
- Peters, A. T., & Freeman, H. S. (1994). *Modern colorants: Synthesis and structure* (Vol. 3): Springer Science & Business Media.
- Qin, C., Peng, W., Zhang, K., Islam, A., & Han, L. (2012). A Novel Organic Sensitizer Combined with a Cobalt Complex Redox Shuttle for Dye-Sensitized Solar Cells. *Organic Letters*, 14(10), 2532-2535.
- Ramamurthy, V. (1997). *Organic photochemistry*. New York: CRC Press.
- Rani, S., Suri, P., & Mehra, R. M. (2011). Mechanism of charge recombination and IPCE in ZnO dye-sensitized solar cells having I⁻/I₃⁻ and Br⁻/Br₃⁻ redox couple. *Progress in Photovoltaics: Research and Applications*, 19(2), 180-186.
- Richards, R., Covington, A., Prue, J., Albery, W., Borrell, P., Bamford, C., . . . Sheridan, J. (1963). General and physical chemistry. *Annual Reports on the Progress of Chemistry*, 60, 7-176.
- Sánchez-de-Armas, R., San-Miguel, M. A., Oviedo, J., & Sanz, J. F. (2012). Molecular modification of coumarin dyes for more efficient dye sensitized solar cells. *The Journal of Chemical Physics*, 136(19).
- Sanchez-de-Armas, R., San Miguel, M. A., Oviedo, J., & Sanz, J. F. (2012). Coumarin derivatives for dye sensitized solar cells: a TD-DFT study. *Physical Chemistry Chemical Physics*, 14(1), 225-233.
- Sawyer, W. D. (1986). An improved method of light-beam-induced current characterization of grain boundaries. *Journal of Applied Physics*, 59(7), 2361-2363.
- Schiermeier, Q., Tollefson, J., Scully, T., Witze, A., & Morton, O. (2008). Energy alternatives: Electricity without carbon. *Nature News*, 454(7206), 816-823.
- Schoch, K. F. (2004). Advanced polymeric materials: structure property relationships [Book Review]. *IEEE Electrical Insulation Magazine*, 20(5), 43-44.
- Schrödinger, E. (1926). An undulatory theory of the mechanics of atoms and molecules. *Physical Review*, 28(6).
- Seybold, P. G., May, M., & Bagal, U. A. (1987a). Molecular structure: Property relationships. *Journal of Chemical Education*, 64(7), 575.
- Seybold, P. G., May, M., & Bagal, U. A. (1987b). Molecular structure: Property relationships. *Journal of Chemical Education*, 64(7), 575.

- Sherrill, C. D. (2001). A Brief Review of Elementary Quantum Chemistry. *Georgia Institute of Technology, School of Chemistry and Biochemistry*.
- Slater, J. C. (1929). The theory of complex spectra. *Physical Review*, 34(10), 1293.
- Slater, J. C. (1951). A simplification of the Hartree-Fock method. *Physical Review*, 81(3), 385.
- Smith, H. (1991). *Introduction to Quantum Mechanics*: World Scientific Publishing Co Inc.
- Spokoyny, A. M., Li, T. C., Farha, O. K., Machan, C. W., She, C., Stern, C. L., Mirkin, C. A. (2010). Electronic Tuning of Nickel-Based Bis(dicarbollide) Redox Shuttles in Dye-Sensitized Solar Cells. *Angewandte Chemie International Edition in English*, 49(31), 5339-5343.
- Sprenger, H. E., & Ziegenbein, W. (1967). The Cyclobutenediylum Cation, a Novel Chromophore from Squaric Acid. *Angewandte Chemie International Edition in English*, 6(6), 553-554.
- Tatarets, A. L., Fedyunyaeva, I. A., Terpetschnig, E., & Patsenker, L. D. (2005). Synthesis of novel squaraine dyes and their intermediates. *Dyes and Pigments*, 64(2), 125-134.
- Tatikolov, A. S., & Costa, S. I. M. (2001). Photophysical and aggregation properties of a long-chain squarylium indocyanine dye. *Journal of Photochemistry and Photobiology A: Chemistry*, 140(2), 147-156.
- Teng, C., Yang, X., Yuan, C., Li, C., Chen, R., Tian, H., Sun, L. (2009). Two Novel Carbazole Dyes for Dye-Sensitized Solar Cells with Open-Circuit Voltages up to 1 V Based on Br⁻/Br₃⁻ Electrolytes. *Organic Letters*, 11(23), 5542-5545.
- Thorndike Greenspan, N. (2005). *The end of the certain world: The life and science of Max Born. The Nobel physicist who ignited the quantum revolution*: Basic books.
- Tian, H., Jiang, X., Yu, Z., Kloo, L., Hagfeldt, A., & Sun, L. (2010). Efficient Organic-Dye-Sensitized Solar Cells Based on an Iodine-Free Electrolyte. *Angewandte Chemie International Edition*, 49(40), 7328-7331.
- Tomasi, J., Mennucci, B., & Cammi, R. (2005). Quantum mechanical continuum solvation models. *Chemical reviews*, 105(8), 2999-3094.
- Tortorella, S., Talamo, M. M., Cardone, A., Pastore, M., & De Angelis, F. (2016). Benchmarking DFT and semi-empirical methods for a reliable and cost-efficient computational screening of benzofulvene derivatives as donor materials for small-molecule organic solar cells. *J Phys Condens Matter*, 28(7).
- Treibs, A., & Jacob, K. (1965). *Angewandte Chemie International Edition*, 694(4).

- Velusamy, M., Hsu, Y.-C., Lin, J. T., Chang, C.-W., & Hsu, C.-P. (2010). 1-Alkyl-1H-imidazole-Based Dipolar Organic Compounds for Dye-Sensitized Solar Cells. *Chemistry – An Asian Journal*, 5(1), 87-96.
- Völker, S. F., Renz, M., Kaupp, M., & Lambert, C. (2011). Squaraine dyes as efficient coupling bridges between triarylamine redox centres. *Chemistry–A European Journal*, 17(50), 14147-14163.
- von Barth, U. (1984). Many-Body Phenomena at Surfaces.
- Wang, M., Chamberland, N., Breau, L., Moser, J. E., Humphry-Baker, R., Marsan, B., Zakeeruddin, S. M., & Grätzel, M. (2010). An organic redox electrolyte to rival triiodide/iodide in dye-sensitized solar cells. *Nature chemistry*, 2(5), 385–389.
- Xiang, W., Huang, F., Cheng, Y.-B., Bach, U., & Spiccia, L. (2013). Aqueous dye-sensitized solar cell electrolytes based on the cobalt(ii)/(iii) tris(bipyridine) redox couple. *Energy & Environmental Science*, 6(1), 121-127.
- Yan, Z., Guang, S., Su, X., & Xu, H. (2012). Near-infrared absorbing squaraine dyes for solar cells: relationship between architecture and performance. *The Journal of Physical Chemistry C*, 116(16), 8894-8900.
- Yang, J., Ganesan, P., Teuscher, J., Moehl, T., Kim, Y. J., Yi, C., Grätzel, M. (2014). Influence of the Donor Size in D- π -A Organic Dyes for Dye-Sensitized Solar Cells. *Journal of the American Chemical Society*, 136(15), 5722-5730.
- Yang, L., Guo, L., Chen, Q., Sun, H., Liu, J., Zhang, X., Dai, S. (2012). Theoretical design and screening of panchromatic phthalocyanine sensitizers derived from TT1 for dye-sensitized solar cells. *Journal of Molecular Graphics and Modelling*, 1-9.
- Yella, A., Lee, H. W., Tsao, H. N., Yi, C., Chandiran, A. K., Nazeeruddin, M. K., Diao, E. W., Yeh, C. Y., Zakeeruddin, S. M., & Grätzel, M. (2011). Porphyrin-sensitized solar cells with cobalt (II/III)-based redox electrolyte exceed 12 percent efficiency. *Science New York*, 629–634.
- Zhan, C.-G., Nichols, J. A., & Dixon, D. A. (2003). Ionization potential, electron affinity, electronegativity, hardness, and electron excitation energy: molecular properties from density functional theory orbital energies. *The Journal of Physical Chemistry A*, 107(20), 4184-4195.
- Zhang, J., Kan, Y.-H., Li, H.-B., Geng, Y., Wu, Y., & Su, Z.-M. (2012). How to design proper π -spacer order of the D- π -A dyes for DSSCs? A density functional response. *Dyes and Pigments*, 95(2), 313-321.
- Zhang, J., Li, H.-B., Sun, S.-L., Geng, Y., Wu, Y., & Su, Z.-M. (2012). Density functional theory characterization and design of high-performance diarylamine-fluorene dyes with different [small pi] spacers for dye-sensitized solar cells. *Journal of Materials Chemistry*, 22(2), 568-576.

Zhou, H., Xue, P., Zhang, Y., Zhao, X., Jia, J., Zhang, X., .Lu, R. (2011). Fluorenylvinylenes bridged triphenylamine-based dyes with enhanced performance in dye-sensitized solar cells. *Tetrahedron*, 67(44), 8477-8483.

Zhu, H., Y., & Lewars, E. G., (2018). Computational Chemistry; Introduction to the Theory and Applications of Molecular and Quantum Mechanics 2nd edition, *Springer-Verlag*. 68(8), 560-561.

University of Malaya

LIST OF PUBLICATIONS AND PAPERS PRESENTED

PUBLICATIONS

1. Ramle, A. Q., Khaledi, H., **Hashim, A. H.**, Mingsukang, M. A., Arof, A. K. M., Ali, H. M., & Basirun, W. J. (2019). Indolenine–dibenzotetraaza [14] annulene Ni (II) complexes as sensitizers for dye-sensitized solar cells. *Dyes and Pigments*, 164, 112-118.
2. **Hashim, A. H.**, Zain, S. M., Lee, V. S., & Said, S. M. (2018). Electronic, magnetic and structural properties of Co₃O₄ (100) surface: a DFT+ U study. *Applied Surface Science*, 427, 1090-1095.

PAPERS PRESENTED

1. Ramle, A. Q., Khaledi, H., **Hashim, A. H.**, Mingsukang, M. A., Arof, A. K. M., Ali, H. M., & Basirun, W. J. (2019) *Theoretical Studies and Rational Design of Indolenine Tetraaza Annulene (14): An Application for Dye Sensitized Solar Cells (DSSC's)*. Paper presented at International Conference in Organic Synthesis 2016, 21st – 24th August 2016, Majestic Hotel, Kuching, Sarawak, Malaysia.
2. **Hashim, A. H.**, Zain, S. M., Lee, V. S., & Said, S. M. (2018). *Theoretical Optimization of Symmetrical and Unsymmetrical Organic Dyes for Dye-Sensitized Solar Cell Applications*. Paper presented at the 9th Conference of the Asian Consortium on Computational Materials Science (ACCMS-9), 9th – 11th August 2017, Berjaya Time Square Hotel, Kuala Lumpur, Malaysia.